Continuous comagnetometry using transversely polarized Xe isotopes

by

Daniel Thrasher

A dissertation submitted in partial fulfillment of

the requirements for the degree of

Doctor of Philosophy

(Physics)

at the

UNIVERSITY OF WISCONSIN–MADISON

2020

Date of final oral examination: 03/12/2020

The dissertation is approved by the following members of the Final Oral Committee:

Thad G. Walker, Professor, Physics

Deniz Yavuz, Professor, Physics

Shimon Kolkowitz, Assistant Professor, Physics

Jennifer Choy, Assistant Professor, Engineering Physics

For my children.

Acknowledgments

Interviewer: Why weren't you willing to pay for piano lessons for your son?

Samuel: How was I supposed to know he would grow up to be Lenny Bernstein?

— Samuel Joseph Bernstein

Although I am certainly not the Leonard Bernstein of the physics community, there have been many people in my life who, unlike Leonard's father, have recognized my potential and paid for my proverbial piano lessons.

Thad has been a most gracious adviser throughout this project. His infectious love for physics is inspiring. Susan Sorensen has been an able co-researcher with me on this project. Her contributions are many and much appreciated. Anna Korver was the senior graduate student when I joined the project and was a wonderful mentor. Josh Weber worked as a postdoctoral researcher on the project for two years. He helped keep the project progressing during my leave of absence, for which I am very grateful.

This project received much support from the NMR-gyro research team at Northrop Grumman. Mike Bulatowicz has often shared his expertise and well designed hardware. Mike Larsen has been an unwavering supporter of this research. He has enabled the sharing of NGC property, both intellectual and hardware, as well as funding between our research teams. His insight has been a great resource. James Pavell provided beautiful vapor cells used during my tenure.

The National Science Foundation has provided three rounds of funding through their Grant Opportunities for Academic Liaison with Industry program, without which this project would not be possible. I express gratitude to Ann Austin for her tireless efforts to stream line equipment purchases and Aimee Lefkow for the numberless things she does behind the scenes so I can focus on research.

Finally, I thank my wife for her enduring support.

Contents

List of Tables

List of Figures

Abstract

This thesis describes the development of a new type of spin-exchange pumped noble gas comagnetometer. The comagnetometer is designed to suppress systematic uncertainty introduced by longitudinal noble gas and alkali-metal polarizations while maintaining detection bandwidth. To this end, ^{129}Xe and ^{131}Xe nuclei are simultaneously and continuously polarized transverse to a pulsed bias field by modulation of spin-exchange collisions with transversely optically pumped ^{85}Rb atoms. In addition to polarizing the Xe nuclei, the polarized Rb atoms also serve as an embedded magnetometer that detects the precession of both noble gas isotopes simultaneously. Continuous comagnetometry is demonstrated via two different modulation schemes: polarization modulation and bias pulse repetition rate modulation. The theory of these implementations including a description of spin-exchange broadening and noble gas polarizations are also described in detail. The field suppression, stability, and detection channel fidelity of each implementation are also presented.

Chapter 1

Introduction

> *What sort of science is that which enriches the understanding but robs the imagination?*
>
> — Henry David Thoreau

This thesis describes the design and implementation of a novel quantum spin sensor. Simultaneous measurement of the nuclear magnetic resonance (NMR) of two hyperpolarized noble gases contained in the same volume is used to differentiate between magnetic and non-magnetic phenomena. We introduce the concept of comagnetometry with polarized nuclei, describe previously demonstrated comagnetometers and their application to measuring non-magnetic spin-dependent interactions, describe known systematic uncertainties inherent to spin-exchange pumped comagnetometers, and summarize the results of the novel comagnetometer we developed.

1.1 Fundamentals

Perhaps the most simple quantum spin sensor is a polarized atom or nucleus. When immersed in a magnetic field, the atom or nucleus will undergo Larmor precession about the magnetic field. The rate of precession due to the magnetic field is determined by the

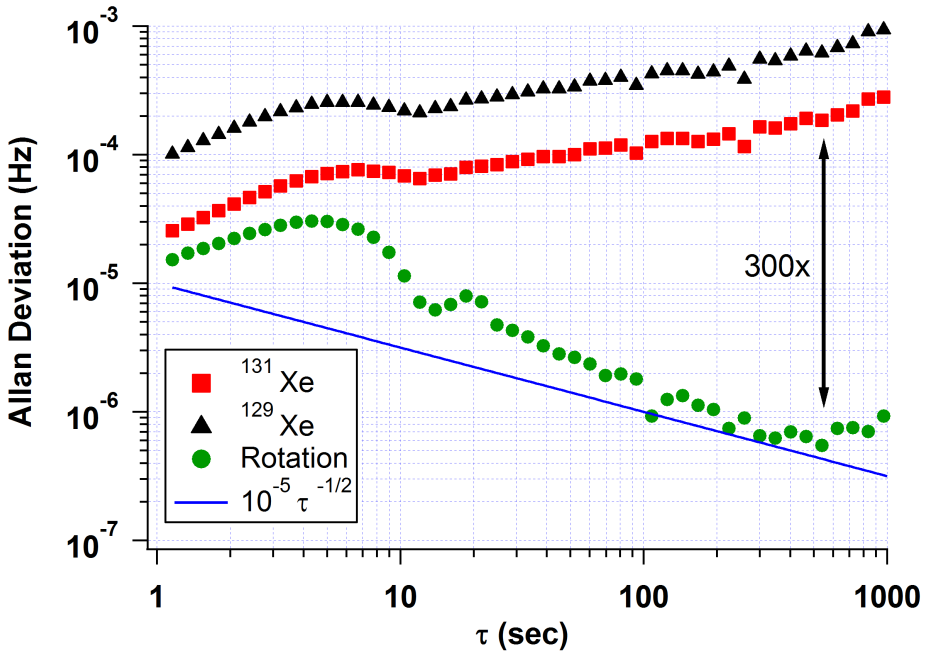

Figure 1.1: Allan Deviation of measured precession frequencies of ^{131}Xe, ^{129}Xe, and the computed rotation for one of the comagnetometer implimentations discussed in this thesis.

atom or nucleus' gyromagnetic ratio. The rate of precession can also be influenced by many non-magnetic spin-dependent interactions (NMSI) which one may or may not want to measure. Comagnetometry is the simultaneous measurement of multiple co-located polarized entities as they precess about a common magnetic field. As long as the gyromagnetic ratio of each entity is well known, comagnetometry enables the suppression of magnetic noise, thereby enabling enhanced sensitivity to NMSI. Figure 1.1 demonstrates the increased frequency sensitivity to NMSI achieved through comagnetometry. The individual Larmor resonance frequencies of ^{129}Xe (black) and ^{131}Xe (red) are dominated by stray magnetic field noise in a three layer μ-metal magnetic shield. With knowledge of each isotope's gyromagnetic ratio however, the correlated magnetic field noise is subtracted (green) thereby enhancing sensitivity to NMSI by more than two orders of magnitude.

The Heisenberg uncertainty relation for resolving the energy splitting ΔE of a single atom with a coherence time T_2 is $\Delta E \geq \hbar/T_2$. The transition frequency uncertainty when

measuring N atoms once every T_2 over a time t is then

$$\Delta f = \frac{1}{2\pi T_2}\sqrt{\frac{T_2}{N\,t}}. \tag{1.1}$$

A 1 cm^3 vapor cell filled with 50 Torr of enriched Xe has $\sim 2\times10^{18}$ Xe nuclei. Assuming a modest $T_2 = 100$ sec, $\Delta f \approx 10$ pHz/$\sqrt{\text{Hz}}$. The lowest noise resolved in a spin-exchange pumped comagnetometer to date is x10^4 greater than this value (see Ch. 1.3). The promise of such fantastically low noise is part of what continues to drive the development of new quantum spin sensors.

Spin-exchange (SE) pumped comagnetometers consist of co-located ensembles of noble gas nuclei and alkali-metal atoms which are spin polarized in the presence of a magnetic field [Walker and Happer (1997)]. Suppose an ensemble of two spin-exchange optically pumped (SEOP) noble gas species (a and b) are each subject to a common magnetic field B_z and some NMSI X_z. The Larmor resonance frequency of each isotope obeys [Walker and Larsen (2016); Limes et al. (2019); Terrano et al. (2019); Petrov et al. (2019)]

$$\Omega^a = \gamma^a(B_z + b^a_S S_z + b^a_b K^b_z) + X^a_z, \tag{1.2a}$$

$$\Omega^b = \gamma^b(B_z + b^b_S S_z + b^b_a K^a_z) + X^b_z, \tag{1.2b}$$

where γ is the gyromagnetic ratio, S and K are the respective alkali-metal and noble gas polarizations, z subscripts refer to the longitudinal components (*i.e.*, parallel to the bias field direction), and b^i_j is the SE coefficient [Schaefer et al. (1989)] characterizing the influence of j's polarization on i. Given a known $\rho = \gamma^a/\gamma^b$, Ω^a and Ω^b can be simultaneously measured and correlated B_z fluctuations subtracted using [Chupp et al. (1988)],

$$\xi = \frac{\rho\Omega^b - \Omega^a}{1+\rho} = \frac{\rho X^b_z - X^a_z}{1+\rho} + \frac{\gamma^a}{1+\rho}[(b^b_S - b^a_S)S_z + b^b_a K^a_z - b^a_b K^b_z]. \tag{1.3}$$

We see that although Eq. 1.3 is independent of B_z, longitudinal polarizations S_z and K_z remain and are indistinguishable from X_z [Bulatowicz et al. (2013); Limes et al. (2019); Terrano et al. (2019)]. In the context of rotation sensing and for $\gamma^a < 0$, and $\gamma^b > 0$, we set $X_z^b = \omega^R$ and $X_z^a = -\omega^R$ [Walker and Larsen (2016)] such that ξ becomes the rotation frequency ω^R. The main motivation of this thesis is the suppression of time averaged S_z and K_z while maintaining the detection bandwidth of ξ.

The embedded alkali-metal atoms can be used for quantum non-demolition readout [Takahashi et al. (1999); Katz et al. (2019)] of the noble gas precession. During atomic collisions, a Fermi-contact interaction enhances the field experienced by the alkali-metal atoms due to the polarized noble gas nuclei [Nahlawi et al. (2019)]. This enhancement factor directly improves the signal-to-noise-ratio (SNR) as classical fields are not similarly enhanced. Using the alkali-metal atoms also enables miniaturization by eliminating the need for an exterior pick-up coil (such as a superconducting quantum interference device [Allmendinger et al. (2019); Sachdeva et al. (2019)]).

1.2 Applications

Comagnetometers are uniquely qualified for some searches of exotic physics because of their absolute sensitivity to small energy changes. For instance, although optical atomic clocks exhibit exquisite fractional stability $\delta\nu/\nu \sim 10^{-18}$ their absolute frequency (energy) sensitivity is $\delta\nu \sim 100$ μHz [Ludlow et al. (2015)]. Comagnetometers have less exquisite instability $\delta\nu/\nu \sim 10^{-9}$, but their absolute stability is $\delta\nu \sim 10$ nHz or 10^4 times more sensitive than optical atomic clocks. SE pumped comagnetometers have been used to place upper bounds on spin-mass couplings [Bulatowicz et al. (2013); Lee et al. (2018)], nuclear electric dipole moments [Rosenberry and Chupp (2001); Allmendinger et al. (2019); Sachdeva et al. (2019)] as well as local Lorentz invariance violation [Bear et al. (2000); Gemmel et al. (2010)]. These devices also show promise as miniaturized inertial sensors [Walker and Larsen

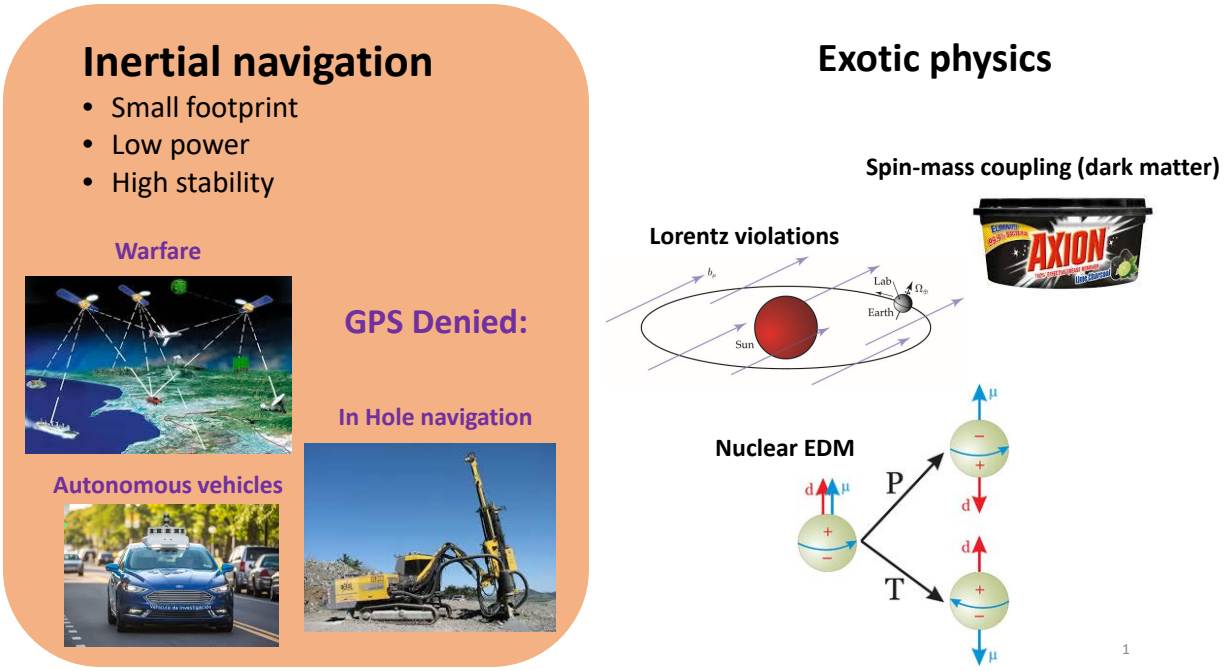

Figure 1.2: Collage depicting applications of noble gas comagnetometers.

(2016); Kornack et al. (2005); Jiang et al. (2018); Karwacki (1980)]. In the paragraphs that follow we outline the fundamental physics behind these NMSI.

Exotic Physics

Spin-mass couplings: There are various theories beyond the standard model that predict new particles which are characterized by very weak couplings to ordinary matter and have masses in the sub-ev range. One possibility is a new P-odd and T-odd interaction between polarized and unpolarized nucleons proportional to $\mathbf{K} \cdot \mathbf{r} e^{-r/\lambda}$, where $\mathbf{K}$ is the spin of the polarized nucleon, $\mathbf{r}$ is the distance between polarized and un-polarized nucleons, and λ is the interaction range. Laboratory searches for such an interaction have been pursued by monitoring a comagnetometer's signal dependence on the proximity of a non-magnetic "source" mass.

Atomic electric dipole moments (EDM): An electric dipole moment in a nucleus would

manifest itself as a charge asymmetry along the axis of total angular momentum. Such an asymmetry is odd for both time and parity reversal. Although the standard model allows for simultaneous charge and parity conjugation violation, such violation is insufficient to explain the size of the observed baryon asymmetry of the universe. By putting new upper bounds on atomic EDMs by direct laboratory searches, theories beyond the standard model, which allow for EDMs greater than the standard model, can be constrained. Comagnetometers have been used to search for atomic EDMs by looking for correlations between the comagnetometer signal and an applied electric field. For instance, if ^{129}Xe had a permanent EDM of $d\mathbf{F}/F$ where $\mathbf{F}$ is total angular momentum then the frequency shift between states with $|\Delta_{m_F}| = 1$ would be $\omega_d = \pm d|E|/(\hbar F)$.

Local Lorentz invariance violation (LLIV): Lorentz invariance is the assumption that the laws of physics are invariant under transformation between two coordinate frames moving at constant velocity with respect to one another. The standard model does not allow for the existence of a preferred reference frame i.e. violation of Lorentz invariance. Tests of LLIV of spin and light are crucial for constraining standard model extensions. Comagnetometers have been used to search for the isotropy of spin dependent interactions in space by looking for comagnetometer signals which correlate with the device's orientation within the laboratory reference frame. In the presence of Lorentz violation from the photon sector, the Coulomb potential of a point charge becomes anisotropic [Flambaum and Romalis (2017)]. A nuclei's sensitivity to this anisotropy depends on its nuclear electric quadrupole moment. Similar to measurements of LLIV for spins, noble gas comagnetometers with one species with a nuclear spin greater than 1/2, can be used to search for LLIV of the photon by searching for correlations between the comagnetometer's signal and its orientation in space.

Inertial Rotation

The precession of a polarized gas about a constant bias field constitutes an inertial reference frame, i.e. the nuclei (idealy) have no way of knowing whether or not their container is rotating. If the precession of the noble gas is measured relative to the polarization of the alkali-metal atoms which is itself determined by the polarization of its pump laser then rotation of the pump laser about the bias field will change the measured rate of precession of the polarized noble gas nuclei (if the rate of rotation of the pump laser about B_z is equal to that of one of the noble gas species' rate of precession then the SE field produced by that isotope would always have the same orientation relative to the Rb polarization and consequently not produce any tourque on the Rb).

Interest in novel navigation systems which operate in global positioning system (GPS) denied environments has increased as of recent. To date, the United States, Russia, China, and India have successfully demonstrated the capability of destroying their own satellites. Such capability could be used in future conflict to remove GPS satellites. Other GPS denied environments besides future war zones include subterranean and submarine travel. An important obstacle to harnessing geothermal energy resources is the limited "in-hole" navigation of horizontal drilling rigs. The future development of autonomous vehicles also relies on robust navigation including in GPS denied environments.

The application of comagnetometers as inertial sensors is promising because of their low intrinsic noise, miniaturize-ability, low power consumption, insensitivity to acceleration, and a scaling from experimental observable to rotation that is independent of experimental parameters. NMR-gyroscopes will likely first be used to provide long term correction to another miniaturized gyro whose short term noise performance is superior but whose long term drift is inferior to the NMR-gyroscope. A proof of concept experiment along these lines was recently performed using a classical and quantum accelerometer [Cheiney et al. (2018)].

As this section has shown, the contribution of comagnetometers to the precision mea-

surement community has been substantial. All measurements mentioned above were limited by technical noise which is orders of magnitude greater than the quantum projection noise limits. Consequently, all of the precision measurements listed above would benefit from new comagnetometer schemes which limit technical noise.

1.3 Prior Art

SE pumped comagnetometers have been under development for more than 60 years. In the section below we briefly summarize the schemes which constitute the present state of the art in order to better place the performance of our novel sensor in perspective. In general, comagnetometer performance is described in terms of measurement bandwidth: the fastest NMSI which can be resolved, noise: the rate at which the sensitivity to NMSI interactions increase with integration time, stability: the ultimate sensitivity achieved, and scale factor: the conversion from observed signal to NMSI.

The noise is often characterized in terms of angle-random-walk (ARW) and is measured in units of $\mathrm{Hz}/\sqrt{\mathrm{Hz}}$ or in the inertial measurement community in units of $\mathrm{deg}/\sqrt{\mathrm{Hr}}$. The conversion between these two units can be written as

$$1\frac{\mathrm{Hz}}{\sqrt{\mathrm{Hz}}} = 1\frac{\mathrm{cycles}}{\mathrm{sec}}\frac{\sqrt{\mathrm{sec}}}{1}\frac{360\ \mathrm{deg}}{\mathrm{cycle}}\frac{3600\ \mathrm{sec}}{\mathrm{Hr}}\sqrt{\frac{\mathrm{Hr}}{3600\ \mathrm{sec}}} = 21600\frac{\mathrm{deg}}{\sqrt{\mathrm{Hr}}}. \tag{1.4}$$

Comagnetometers may be limited by other noise processes besides ARW. In such cases it is not uncommon to report the ARW as an upper bound. Consequently, the most fair comparison of comagnetometer performance is by comparing how the noise integrates over time using devices such as the Allan deviation (see Ch. 2.5 for more details on the Allan deviation). The ultimate stability is measured in Hz or in the inertial measurement community (where it is referred to as bias instability) in units of deg/Hr. Similar to Eq. 1.4, 1 Hz = 1.3×10^6 deg/Hr. Table 1.1 lists the required bias instability for various inertial measurement systems

Bias Instability (deg/Hr)	Systems applications
> 10	Automotive sensing
1	attitude heading, short flight devices
0.1	some aircraft
0.01	commercial airliners
< 0.001	ships, submarines, spacecraft

Table 1.1: Bias instability requirements for navigation applications.

applications [Donley and Kitching (2013)].

The scale factor and its stability are important characteristics as they determine how the apparatus' observables depend on NMSI. Indeed, a comagnetometer with fantastic noise and stability but large scale-factor uncertainty is not necessarily more desirable than a comagnetometer with poor noise and stability but exquisite scale-factor stability. We refer to comagnetometers whose scale factor can be written in terms of fundamental constants as having "physics" scale factors.

Northrop Grumman Corp. gyro

A schematic of the Northrop Grumman Corp. gyro (NGC-gyro) [Walker and Larsen (2016)] is shown in Fig. 1.3. It consists of a 2 mm cubic vapor cell with ^{85}Rb and enriched ^{129}Xe-^{131}Xe. The Rb is optically pumped using D1 light propagating parallel to a DC bias field. SE collisions between the polarized Rb and Xe atoms polarize the Xe nuclei parallel to the bias field. Because of this configuration, the contribution of the Rb SE field to the Xe precession is substantial ($S_z >> 0$). Xe isotopes were chosen in order to suppress the influence of the Rb SE field on their comagnetometry ($b_S^a = 1.002\ b_S^b$[Bulatowicz et al. (2013); Petrov et al. (2019)]). Because ^{131}Xe has a nuclear spin of 3/2, the comagnetometer signal is sensitive to varying electric field gradients near the cell walls [Wu et al. (1988)].

This device has demonstrated kHz level rotation sensing bandwidth limited only by the lowest Larmor precession frequency of the two isotopes. The scale-factor is unity and is very

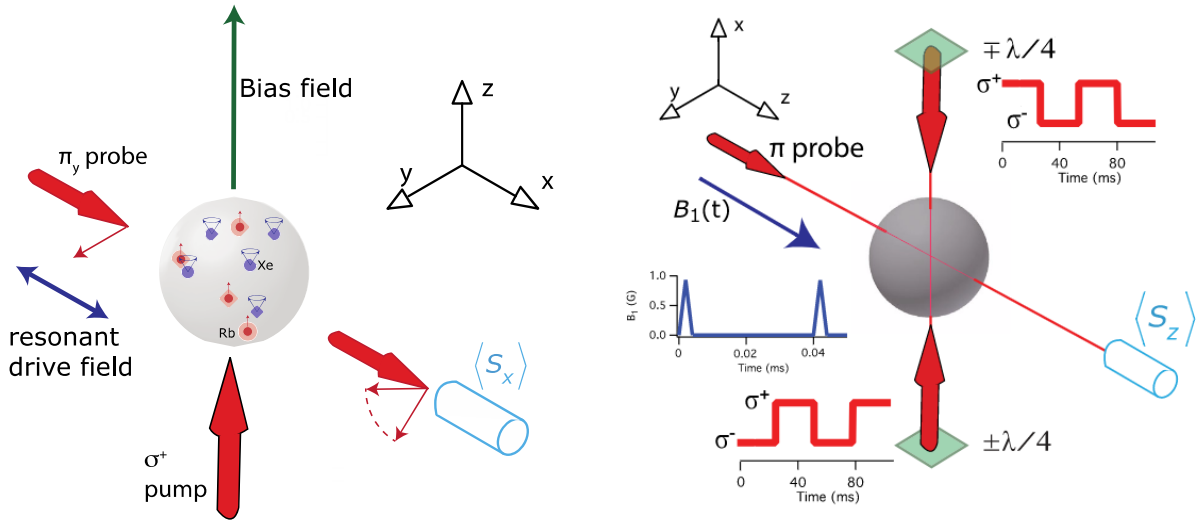

Figure 1.3: Left: schematic of longitudinal comagnetometer configuration used in the NGC-gryo. Right: schematic of transverse comagnetometer configuration described in this thesis.

uniform across the entire sense bandwidth. We should note that it is the only NMR-gryo to date whose scale factor stability has been measured. The short term noise is higher than other methods purportedly from quantization noise. The best long term stability is on the order of 10's nHz. This is the most miniaturized and fieldable NMR-gyro demonstrated thus far.

Self-compensating non-magnetometer

The self-compensating (SC) non-magnetometer utilizes the interaction between polarized alkali atoms and noble gas nuclei to measure NMSI [Kornack and Romalis (2002); Kornack (2005)]. It operates by applying a compensation field which largely cancels the nuclear magnetization experienced by the alkali-metal atoms thereby allowing both alkali-metal atoms and noble gas nuclei to be brought into resonance despite vastly different gyromagnetic

ratios. The measured comagnetometer signal, under this "self-compensating" condition, is proportional to the difference in field coupling to the two spin species. Since both spin species occupy the same volume they experience the same classical magnetic field. Each spin species' sensitivity to NMSI is likely not the same. Hence, the signal from the device is first order insensitive to magnetic fields while retaining sensitivity to NMSI. This device is not a comagnetometer as defined in this chapter because it has only one observable.

The device was originally demonstrated using ^{3}He-K [Kornack et al. (2005)] and has demonstrated lower short term noise than SE pumped comagnetometers. The long term stability is similar to other state of the art devices, roughly 10 nHz. The scale factor of this device depends on how well the compensation field cancels the nuclear magnetization and therefore requires calibration (non-physics scale factor). It has been used to put the most stringent upper bounds on LLIV [Brown et al. (2010)] and anomalous spin-mass couplings for Compton wavelengths greater than 1 cm [Vasilakis et al. (2009); Lee et al. (2018)]. Researchers have extended the SC non-magnetometer using modulation techniques to allow for dual axis rotation sensing with excellent noise performance [Jiang et al. (2018)].

Pulsed FID comagnetometer

The first demonstration of a free induction decay (FID) SE pumped comagnetometer was in 2013 using a ^{129}Xe-^{131}Xe comagnetometer [Bulatowicz et al. (2013)]. Again, these isotope's were chosen because of their similar SE enhancement factors. A new pulsed FID comagnetometer was recently demonstrated using ^{3}He-^{129}Xe-^{87}Rb [Limes et al. (2018)]. While the difference of the enhancement factors of these noble gas species ($b_S^{\mathrm{Xe}} = 110\, b_S^{\mathrm{He}}$[Ma et al. (2011)]) is much greater than for ^{129}Xe-^{131}Xe, the influence of time average S_z was greatly suppressed by applying transverse magnetic field pulses in concert with polarization modulation of the alkali-metal atoms. When the area of the transverse magnetic field pulses produce π precession of the Rb atoms, the coupling between the Rb atoms and Xe nuclei

Group	Bandwidth (Hz)	ARW (deg/rt Hr)	Bias (deg/Hr)
NGC[1]	300	0.005	<0.02
FID[2]	0.003	0.025	<0.01
SC[3]	10	0.006	0.05
This work	1	0.15	1

Table 1.2: Summary of performance of SE pumped comagnetometers. ARW is angle-random-walk. All but the SC have physics scale factors. References: 1: Walker and Larsen (2016), 2: Limes et al. (2018), 3: Jiang et al. (2018)

due to SE fields is greatly suppressed. This scheme enabled comagnetometer stability similar to that achieved with the SC non-magnetometer ($\sim$10 nHz) while realizing a "physics" scale factor. The sensitivity bandwidth of the device is very limited (< 0.01 Hz). In addition, the rate at which the device averages noise is orders of magnitude slower than the observed SNR suggests. This discrepancy could be due to non-linearity in the Rb magnetometer because of the large noble gas spin-exchange fields it senses.

This scheme was used to make the first measurement of the through space J-coupling between ^{3}He and ^{129}Xe [Limes et al. (2019)] and is currently being used to search for low frequency dark matter. Some of the performance metrics which have been measured in all three of the devices mentioned thus far are summarized in Table 1.2.

1.4 This work

The device demonstrated in this thesis, a schematic of which is shown in Fig. 1.3, is a SE pumped ^{131}Xe-^{129}Xe comagnetometer which produces no first-order time-averaged S_z or K_z such that the comagnetometer signal

$$\xi \equiv \frac{\rho\Omega^b - \Omega^a}{1+\rho} \approx \frac{\rho X_z^b - X_z^a}{1+\rho} \tag{1.5}$$

is independent of magnetic fields and longitudinal SE fields, where the superscripts a and b refer to ^{129}Xe and ^{131}Xe, respectively, and $\rho = 3.373417(38)$ [Makulski (2015)]. Similar to the NGC-gryo, the bandwidth of the device is limited only by the lowest Larmor frequency of the two isotopes. The scale factor between the Larmor resonance frequencies and NMSI is determined predominantly by fundamental physical constants, namely the gyromagnetic ratios. It is, to a good approximation [Brinkmann et al. (1962)], independent of the details of our apparatus (such as temperature, gas pressures, etc.). This means that comagnetometry can be performed without the need for calibration (in contrast with the SC non-magnetometer).

Longitudinal alkali-metal atom and noble gas nuclear polarization are avoided by optically pumping ^{85}Rb atoms transverse to a low duty cycle pulsed bias field. The pulse area of each bias field pulse is chosen such that the Rb spins precess 2π radians during each bias pulse. The Xe isotopes precess only $\sim 2\pi/10^3$ radians per pulse (owing to their much smaller magnetic moments). As such, we can approximate the effective bias field experienced by the Xe isotopes due to the pulses as a continuous function,

$$B_p(t) = \omega_p(t)/\gamma^S, \tag{1.6}$$

where $\omega_p(t)$ is the repetition rate of the 2π pulses and $\hbar\gamma^S = 2\mu_B/(2I+1)$, where $I = 5/2$ is the ^{85}Rb nuclear spin and μ_B is the Bohr magneton. Because of the low duty cycle nature of the pulses, the polarized atoms and nuclei are at zero field most of the time. This allows for SE collisions to transfer angular momentum from the Rb to the Xe (thereby polarizing the Xe nuclei) and for the Rb to precess due to each Xe isotope's SE field (thereby sensing the Xe nuclear precession). Both Xe resonances are simultaneously excited by either modulating the polarization of Rb atoms at the Xe resonance frequencies or by modulating the repetition rate of the bias field pulses at subharmonics of the Xe resonance frequencies. The results of each excitation method are summarized in the sections below.

Polarization Modulation

Modulating the handedness of polarization of the transversely oriented D1 pump laser produces a modulated transverse Rb polarization. Insofar as the pump polarization modulation (PM) has Fourier coefficients near each Xe resonance (as determined by the average bias pulse repetition rate and stray magnetic field) then transversely polarized Xe will be excited. Chapter 2 gives a detailed derivation of this process using the Bloch equation.

Chapter 3 provides a detailed description of the experimental apparatus and the various diagnostic measurements we made to characterize the PM comagnetometer. We find that PM suppresses time averaged S_z by at least 2500x while simultaneously realizing 1% and 0.1% transverse polarization for ^{129}Xe and ^{131}Xe, respectively. The effective SNR is roughly 5000 $\sqrt{\text{Hz}}$ and the bias instability is less than 1 μHz. The field suppression factor, defined as ξ's response to bias field modulation divided by ^{131}Xe's frequency response, was greater than 100.

We found that our detection scheme for PM caused roughly 10% of ^{129}Xe's phase information to show up in ^{131}Xe phase's detection channel and vice verse. This cross talk is undesirable as it is subject to variation and changes the scale factor of the comagnetometer. It was in pursuit of solving this cross talk issue that lead us to attempt exciting the Xe isotopes without modulating the Rb pump polarization. Modulating the pump polarization (as will be discussed extensively in Chapter 3) reverses the gain of the magnetometer and produces optical pumping transients. These gain reversals plus transients complicate the detection fidelity of the Xe phase of precession. Ideas developed in Ch. 4 should, if applied to the PM comagnetometer, greatly reduce these effects.

Bias Pulse Density Modulation

The pulsed nature of the bias field we implement enables the novel ability to apply bias field modulations which are experienced much more strongly by the Xe nuclei than by the Rb

atoms. This is due to the 2π precession each pulse causes the Rb to undergo. In the low duty cycle limit, the Rb would not be able to distinguish any change in pulse density. We use this novel capability to excite both Xe isotope's nuclei simultaneously without modulating the polarization of the D1 pump laser light. Although abandoning PM compromises the suppression of time averaged S_z, doing so allowed us to explore new detection schemes which addressed the cross talk issue we discovered when performing PM. Chapter 2 provides a detailed derivation using the Bloch equation reviewing how modulating the bias pulse density produces transversely polarized Xe in a continuous fashion.

Chapter 4 provides a detailed description of the experimental apparatus and the various diagnostic measurements we made to characterize the bias pulse density modulation (PDM) comagnetometer. We measure an ARW of 7 $\mu\text{Hz}/\sqrt{\text{Hz}}$ and bias instability of roughly 1 μHz. The field suppression was found to be 1800. We found that first order treatment of the influence of magnetometer phase shifts due to stray magnetic fields (see Ch. 2) resulted in order-of-magnitude improvements to the field suppression. This improvement should not be unique to PDM comagnetometry and we expect applying similar methods to the PM comagnetometer would similarly improve the field suppression. The cross talk was reduced by an order of magnitude for both isotopes compared to PM. We attribute this improvement to suppressed gain modulation.

The demonstrated performance of the PDM comagnetometer compared to other state of the art comagnetometers is shown in Table 1.2. Both the noise and stability are limited by unknown systematic errors. However, despite the excited Xe SE field being 30 times smaller than the FID comagnetometer, the ARW is only 6x greater at 230 times the bandwidth. While the ARW and bias instability of the comagnetometer is not more impressive than other state of the art comagnetometers, the novel first order suppression of longitudinal SE fields makes continued efforts to reduce limiting systematics a worthwhile venture. It is clear that the chip-scale comagnetometers of the future will require reliable suppression of these longitudinal SE fields. The comagnetometer described in this thesis is the only comagnetometer known

to the author which suppresses longitudinal SE fields while maintaining sense bandwidth.

Chapter 5 describes possible future improvements to transverse comagnetometry including discussion of the use of ^{3}He-^{129}Xe vapor cell and exciting the noble gases using a hybrid technique including both PM and PDM. Chapter 5 also discusses how the demonstrated stability should be sufficient to reduce the upper bound on spin-mass couplings by an order of magnitude for Compton wavelengths less than 1 mm [Bulatowicz et al. (2013)]. In addition, the through space J-coupling between ^{129}Xe and ^{131}Xe, which has yet to be measured, should also be well resolved by this device.

Chapter 2

Theory

When the facts change, I change my mind. What do you do sir?

— Lord John M. Keynes

This chapter demonstrates how we model the Rb and noble gas polarizations using Bloch equations. Steady state solutions are found for two excitation methods: polarization modulation and pulse density modulation. We show how the Rb SE field, if left uncompensated, produces broadening of the NMR. We also show how the presence of stray B_z produces a magnetometer phase shift which influence both the drive and detection of the Xe Larmor resonance. We review the influence of photon shot noise on the comagnetometer and estimate the photon shot noise limited rotation sensitivity.

2.1 The Bloch equation

Xe nucleus

The two dominant interactions which govern the precession of noble gas nuclei in the pressence of polarized alkali-metal atoms are magnetic fields and spin-exchange collisions. Of course, the many non-magnetic spin-dependent interactions mentioned in Chapter 1 will

also contribute to noble gas precession. We will add these after establishing the dominant interactions.

We begin by considering the influence of magnetic fields. Following [Walker and Larsen (2016)], the Hamiltonian describing the energy of a nuclear spin $\mathbf{K}$ immersed in a magnetic field $\mathbf{B}$ can be written as $H = -\hbar\gamma\mathbf{B}\cdot\mathbf{K}$. Applying Ehrenfests's theorem we find

$$\frac{d\langle\mathbf{K}\rangle}{dt} = \frac{-i}{\hbar}\langle[\mathbf{K}, H]\rangle = i\gamma\langle[\mathbf{K}, K\cdot\mathbf{B}]\rangle = -\gamma\mathbf{B}\times\langle\mathbf{K}\rangle, \tag{2.1}$$

which is simply the equation for a magnet in a magnetic field and is often referred to as the Bloch equation in NMR literature. For convenience we drop the $\langle\rangle$ notation. We find it useful to describe the nuclear polarization in terms of components perpendicular and parallel to a uniform bias field, $\mathbf{K} = K_z\hat{z} + \mathbf{K}_\perp$. In addition, a phasor notation enables ease of describing the amplitude and phase, defining $K_+ = K_x + iK_y = K_\perp e^{-i\phi}$ where $\phi = \gamma^K \int B_z dt$.

Spin-exchange between alkali-metal atoms and noble gas nuclei is mediated by the Fermi-contact hyperfine interaction [Walker and Happer (1997)]. The energy of this interaction can be written as

$$H_{SE} = \alpha(r)\mathbf{S}\cdot\mathbf{K}, \tag{2.2}$$

where $\mathbf{S}$ is the alkali-metal polarization vector, $\alpha(r)$ is the coupling strength, and r the inter-atomic separation between the two species. This coupling enables spin transfer from $\mathbf{S}$ to $\mathbf{K}$ (and vice verse) through collisions between atom pairs and three-body collisions that form weakly bound Rb-Xe van der Waals (vdW) molecules. This interaction also produces effective magnetic fields hence forth referred to as SE fields. These fields are conventionally

compared to the magnetic field produced by a fictional uniform magnetization as follows,

$$B_S^K = -\kappa_{XeRb}\frac{8\pi\mu_B}{3}n_S S = b_S^K S, \tag{2.3a}$$

$$B_K^S = \kappa_{RbXe}\frac{8\pi g_K\mu_N}{3}n_K K = b_K^S K. \tag{2.3b}$$

Here, n is the respective atom density, μ is the respective magnetic moment, and κ is the so called enhancement factor. The notation B_S^K is read as "the SE field produced by $\mathbf{S}$ as experienced by $\mathbf{K}$". An enhancement factor greater than one suggests a quantum amplification of the experienced dipolar magnetic field. The enhancement factor for Rb-Xe has been measured to be $\kappa_{RbXe} = \kappa_{XeRb} = 518(8)$ [Nahlawi et al. (2019); Ma et al. (2011)]. Such a large enhancement factor stems from the high probability of finding the Rb valence electron inside the Xe nucleus [Grover (1978); Schaefer et al. (1989)].

Similar to the Fermi-contact hyperfine interaction between alkali-metal atoms and noble gas nuclei, there also exists a spin-spin coupling $\mathbf{I^a}\cdot\mathbf{I^b}$ between the two noble gas species [Limes et al. (2019)]. This so called through-space J-coupling exists due to second order electron interactions which take place in Xe-Xe vdW molecules and depends on the vapor cell geometry. This interaction also produces an effective magnetic field which we write as $B_{K'}^K = b_{K'}^K(\kappa_{XeXe})K'$. No measurement of κ_{XeXe} yet exists but it is calculated to be -0.34 [Vaara and Romalis (2019)]. We discuss recent measurements of κ_{XeHe} in the Princeton FID comagnetometer and motivate its geometric dependence in Ch. 5.

Taking into account the influence of SE collisions, the Bloch equation becomes

$$\frac{d\mathbf{K}}{dt} = -\mathbf{\Omega}\times\mathbf{K} - \Gamma\mathbf{K} + \Gamma_S^K\mathbf{S}, \tag{2.4}$$

where $\mathbf{\Omega} = \gamma(\mathbf{B} + b_S^K\mathbf{S} + b_K^S\mathbf{K'} + \mathbf{X})$, $\mathbf{X}$ represents non-magnetic spin-dependent interactions, $\mathbf{K'}$ represents a second nuclear spin species, Γ is the total relaxation rate of the noble gas nuclei, and Γ_S^K is the SE pumping rate. The total relaxation rate Γ is dominated by SE

collisions, cell wall interactions, and magnetic field gradients. Since our apparatus is in a magnetic shield we presume magnetic field gradients to have a negligible contribution to Γ. Furthermore, the largest magnetic field is the pulsed bias field whose orientation defines $\hat{z}$. For both PM and PDM comagnetometry the time average of the Rb polarization is orthogonal to the bias field so that $\mathbf{S} = S_+\hat{+}$. Finally we can write the Bloch equation as two equations describing the transverse and longitudinal noble gas nuclear polarizations as

$$\frac{dK_+}{dt} = -(\mp i\Omega + \Gamma_2)K_+ + \Gamma_S^K S_+ + \mp i\Omega_+ K_z, \tag{2.5a}$$

$$\frac{dK_z}{dt} = \mp(\Omega_y K_x - \Omega_x K_y) - \Gamma_1 K_z, \tag{2.5b}$$

where Γ_1 is the longitudinal relaxation rate and $\Gamma_2 = 1/2\pi T_2$ is the transverse relaxation rate. Since $\gamma^a < 0$ and $\gamma^b > 0$ we find it useful to write γ (and hence Ω) as a positive value. The sign is written explicitly out front (top sign is for a, bottom sign is for b). We find this useful when we solve for steady state solutions to the Bloch equation.

SE Broadening: Before moving on to describing the Bloch equation for the Rb atom, it is important to note the influence of the $i\Omega_+ K_z$ term. The transverse field experienced by the Xe can be written as $\Omega_+ = \gamma^K(B_+ + b_S^K S_+)$. The term $b_S^K S_+$ is of order 100 μG. This substantial SE field can produce a torque on the Xe nuclei causing them to tip into $\hat{z}$ and consequently broaden the measured NMR linewidth. Such SE broadening can be suppressed by applying a magnetic field B_+ to cancel $b_S^K S_+$ thereby restoring the NMR linewidth to the Γ_2 limit [Korver et al. (2015); Korver (2015)]. Because $b_S^K S_+$ us much less than the magnetic width of the magnetometer, the performance of the magnetometer is not degraded by the presence of the compensation field. For the analysis which follow we begin by assuming that $B_+ = b_S^K S_+$ so that we can ignore the term $i\Omega_+ K_z$. We then explore $B_+ \neq b_S^K S_+$ for the case of PDM excitation.

Rb atom

The Rb atoms serve two primary purposes in our system: we use the DC transversely polarized Rb S_+ to polarize the Xe nuclei and the AC longitudinally polarized Rb S_z to detect the Xe precession. For $\Omega << \Gamma'$ the time-average solution to the Bloch equations for the Rb polarization

$$\mathbf{S} = \frac{\mathbf{R}\Gamma' + \mathbf{\Omega} \times \mathbf{R} + \mathbf{\Omega}(\mathbf{\Omega} \cdot \mathbf{R})/\Gamma'}{\Gamma'^2 + \mathbf{\Omega}^2} \tag{2.6}$$

can be expanded as

$$\mathbf{S} = \frac{\mathbf{R}}{\Gamma'} + \frac{\mathbf{\Omega} \times \mathbf{R}}{\Gamma'^2} + \frac{\mathbf{\Omega} \times \mathbf{\Omega} \times \mathbf{R}}{\Gamma'^3} + ..., \tag{2.7}$$

where $\mathbf{R} = \int \Phi(\nu)\sigma(\nu)/A \; d\nu$ is the pumping rate, $\sigma(\nu)$ is the cross section of the atomic transition, $\int \Phi(\nu) \; d\nu = P/h\nu$ is the total photon flux for a beam of power P incident an area A, Γ' is the total relaxation rate (including pumping), and $\mathbf{\Omega} = \gamma^S \mathbf{B}$ where $\mathbf{B} = b_a^S \mathbf{K}^a + b_b^S \mathbf{K}^b$ is the magnetic field experienced by the Rb. Note how the bias field does not appear in the field experienced by the Rb. This is because the bias field is applied as a sequence of low duty cycle pulses, the area of which correspond to 2π precession of the Rb atom. These equations assume negligible back polarization from the Xe to the Rb [Limes et al. (2018)], and that $\mathbf{K}$ precesses slowly such that S_z responds adiabatically. Since we optically pump along $\hat{x}$ we have $\mathbf{R} = R(t)\hat{x}$, and

$$S_+ = \frac{R(t)}{\Gamma'} + i\frac{R(t)\Omega_z}{\Gamma'^2} = \frac{R(t)}{\Gamma'} e^{i\epsilon_z}, \tag{2.8a}$$

$$S_z = -\frac{R(t)}{\Gamma'^2}(\Omega_y - \frac{\Omega_z}{\Gamma'}\Omega_x) = \frac{-R(t)}{\Gamma'^2}\mathrm{Im}[\gamma^S b_K^S K_+ e^{-i\epsilon_z}], \tag{2.8b}$$

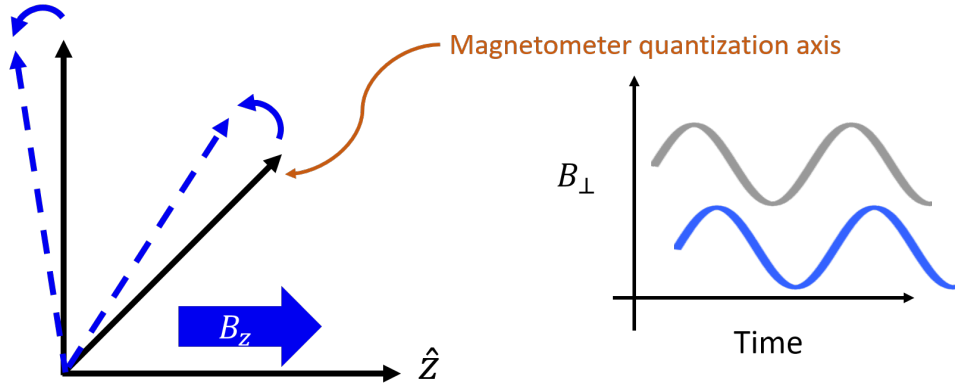

Figure 2.1: Cartoon depicting the influence of the stray field B_z on the phase of a rotating $B_\perp$ as measured by the Rb magnetometer.

where

$$\epsilon_z = \tan^{-1}(\frac{S_y}{S_x}) \equiv \tan^{-1}(\frac{B_{z0}}{B_w}) << 1 \tag{2.9}$$

is the magnetometer phase shift. $B_w = \Gamma'/\gamma^S$ is the magnetic width of the magnetometer. Figure 2.1 depicts how a stray B_z effectively rotates the quantization axis of the Rb magnetometer thus causing a phase shift in the measurement of a rotating $B_\perp$. We will show in Ch. 2.5 that the derivative of this phase shift appears as a rotation. In Ch. 4.4 we demonstrate that accounting for ϵ_z enables order of magnitude improvement in the field suppression of the PDM comagnetometer.

Having motivated the Bloch equations describing the Rb atom and noble gas nuclear polarizations we can consider PM and PDM excitation individually.

2.2 Polarization modulation

For PM excitation the Xe NMR are driven by modulating the transverse Rb polarization near each isotopes resonance frequency while the average bias pulsing frequency is kept fixed. Hence, we set $S_+(t) = e^{i\epsilon_z}\left(\sum_p s_p e^{ip\omega_1 t} + \sum_q s_q e^{iq\omega_2 t}\right)$ and $B_z = B_{z0} + B_p$ where $B_p = \omega_p/\gamma^S$,

B_{z0} is the stray field inside our magnetic shields, and s_i is the Fourier coefficient of S_+ at ω_i. With the substitution $K_+ = K_\perp e^{\pm i(\omega_d t+\delta)}$, where δ is the phase shift of the Xe relative to the phase of S_+ we find the real part of Eq. 2.5a to be

$$\frac{dK_\perp}{dt} = -\Gamma_2 K_\perp + \Gamma_S^K[s_p\cos((p\omega_1+\omega_d)t+\delta\pm\epsilon_z) + s_q\cos((q\omega_1+\omega_d)t+\delta\pm\epsilon_z)] \quad (2.10)$$

where the summations over p and q are omitted for convenience and we have assumed that $\Omega_+ = 0$. The steady state solution of this equation is $K_\perp = \Gamma_S^K\left(s_p+s_q\right)/\Gamma_2$ when ω_d is chosen such that the resonance condition $\omega_d + p\omega_1 = q\omega_2 + \omega_d \sim 0$ is satisfied and $\delta, \epsilon_z << 1$. Similarly, the imaginary part of Eq. 2.5a (once again for $\delta, \epsilon_z << 1$) is

$$\frac{d\delta}{dt} = -\Delta - \Gamma_2(\delta \mp \epsilon_z), \quad (2.11)$$

where $\Delta = \omega_d - \gamma B_z$. The sign in front of ϵ_z is isotope dependent because the Xe isotopes precess in opposite directions. We can solve this equation in the Fourier domain and find

$$\tilde{\delta} = -\frac{\tilde{\Delta} \pm \Gamma_2\tilde{\epsilon}_z}{\Gamma_2 + i\omega}, \quad (2.12)$$

where the notation $\tilde{f} = f(\omega)$ is utilized.

2.3 Pulse density modulation

For PDM excitation we excite the transverse Xe polarization by modulating the pulsed bias field repetition rate ω_p instead of S_+. Hence, we set $S_+(t) = S_\perp$ =constant. The $\hat{z}$ component of the magnetic field experienced by the Xe nuclei is $B_z = B_{z0} + B_p(t)$, which includes the stray field B_{z0} and the bias field from the 2π pulses $B_p(t) = B_{p0} + B_m(t)$, where B_m is the modulated part of the pulsed field. The Xe nuclei experience both B_{z0} and B_p, but because the Rb atoms precess by 2π during each bias pulse, the Rb atoms

experience predominantly B_{z0}. Although one could modulate B_{z0} to excite the Xe NMR, the modulation depth required to do so efficienty would compromise the Rb magnetometer. We modulate ω_p as

$$\omega_p(t) = \omega_{p0}(1 + b_1 \cos(\omega_1 t) + b_2 \cos(\omega_2 t)), \tag{2.13}$$

where ω_1, and ω_2 determine the Xe drive frequencies, and $b_1 = B_1/B_{p0}$ and $b_2 = B_2/B_{p0}$ set the depth of modulation.

We measure the difference $\delta = \phi - \alpha$ between the instantaneous Xe phase ϕ and a reference phase $\alpha = \int(\omega_d + \gamma B_m)dt$ which is the phase the Xe would have if the only fields present were the pulsing fields and if $\Delta \equiv \omega_d - \Omega_0 = 0$ with $\Omega_0 = \gamma(B_{z0} + B_{p0}) + X_z$. We let $K_+ = K_\perp e^{\pm i(\alpha+\delta)}$. To first order in δ and ϵ_z, the real part of Eq. 2.5a is

$$\frac{dK_\perp}{dt} = -\Gamma_2 K_\perp + \Gamma_S^K S_\perp[\cos(\alpha) - (\delta \mp \epsilon_z)\sin(\alpha)]. \tag{2.14}$$

To find the time averages of $\cos(\alpha)$ and $\sin(\alpha)$ (and thereby arrive at a steady-state solution for $K_\perp$), consider the time average of $e^{i\alpha}$ for $B_m = B_1 \cos(\omega_1 t) + B_2 \cos(\omega_2 t)$. Making substitutions using the Jacobi-Anger expansion

$$e^{izsin\theta} = \sum_{n=-\infty}^{\infty} J_n(z) e^{in\theta}, \tag{2.15}$$

where $J_n(z)$ is the n-th Bessel function of the first kind, and keeping only terms of the sums that would mix to give a contribution at DC, we find the time averages $\overline{\cos(\alpha^K)} = J_{-p^K}(\frac{\gamma^K B_1}{\omega_1}) J_{-q^K}(\frac{\gamma^K B_2}{\omega_2}) \equiv j^K$ and $\overline{\sin(\alpha^K)} = 0$. The steady-state solution for $K_\perp$ is then

$$K_\perp = \frac{\Gamma_S^K S_\perp}{\Gamma_2} j^K \tag{2.16}$$

where p^K and q^K are chosen to satisfy the resonance condition $\omega_d^K = p^K \omega_1 + q^K \omega_2$.

The imaginary part of Eq. 2.5a is

$$\frac{d\phi}{dt} = \Omega - \frac{\Gamma_S^K S_\perp}{K_\perp} \sin(\phi \mp \epsilon_z). \tag{2.17}$$

To get an expression for δ, we make substitutions as given above and use the steady-state solution for $K_\perp$. To first order in δ and ϵ_z, we arrive at

$$\frac{d\delta}{dt} = -\Delta - \Gamma_2(\delta \mp \epsilon_z), \tag{2.18}$$

which is the same as Eq. 2.11 from PM excitation.

Influence of transverse fields

The expressions derived above are only valid when the transverse fields experienced by the noble gas are negligible. Here we demonstrate their influence on the PDM comagnetometer. The transverse fields experienced by the Xe include both classical fields (such as those from moving charges) and SE fields. We write $B_+ = B_x + iB_y = (B_{x0} + b_S^K S_x) + i(B_{y0} + b_S^K S_y) = B_{+0} + b_S^K S_+$ where B_{+0} are the classical fields and $b_S^K S_+$ are the SE fields from polarized Rb atoms. The steady state solution of Eq. 2.5b is

$$K_z = \frac{j^K \gamma^K K_\perp}{\Gamma_1}(\overline{B}_y + \overline{B}_x \delta^K). \tag{2.19}$$

Note how K_z depends on the total (classical plus SE) average transverse magnetic fields. Additionally, a DC B_y produces K_z but a DC B_x produces a K_z only when $\delta^K \neq 0$. Using the steady state solution for K_z we can solve for the imaginary part of Eq. 2.5a to first order in δ and find,

$$\frac{d\delta^K}{dt} = -\Delta^K - \Gamma_2^K \left[\eta^K \overline{B}_y \overline{B}_x \mp \epsilon_z\right] - \Gamma_2 \, \delta^K \left[1 + \eta^K (\overline{B}_x^2 + \overline{B}_{y0} \overline{B}_y)\right] \tag{2.20}$$

where $\eta^K = (j^K\gamma^K/\Gamma_2^K)^2$. Note how this expression is equal to Eq. 2.18 when $\overline{B}_x = \overline{B}_y = 0$. We see that the product $\overline{B}_x\overline{B}_y = (\overline{B}_x + b_S^K\overline{S}_x)(\overline{B}_y + b_S^K\overline{S}_y)$ causes a phase shift of the noble gas while $\overline{B}_x^2 - \overline{B}_{y0}\overline{B}_y$ causes broadening of Γ_2 [Korver et al. (2015)]. The results of this derivation are applicable to PM excitation with the caveat that the PM comagnetometer is only sensitive to transverse fields that are resonant (co-precess) with the Xe.

2.4 Performance Limits

In Ch. 1 we mentioned that an important motivation for developing a new type of noble gas comagnetometer was because, to date, all demonstrated devices where limited by technical noise sources. Any proposal for a new scheme which suppresses systematic error would only be of interest if its fundamental noise remained similar to other schemes. In this section we derive estimates for how the photon shot noise limits the performance of a SE pumped comagnetometer.

Photon Shot Noise

We detect S_z via Faraday rotation. A linearly polarized diode laser, or probe laser, whose frequency is tuned near the D2 line of Rb is directed along $\hat{z}$ parallel to the bias field produced by the pulsing coils. Linearly polarized light is a superposition of $\sigma^{\pm}$ components. These components are absorbed/phase-shifted differently as they propagate through a spin-polarized vapor effectively rotating the angle of linear polarization Φ_F of the probe proportional to S_z. We write,

$$\Phi_F = \beta_0 S_z S_\infty \frac{\Delta}{W(1 + 4\Delta^2/W^2)} \approx \beta_0 S_z S_\infty \frac{W}{4\Delta}, \tag{2.21}$$

where $\beta_0 = n_S l \sigma_0$ is the optical depth at line center, $\sigma_0 = \sigma_{max} W_{raditation}/W_{pressure}$ is the cross section, n_S is the alkali-metal atom number density, l is the probe's path length through

the cell, W is the width of the D2 resonance, Δ is the detuning from resonance, and S_∞ characterizes the degree of circular dichroism of a transition (J = (1/2,3/2), $S_\infty = (1, 1-/2)$). The approximation holds for $\Delta >> W$. The following logic approximates the photon shot noise limit of the magnetometer noise good to a factor of two or so. For a more careful calculation see [Romalis (2013)]. If we assume the maximum value of Φ_F is of order unity (call it 1/4 for convenience) then the Δ which produces this Φ_F is $\Delta = W\sqrt{\beta_0}$. Operating at this Δ for the D2 transition ($S_\infty = -1/2$) implies $\Phi_F = -\sqrt{\beta_0}S_z/8$. The measurement of Φ_F is (ideally) limited by shot noise due to the particle nature of photons so that $\delta\Phi_F = 1/2\sqrt{\Phi}$ where Φ is the photon flux. Finally, from Eq. 2.7 we write $S_z = -\gamma^S B_y S_x/\Gamma' = -S_x B_y/B_w$. So the uncertainty in the measurement of B_y using Faraday rotation is

$$\delta B_y = \frac{4B_w}{S_x\sqrt{\Phi\beta_0}}. \tag{2.22}$$

We normally use 1 mW of detected probe photons so that $\Phi = \frac{1\text{ mJ}}{\text{sec}}\frac{1\text{ eV}}{1.6\times10^{-19}\text{ J}}\frac{\text{photons}}{1.6\text{ eV}} = 3\times10^{15}\frac{\text{photons}}{\text{sec}}$. Our vapor cells have sufficient Xe and N_2 buffer gas to pressure broaden the D2 transition width at room temperature from $W_{radiation} = 6$ MHz to $W_{pressure} \approx 6$ GHz such that $\sigma_0 = 2\times10^{-9}\text{ cm}^2\frac{6\text{ MHz}}{6\text{ GHz}} = 1\times10^{-12}\text{ cm}^2$. The cell is heated such that $n_S \approx 10^{13}\text{ cm}^{-3}$. With a $l = 1$ cm path length these criterion produce an effective optical depth at line center of $\beta_0 \approx 30$. The pump detunings and pump power are chosen to balance the time average of the AC stark effect [Korver (2015)] while producing $S_x \approx 1/2$. In practice we measure $B_w \approx 3$ mG ($\Gamma' \approx 50000\text{ sec}^{-1}$) which is similar to what we predict using data from the literature (see App. A). Evaluating Eq. 2.22 with these numbers lead to $\delta B_y \approx 80\text{ pG}/\sqrt{\text{Hz}}$ or 8 $\text{fT}/\sqrt{\text{Hz}}$. Although δB_y can be reduced by increasing the probe power, a realisitic probe laser has some circular polarization which produces relaxation thereby increasing B_w. Hence, the probe laser's power can not be increased ad infinitum without degraded noise performance.

2.5 Comagnetometry

In App. A we estimate Γ_S^K and find that for PM and PDM excitation schemes the expected transverse SE field experienced by the Rb due the noble gas polarizations is roughly $B^K \approx 100\mu$G. In Sec. 2.4 we described how the photon shot noise limits the detection noise of the Faraday rotation measurement of S_z and how quantum projection noise places a lower bound on δ. In this section we derive expressions relating these fundamental noise processes to the comagnetometer's sensitivity to non-magnetic spin-dependent interactions.

Faraday detection allows us to measure δ. However, we desire to perform comagnetometry using the precession frequencies. One can either convert the measured phase to frequency using Eq. 2.12 or by creating a feedback loop which corrects ω_d to keep the measured phase $\delta \pm \epsilon_z \equiv 0$. The latter is desirable as Eq. 2.12 contains Γ_2 which is subject to change. The feedback to correct ω_d can be written as

$$\tilde{\omega_d} = \tilde{G}(\tilde{\delta} \pm \epsilon_z + \tilde{n}) \tag{2.23}$$

where G is frequency dependent gain (in units of 1/sec) and $n = (SNR)^{-1} = b_K^S K_\perp / \delta B_y$ is due to finite detection noise (such as photon shot noise). After correcting for finite gain, the drive frequencies become

$$\tilde{\omega}_d^* = \tilde{\omega_d}\tilde{G}^{-1}(i\omega + \Gamma_2 + \tilde{G}) = \tilde{\Omega}_0 \pm i\omega\tilde{\epsilon}_z + (i\omega + \Gamma_2)\tilde{n}. \tag{2.24}$$

We see that $\tilde{\omega}_d^*$ is not merely equal to the Larmor resonance of the noble gas but also depends on the SNR and derivative of the magnetometer phase shift.

The comagnetometer signal is constructed so as to cancel precession which is correlated according to each isotopes gyromagnetic ratio, hence

$$\tilde{\omega}^{co} = \rho\tilde{\omega}_d^{b*} - \tilde{\omega_d}^{a*} = \rho\tilde{X}_z^b - \tilde{X}_z^a + i\omega\tilde{\epsilon}_z(1+\rho) + \tilde{n}^b\rho(i\omega + \Gamma_2^b) - \tilde{n}^a(i\omega + \Gamma_2^a). \tag{2.25}$$

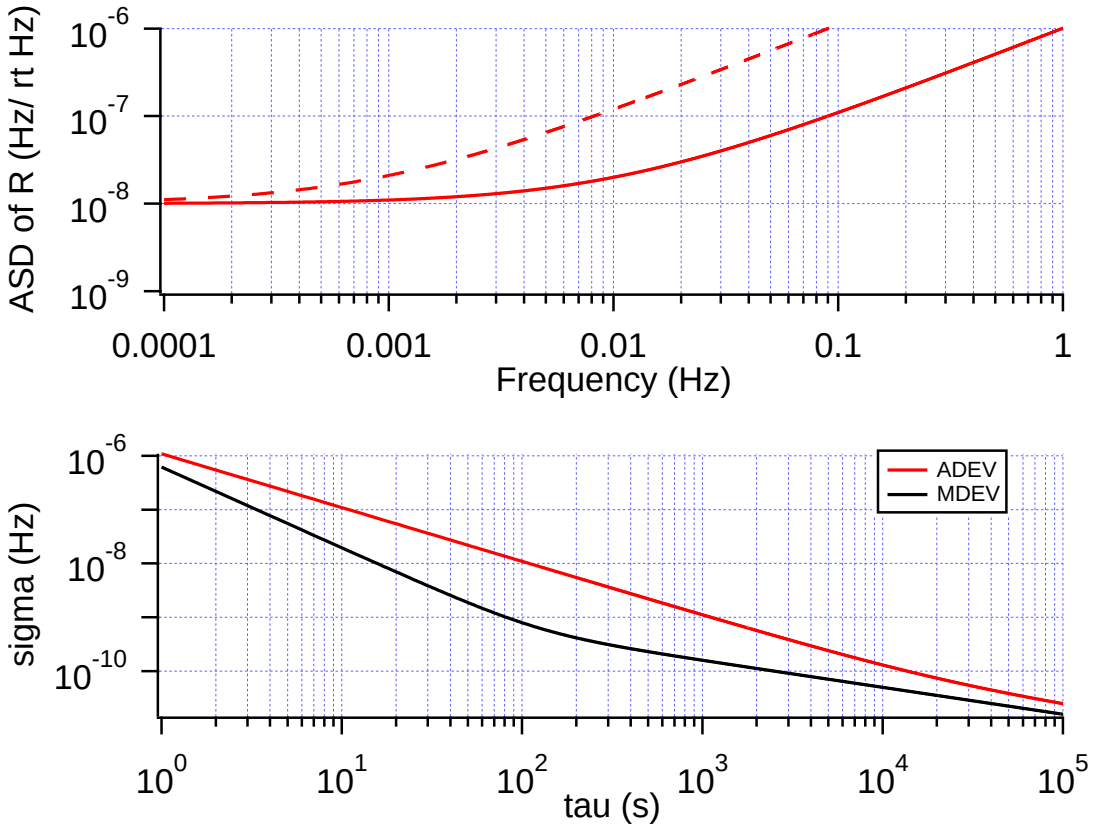

Figure 2.2: Influence of finite SNR on rotation sensitivity. Top panel is amplitude spectral density of $\tilde{R}$. Solid curve is for $\tilde{\epsilon}_z = 0$ whereas the dashed curve is for $\tilde{\epsilon}_z = 10\ \mu\text{rad}/\sqrt{\text{Hz}}$. Bottom shows ADEV and MDEV of solid curve from top panel assuming $f_c = 10$ Hz and $\tau_0 = 1$ s.

We see that the influence of finite SNR is minimized if $\rho\tilde{n}^b = \tilde{n}^a$, such that if the detection noise is the same for both isotopes then $b_K^S K_\perp^b = \rho\ b_K^S K_\perp^a$.

For the special case of detecting rotations $\tilde{X}_z^a = -\tilde{R}_z$ and $\tilde{X}_z^b = +\tilde{R}$ such that $\tilde{R} = \tilde{\omega}^{co}/(1+\rho)$. Figure 2.2 shows the anticipated rotation noise (amplitude spectral density) $\tilde{R}$ assuming the detected SE field is 100 μG for each isotope, the detection noise is 100 pG/$\sqrt{\text{Hz}}$ (so that $\tilde{n}^a = \tilde{n}^b = 10^{-6}$ rad/$\sqrt{\text{Hz}}$), and $\Gamma_2^a = \Gamma_2^b = 10$ mHz. The solid curve is for $\tilde{\epsilon}_z = 0$ whereas the dashed curve is for $\tilde{\epsilon}_z = 10\ \mu\text{rad}/\sqrt{\text{Hz}}$. We see that the finite SNR produces white noise of frequency ($S_y = h_0$, where S_y is power spectrum in units of Hz^2/Hz) for frequencies from 0 to Γ_2 and then white noise of phase ($S_y(f) = h_2 f^2$) for frequencies

$S_y(f)$	σ^2	$\sigma_{\mathbf{M}}^2$
$h_2 f^2$	$\frac{3h_2 f_c}{8\pi\tau^2}$	$\frac{3h_2 f_c \tau_0}{8\pi^2\tau^3}$
h_0	$\frac{h_0}{2\tau}$	$\frac{h_0}{4\tau}$

Table 2.1: Influence of ADEV and MDEV on white noise of phase (top) and flicker noise of phase (bottom). f_c is the cut off frequency of anti-aliasing (low pass) filter. τ_0 is the smallest integration time. The ADEV result assumes $2\pi f_c \tau >> 1$.

greater than Γ_2, where $h_2 = (\frac{\rho\tilde{n}^b + \tilde{n}^a}{1+\rho} + \tilde{\epsilon}_z)^2$ and $h_0 = (\frac{\rho\tilde{n}^b\Gamma_2^b + \tilde{n}^a\Gamma_2^a}{1+\rho})^2$.

A common technique for characterizing frequency stability is the Allan standard deviation (ADEV) [Vanier and Audoin (1989)]. Also known as the "second difference", this computation was developed to converge for flicker noise of frequency and random walk of frequency as the simple variance does not. The second difference is computed by dividing a time series of length T composed of frequency fluctuations $y(t)$ relative to a reference (with no dead time) into $n = T/\tau$ segments where τ is the averaging time. For each τ, the average fluctuation of each segment $\bar{y}(t)$ is computed and the square of the difference between two consecutive segments is summed together. We write

$$\sigma^2 = \frac{1}{2(n-1)} \sum_{i=0}^{n-1} (\bar{y}_{i+1} - \bar{y}_i)^2. \tag{2.26}$$

The influence of the ADEV on white noise of phase and white noise of frequency is shown in Table 2.1.

The modified Allan deviation (MDEV) [Allan and Barnes (1981)] was later developed to enable the distinction between white noise of phase and flicker noise of phase, which both trend as τ^{-1} for ADEV. It is an extension of the ADEV where the square of the difference of non-adjacent segment averages are also computed. We write

$$\sigma_M^2 = \frac{1}{2(n-1)} \sum_{i=0}^{n-1} \sum_{k=1}^{i} (\bar{y}_{i+k} - \bar{y}_i)^2. \tag{2.27}$$

The effect of this additional averaging is to distinguish white noise of phase from flicker noise of phase while minimally influencing the scaling of the other noise processes all at the cost of increased computation time. Table 2.1 shows the influence of MDEV on white noise of phase and white noise of frequency. Fig. 2.2 shows both the ADEV and the MDEV of $\tilde{R}$. We see that the MDEV averages the white noise of phase more quickly than the ADEV. For long integration times the ADEV and MDEV are both limited by white frequency noise.

In this section we have discussed how to use feedback to observe the noble gas Larmor resonance frequencies in real time. We have demonstrated how the magnetometer phase shift contributes to the measured resonance frequency. We have also described the comagnetometer signal and specifically addressed how finite SNR contributes to the noise and stability for measurements of non-magnetic spin-dependent interactions. For the case of photon shot noise limited comagnetometry, we find that the estimated rotation sensitivity is very promising compared to other state-of-the-art comagnetometers (see Ch. 1.3). A rotation frequency uncertainty of 10 nHz is reached in less than 100 s of integration, while maintaining 1 Hz measurement bandwidth.

2.6 Systematic noise sources

Before closing this chapter we would like to summarize some of the many sources of systematic error which can prevent the comagnetometer performance from being photon shot noise limited. Although this list is not exhaustive, it provides an excellent starting place for debugging poor performance. It also serves as an introduction to the topics explored in Chapters 3 and 4.

Longitudinal SE fields: we have already written at length about the influence of these fields. K_z is produced if both $\Delta \neq 0$ and the Rb SE field is not well compensated (both $\hat{x}$ and $\hat{y}$ directions). The Rb SE field itself depends on the pumping rate (pump power and detuning) and the number of Rb atoms (cell temperature).

Faraday rotation noise: Balanced polarimetry is an excellent experimental technique for realizing photon shot noise limited detection of Rb atom precession because probe laser amplitude fluctuations are suppressed to first order. The amount of suppression depends non-linearly on the time average of the photodiode balance (poor balance leads to poor amplitude noise rejection). We use two photodiodes tied anode to cathode to subtract the measured photo currents (also referred to as hard-wired subtraction). Thus, this balance must be set by hand. This balance is subject to drift due to: temperature dependent vapor cell quarter wave retardance, and stray B_y drifts producing S_z. There do exist so called auto-balancing circuits but they should be approached with caution as they can be difficult to optimize.

DAQ noise: The Faraday rotation difference current is sent to a current to voltage converter (with finite SNR) and the output voltage is digit ized using a 16 bit DAQ. The SNR of this DAQ is optimized when the full range ± 10 V is filled with signal. The gain of the current to voltage converter may not be turned up until the DAQ is filled because of the large junction capacitance of the large area photodiodes (turning up the gain too high effectively rolls off the response of the photodiodes). As such, we have a voltage amplifying stage after the current to voltage converter. The gain of this voltage amplifier is chosen so the digitized signal fills the DAQ.

pulsing noise: If the pulse area of the bias pulses fluctuate then we expect the white noise floor of the magnetometer to be degraded. Additionally we expect these fluctuations to produce noise on $\tilde{\epsilon}_z$. Since the PDM comagnetometer uses the bias pulses to excite the Xe, pulse area fluctations and pulse timing errors serve to limit the effective drive-to-noise ratio. Pulse timing errors only appear on the magnetometer and $\tilde{\epsilon}_z$ if the pulse area is not equal to 2π.

pump pointing: If the pump beam is oriented somewhat along $\hat{z}$ then we expect any noise due to optical pumping (from pump amplitude or detuning fluctuations) to appear on S_z, thereby degrading the effective noise floor of the magnetometer.

AC stark balance: The D1 pump photons produce an effective magnetic field which is experienced by the Rb atoms but not by the Xe nuclei and which depends on pump parameters. We suppress or balance the AC stark effect by pumping from with both red and blue detuned photons (the AC stark effect produces a magnetic field parallel to the handedness of polarization and dispersively dependent on the detuning of the pump photons). Poor AC Stark balance causes the Rb to experience a B_x which increases the magnetometer's sensitivity to B_z. This could increase the influence of bias pulsing noise on the magnetometer noise performance.

Drive to noise ratio: The Xe are effectively damped driven oscillators. If they are driven with a noisy source their precession will exhibit the same noise. Hence, the SNR of the detected Xe precession is bounded by the drive to noise ratio of the excitation method (whether that be PM or PDM).

Temperature drifts: When the temperature drifts many things change including; Rb density (and hence the ideal transverse compensation field and magnetometer gain), quadrupole frequency shifts, and Γ_2. According to Eq. 2.11, drifts in Γ_2 only lead to frequency drifts if the isotopes are driven off resonance.

2.7 Chapter Summary

In this chapter we have derived expression from the Bloch equation which describe the time dependence of the Xe and Rb polarizations. We find that purely transversely polarized Xe can be excited by either modulating the transverse Rb polarization or by modulating the bias field. We discussed how photon shot noise limits the SNR of the comagnetometer and estimated the resulting rotation sensitivity.

Chapter 3

Polarization Modulation Excitation

Thad: How many data points do you have?

Me: Four.

Thad: How many free parameters in your fit funciton?

Me: Three.

Thad: So... we aren't drowning in statistics...got it!

— Thad G. Walker

Compared to pulse density modulation (PDM) excitation, polarization modulation (PM) excitation has several advantages. PM excitation AC couples S_z thereby reducing its time average even more so compared to PDM excitation. From an experimental perspective, modulating the transverse polarization is readily achieved using off the shelf electro-optic modulators. This is in contrast to the PDM comagnetometer which requires a carefully designed pulsing circuit to produce high fidelity PDM.

In this chapter we demonstrate continuous comagnetometry by exciting the NMR of each Xe isotope by modulating only the handedness of light polarization between two states: σ^+ and σ^-. The excited SE field $b_K^S K_\perp$, and transfer function from phase to frequency for each isotope are in agreement with estimations (see App. A). The short term noise is measured

to be 16 μHz/$\sqrt{\text{Hz}}$, within a factor of 3 of the measured T_2 divided by the measured SNR. What limits the detection noise is uncertain. We have confirmed that the noise is not limited by the probe laser or detection electronics. The noise may stem from the dual frequency PM waveform itself. We find that correcting the bias field to keep the phase measured for isotope a equal to zero stabilized ω^b to 1 μHz under ideal conditions. The field suppression factor is greater than 100. We discovered that imperfect rectification of the dual frequency square wave PM waveform enables a few percent of the phase information from isotope a to show up in isotope b's detection channel and vice verse. This cross talk effectively changes the scale factor of the comagnetometer. The imperfection in rectification stems from not taking the optical pumping transients (due to PM itself) and frequency dependent phase shifts (due to high pass filtering S_z prior to rectification) into account. Implementing a sample and hold algorithm greatly suppressed the cross talk produced by optical pumping transients. Although removing the HPF improved the cross talk, it degraded the SNR by an order of magnitude because rectification maps $1/f$ noise to the Xe carrier (detection) frequencies.

In a desire to reduce the cross talk without sacrificing SNR we investigate sinusoidal PM using two different detection schemes dubbed $2f$ and S^{mod}. We find that producing reliable purely sinusoidal PM in our optically thick vapor cell to be extremely difficult. We find that non-linearities (modulate at ω and see its harmonics) depended not only on the state of polarization of the pump light but also other pump and probe settings. These non-linearities produced cross talk similar to that demonstrated with square PM. While the cross talk is reduced via sine PM, the superior performance difficult to maintain on a daily basis. Furthermore, the SNR of square PM was never reliably reproduced with sine PM. Table 3.1 summarizes results of the three schemes discussed in this chapter.

Much of the content of this chapter remains unpublished although it has been presented at various conferences the world over. The reason for our embargo is that there were many short comings of the PM comagnetometer which we were unable to resolve. The PDM comagnetometer demonstrated in Chapter 4 sheds much light on many of these issues. At

Scheme	Signal (μG)	C.T. (%)	ARW (μHz/$\sqrt{\text{Hz}}$)	Bias instability (μHz)
Sq., Rect., $1f$	70	3	16	0.8
Sine, $2f$	45	< 1	44	< 4
Sine, S^{mod}	40	< 1	44	< 4

Table 3.1: Summary of PM performance. The Bias instability listed is the minimum of the MDEV of $\tilde{\omega}^b$ when the bias field is corrected to keep the measured phase of isotope a equal to 0. C.T. stands for cross talk. The greatest cross talk (either from a onto b or vice verse) is listed. The Sine PM cross talk numbers are approximated by comparing Figs. 3.18 and 3.24

the time of writing, we are confident that, armed with the new knowledge from Chapter 4, we can overcome many of the issues presented in this Chapter.

We begin by reviewing the conclusions of Ch. 2 concerning PM. We then describe the PM comagnetometer apparatus and what we learned as we optimized each of its components. We then describe its performance as a comagnetometer giving special attention to anomalous cross channel signal leakage and its ramifications.

3.1 PM general principles

In Ch. 2 we showed that by modulating the transverse Rb polarization S_+ at two frequencies ω_1 and ω_2 the steady state transverse polarization of a single Xe isotope can be written as $K_\perp = \Gamma_S^K(s_p + s_q)/\Gamma_2$ as long as $\omega_d + p\omega_1 = q\omega_2 + \omega_d \sim 0$, where s_i is the Fourier coefficient of S_+ at ω_i. We choose $(p^a, q^a) = (1, 0)$ and $(p^b, q^b) = (0, 1)$ such that the resonance condition for each isotope is $\omega_1 = \omega^a$ and $\omega_2 = \omega^b$.

From Eq. 2.8 we find that the detected longitudinal Rb polarization S_z is

$$S_z = -\frac{R(t)}{\Gamma'^2}[b_a^S K_\perp^a \sin(\delta^a + \alpha^a - \epsilon_z) + b_b^S K_\perp^b \sin(\delta^b + \alpha^b + \epsilon_z)], \tag{3.1}$$

where $\delta = \phi - \alpha$ is the difference between the drive phase α and the Xe precession phase ϕ, ϵ_z is the magnetometer phase, and $R \sim S_+$ is the optical pumping rate of the Rb. Although

lock-in detection can be accomplished on S_z as it appears in Eq. 3.1, the phase sensitivity is diminished due to the presence of $R(t)$ which effectively mixes some phase information to DC. A more effective approach is to "rectify" the S_z signal such that $R(t)$ is removed.

3.2 Apparatus

Cell Mount

An 8 mm cubic Pyrex cell filled with 68 Torr enriched Xe and 85 Torr N_2 with a hydride coating [Kwon et al. (1981)] is mounted in a ceramic housing with holes for laser light to enter the cell. The ceramic housing has 4 symmetric faces which fit together like a jig saw puzzle. On each face is printed conductive traces through which AC at $\sim$ 150 kHz is passed to heat the ceramic. The conductive traces are arranged to produce minimal stray magnetic fields including gradient magnetic fields. The $\sim$ 1 mm gap between the vapor cell and ceramic heating jig is shimmed with a 1.5 mm thermally conductive and slightly compressible gap fill (model: TG 977, manufacturer: T-global Technology, see Fig. 3.1). The ceramic is wrapped with aerogel (a high temperature insulating material) and secured with Kapton tape and then fitted into a 3D printed (high temperature Nylon) cartridge with holes to allow laser light to enter the cell. The compressible nature of the aerogel produces a friction fit keeping the ceramic jig structure fixed within the cartridge. The cartridge itself is mounted in a 3-D printed (ABS plastic) rig. This rig has support arms which extend out three of the magnetic shield portholes. These support arms are secured directly to the optical table. The purpose of the rig is to secure the cell in the middle of (i) a set of 3 orthogonal square Helmholtz magnetic shim coils, (ii) the bias pulsing coils, and (iii) the shield. The rig was further designed to allow for the placement of the cell within the shield to be faithfully reproduced after swapping cells. Figure 3.1 shows photographs of the jig heaters and cartridge and Fig. 3.2 shows a drawing of the coil rig.

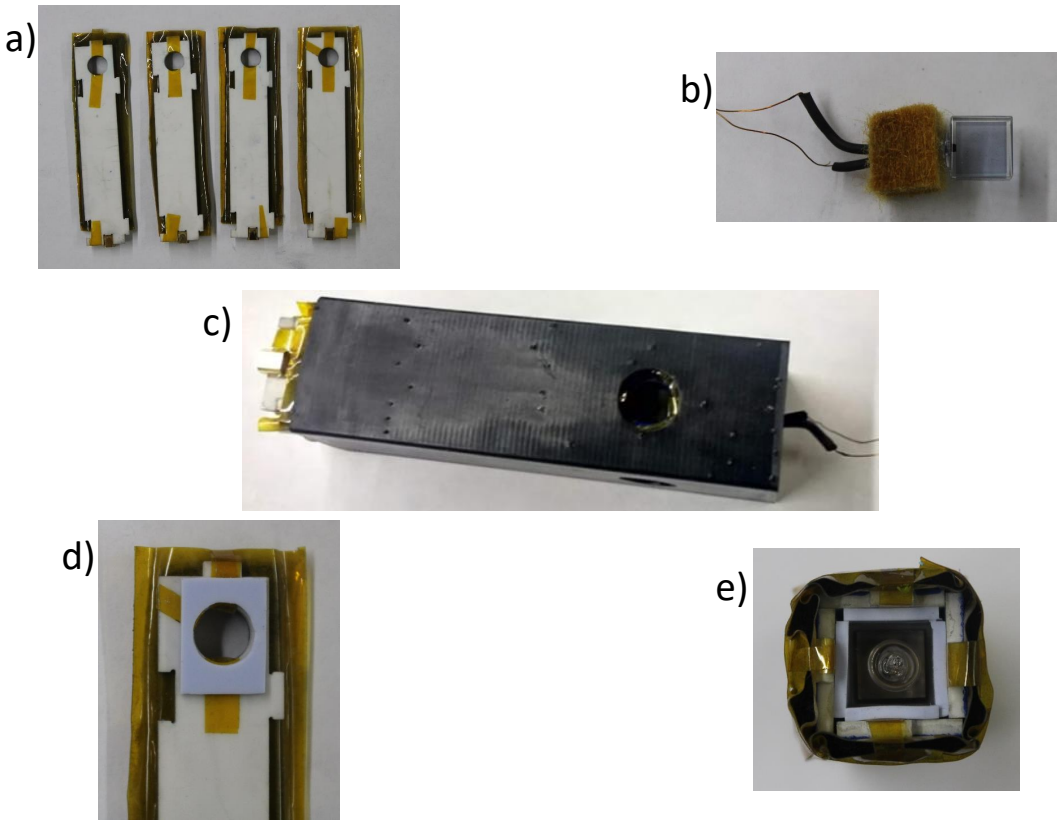

Figure 3.1: Vapor cell heater and cartridge mount photographs. a) four ceramic jig heater sides with aerogel pillows attached to outer faces. AC power enters via MMCX connectors at the bottom of each jig heater. b) 1 cm^3 vapor cell with stem tucked into fiberglass insulation. The RTD sits between the insulation and outer cell wall. c) cartridge with cell installed. d) gap fill shim on one jig heater face. e) view looking into the jig heater with the cell installed. Note the four pieces of gap fill between each outer cell wall and the jig heater inner faces.

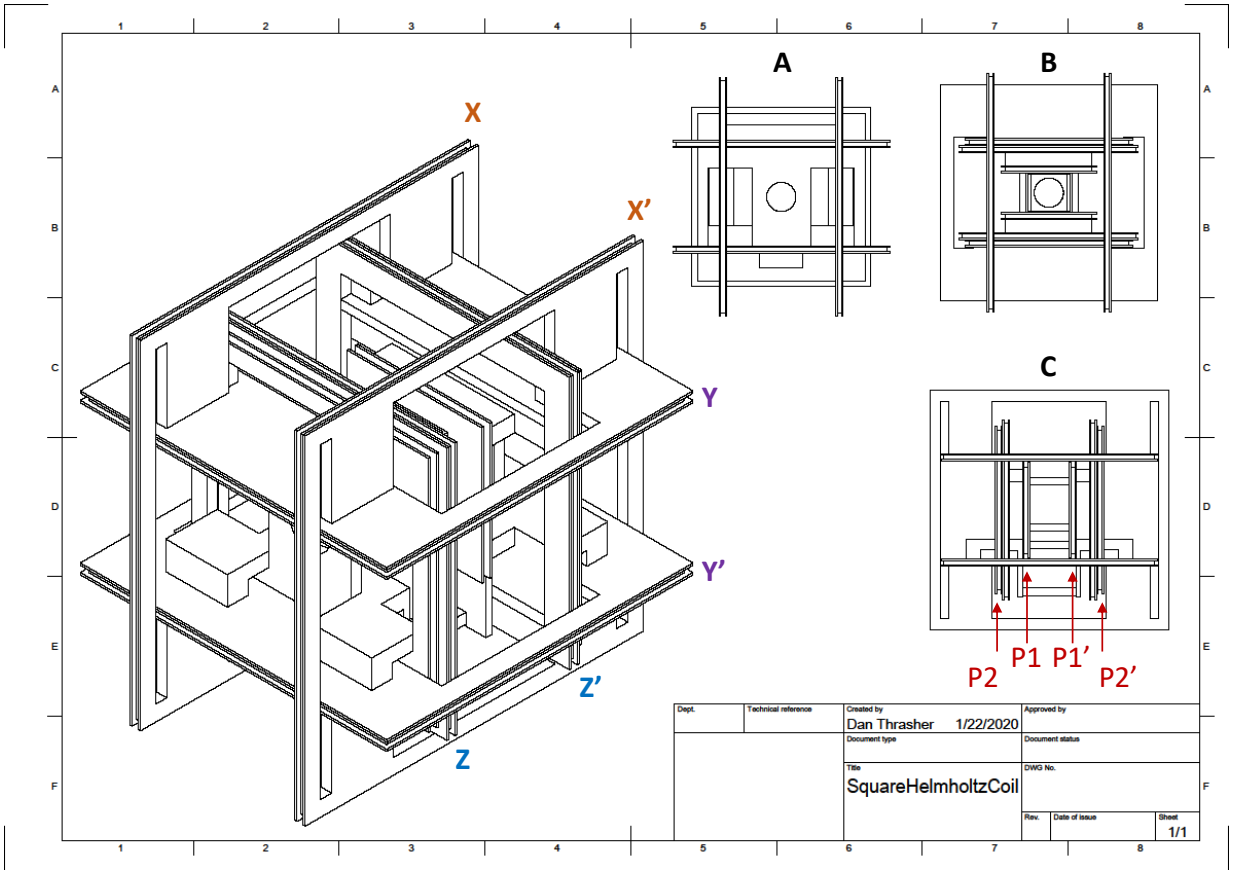

Figure 3.2: Sketches of the rig containing the shim and pulsing coil sets. The cell cartridge sits in the middle. A: view along the $\hat{z}$-axis. B: view down the $\hat{y}$-axis. C: view through $\hat{x}$-axis.

Magnetic Fields

The three layer μ-magnetic shield we use (see Fig. 3.3) was originally designed for performing gradiometry. It is cylindrical with eight access ports (two along the axis of symmetry and six oriented tangentially). Since the pump laser light must enter through the ports we must place our cell such that it is not equidistant from the endcaps. The asymmetry in distance to endcaps informs the design of our bias pulsing coil set. In order to minimize coupling to the shield end caps and maximize uniformity across the volume of the cell, the pulsing coil set consists of two pairs of square coils with differing side lengths wound in series with opposite

Figure 3.3: Model of magnetic shields. The end caps are not shown.

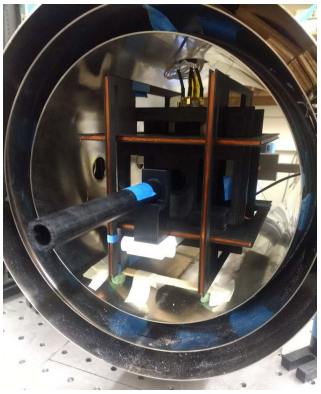

Figure 3.4: Picture of coil rig with cell installed in magnetic shield without the end caps in place. The probe travels through the black pipe oriented towards the viewer.

polarity. The purpose of the ancillary counter wound coils is to suppress the field produced by the coil set at the nearest end cap. See [Korver (2015)] for specific design details. Figure 3.4 depicts the coil rig mounted in the magnetic shields without the end caps installed.

The bias field requires short pulses (< 5 μsec) of ≈ 1 Ampere peak current. The circuit used to drive the pulsing coil was custom-made and is described in [Korver (2015)]. The circuit used to drive the shim coils was also custom-made and is described in [Wyllie (2012)].

Optics

To perform optical pumping of the Rb, the outputs of two distributed feedback laser diodes tuned near the Rb D1 transition (one on either side of resonance) are overlapped (see Fig. 3.5). This is accomplished by polarizing pump A so that it is mostly transmitted by a polarizing beam splitter (PBS) and pump B so that it is mostly reflected by the same PBS. The combined beam is then sent through a quarter wave plate and then separated into two beams using a PBS once again. The angle of the quarter wave plate is chosen such that both pump A and pump B have half their power in each output beam. The resulting beams are

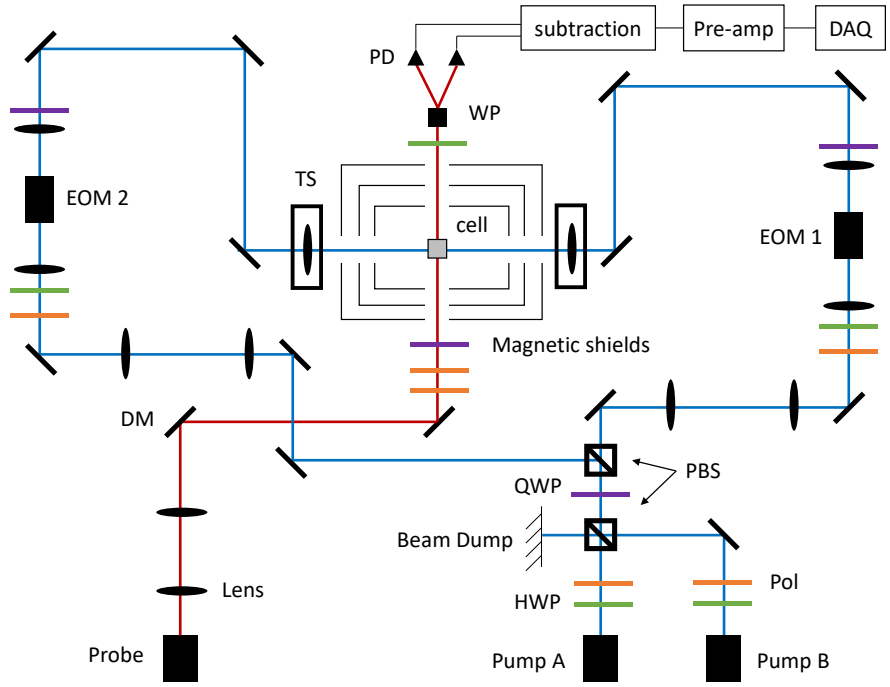

Figure 3.5: Experimental setup for PM excitation. DM: dichroic mirror, Pol: polarizer, HWP: half wave plate, QWP: quarter wave plate, PBS: polarizing beam splitter, WP: Wallaston prism, PD: photodiode, EOM: electro-optic modulator, TS: two axis translation stage. The three axis magnetic shim and pulsing coils are not shown. The setup fits on a four foot square optical table.

then individually expanded (so that twice their beam waist is equal to the aperture of the ceramic heater) and coupled into individual EOMs using a one-to-one telescope. Prior to each EOM is a polarizer and half wave plate. The polarizer ensures that the light incident to the EOM crystal is purely linear. The half wave plate is used to align the light polarization relative to the EOM crystal axis. The maximum and minimum voltage of the EOM drive waveform is chosen to produce $\pm\lambda/2$ retardance. The quarter wave plate at the output of the EOM converts the EOM output at $V_{max}(V_{min})$ to be $\sigma^+(\sigma^-)$. The collimated output of each EOM is coupled into the vapor cell from opposing directions. Fine tuning of each pump beam's pointing is controlled using long focal length lenses mounted on two axis translation stages just outside the magnetic shield. The position of each steering lens is chosen to optimize the magnetometer gain. The power and detuning of each pump laser is chosen

to cancel the AC Stark effect. Optical pumping from both directions is desirable because doing so increases uniformity of Rb polarization across the optically thick cell. See [Kornack (2005)] for a detailed treatment of how optical thickness influences the optical pumping of alkali-metal atoms as a function of cell depth for single sided pumping.

To detect S_z, approximately one mW of linearly polarized light from the output of a third distributed feedback laser diode, tuned near the Rb D2 line, is directed through the center of the cell and parallel to $\hat{z}$. Over filling the cell (like the pump lasers) is undesirable because probe light which does not interact with the atoms is wasted. Under filling the cell too much is undesirable because then only a small portion of the Rb atoms are being probed by the laser light. This can be especially detrimental if the optical thickness is high and (despite dual sided pumping) there exist transverse Rb polarization gradients. Under such conditions and with a small probe beam waist the Faraday signal could be highly sensitive to probe beam pointing. For these reasons we set the probe beam waist to be roughly 1/4 the cell width. We find that a pair of crossed polarizers enables control of both the probe power and polarization orientation incident to the vapor cell. A quarter wave plate just before the magnetic shield allows for fine tuning of the probe beam's circular polarization. This is necessary because the vapor cell introduces some quarter wave retardance to the probe laser before interacting with the Rb atoms. Since optical pumping the Rb vapor along $\hat{z}$ is undesirable we compensate for the circular polarization introduced by the hot cell using the quarter wave plate. The polarization of the transmitted probe light is analyzed via a balanced polarimeter consisting of a half wave plate and Wollaston prism. We are careful to have minimal optics between the back of the vapor cell and the detection photo diodes as any loss of photons leads to reduced detection sensitivity. We find the Wollaston prism advantageous compared to polarizing beam splitter cubes because of their excellent extinction ratio, temperature stability, and minimal optical interference. The half wave plate is used to "balance" the polarimeter such that the difference current of the detected photo diodes is small. We use large area photo diodes to prevent probe laser light from missing the

photo diodes. Although one could focus the probe light onto the PD one must be careful to not saturate the power per unit area of the PD. Additionally, we find that the polarimeter is sensitive to fluctuations in beam pointing. Focusing more tightly increases this sensitivity. We attribute this to lack of uniformity in response across the photo diode active area.

We originally used liquid crystal variable retarders (LCVR) to modulated the pump photon polarization. We chose these because of their large acceptance aperture compared to elecro-optic modulators (EOM). The LCVR accept collimated beams with a 10 mm beam waist. The EOMs however require careful coupling into the few cm long crystal with apertures of only a few mm. Despite the convenience of coupling into the LCVRs we eventually found that the fidelity of modulation they produce is far inferior to EOMs. We proved this by modulating the pump polarization with either EOMs or LCVRs and measuring the noise on S_z at the PM frequency as a function of DC B_y. Recall from Ch. 2 that S_z can be written as

$$S_z \sim \frac{\Omega_y R_x}{\Gamma'^2} \mathrm{scos}(\omega t + \phi), \tag{3.2}$$

where we have assumed $B_y >> B_z, B_x$, $\Omega_y = \gamma^S B_y << \Gamma'$, and scos() = sign(cos()) which comes from the PM. If we demodulate S_z with $\sin(\omega t)$ we find

$$V_Q = \langle S_z \sin(\omega t) \rangle \sim -\frac{\Omega_y R_x}{\Gamma'^2} \sin(\phi) + \delta V_Q, \tag{3.3}$$

$$V_I = \langle S_z \cos(\omega t) \rangle \sim -\frac{\Omega_y R_x}{\Gamma'^2} \cos(\phi) + \delta V_I, \tag{3.4}$$

where V_Q and V_I are the quadrature and in-phase components respectively, and the δVs represent measurement noise inherent to each component. The ratio V_I/V_Q is equal to $\cot(\phi) \equiv DNR$ in the large Ω_y limit.

Figure 3.6 shows V_I/V_Q (i.e. SNR) vs DC B_y using either the EOMs or LCVRs. For large B_y, V_I/V_Q saturates at more than 10^4 $\sqrt{\mathrm{Hz}}$ when the EOM is used to modulate the

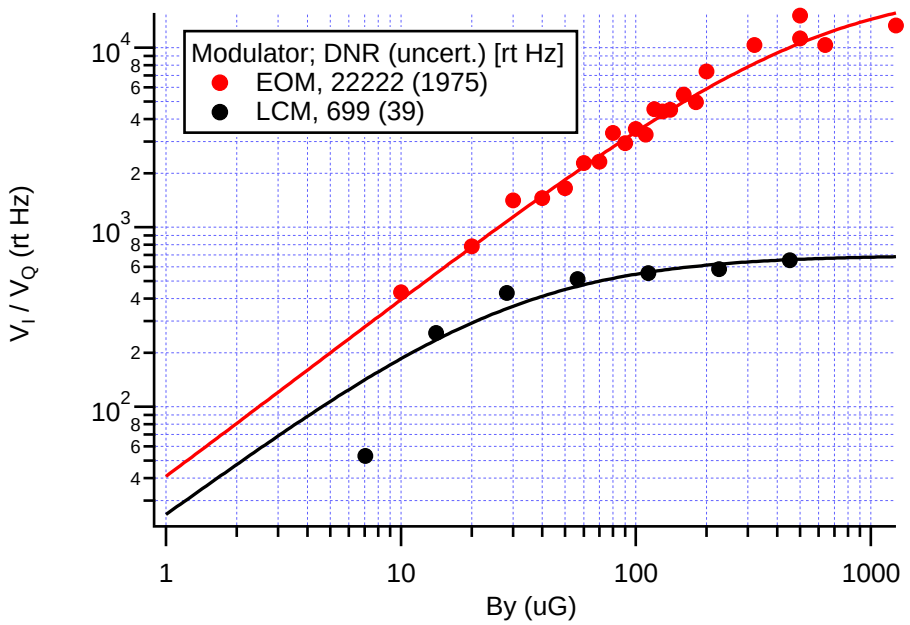

Figure 3.6: Comparison of measured LCVR and EOM DNRs. Filled circles are measured data. Lines are fits to the data using the ratio of Eqs. 3.3 and 3.4. The DNR and its uncertainty from the fit for each modulator are listed in the legend.

light polarization. When the LCVR is used to modulate the light polarization, the V_I/V_Q saturates at less than 10^3 $\sqrt{\text{Hz}}$.

We also found that the LCVR required daily optimization of the voltage set points where as the EOMs did not. The added one time inconvenience of coupling light into the EOMs was more than offset by their performance improvement. All the data presented in this thesis was taken with EOMs. Recall from Ch. 2 that our target photon shot noise limited SNR is 1 ppm which is 100x superior to the DNR measured using the EOMs. Hence, for the case of PM excitation we do not expect to be photon shot noise limited because of the limited DNR of the EOMs. One idea we have had to modulate the polarization with better fidelity than the EOMs is to use a fiber coupled micro-electromechanical system (MEMS) switch. Instead of actively modulating the polarization of the pump beam along a fixed beam path, this scheme would modulate the path the beam travels through fixed waveplates. For σ^+ polarization it would travel one direction and for σ^- it would travel another. The

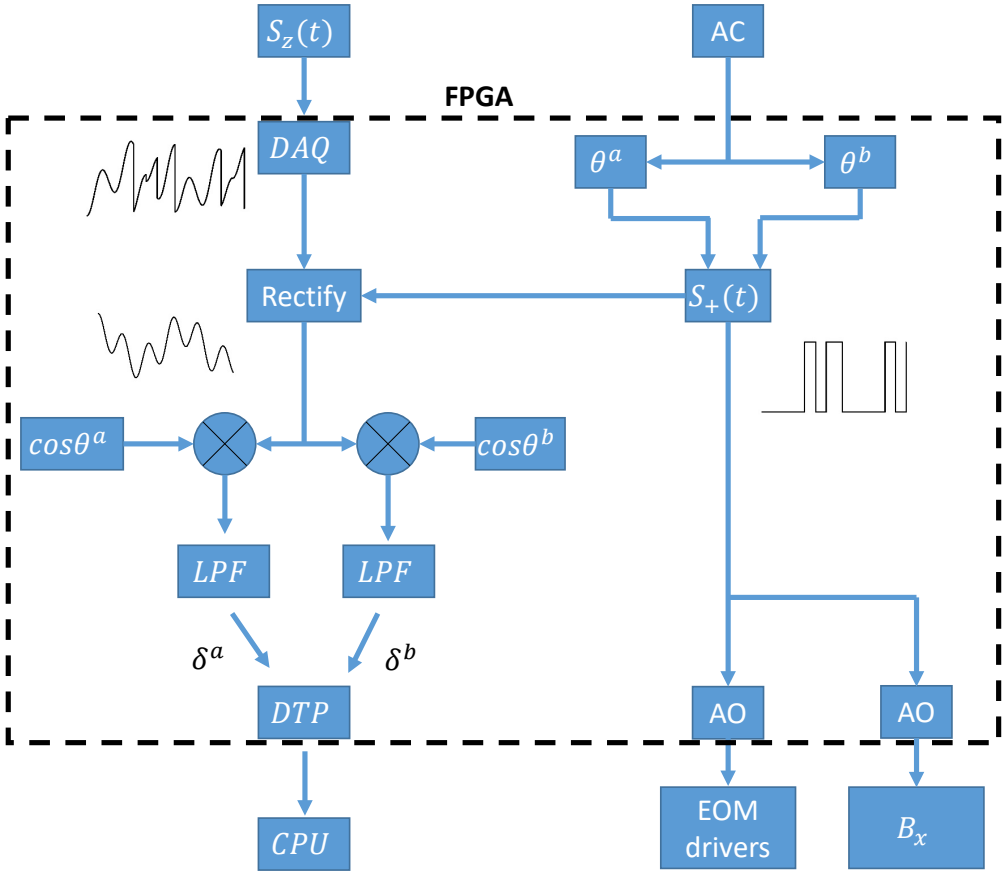

Figure 3.7: Schematic of software operations. Atomic clock (AC), Low-pass filter (LPF), analog output (AO), digital transfer protocall (DTP), central processing unit (CPU), B_x represents the $\hat{x}$-shim driver.

two beam paths are combined on a polarizing beam splitter followed by a 1/4 wave plate. We think that modulating the direction of propagation is easier to do with high fidelity than modulating the polarization itself. We have yet to implement this new scheme but fiber coupled MEMS switches with 1 msec rise times are commercially available for less than the cost of an EOM and its driver. From a practical point of view, MEMS switches are more compact, require less sophisticated electronics, and consume less power.

Software

The software which runs the experiment must complete the following tasks:

1. Synthesize control voltage for the EOM electronics to produce $S_+(t)$.
2. Synthesize the control for $\hat{x}$-magnetic shim driver which compensates (cancels) the transverse Rb SE experienced by the Xe nuclei.
3. Digitize the S_z signal from the photo diode pre-amp.
4. Rectify the digitized S_z signal.
5. Demodulate the rectified S_z signal at ω^a and ω^b.
6. Transfer the phase difference δ to the control computer.
7. Save the transferred δ data to the computer memory for post processing

Nearly all of these tasks are accomplished on a field programmable gate array (FPGA) because of its reliable timing and low latency. The timing of the FPGA is referenced to a commercial atomic clock. In essence, the FPGA enables us to compare the measured phase of precession of each isotope to the phase of the atomic clock. One can transfer the phase stability of a reference oscillator to another much lower frequency through a process known as direct digital synthesis (DDS). App. B provides an overview of DDS and how to implement it in LabVIEW FPGA. We use DDS to compute a drive phase θ for each isotope. The drive phases of each isotope are then combined to construct the signal $S_+(t)$. The details on how to combine θ^a and θ^b to construct $S_+(t)$ depends on the desired excitation waveform (the next section discusses two different excitation waveforms we have implemented). The FPGA we use has an integrated 16-bit DAQ which samples S_z at a constant rate. The digitized data are rectified by multiplying by ± 1 depending on a trigger which has the same phase as $S_+(t)$. These rectified data are then demodulated by multiplying by $\cos(\theta^a + \alpha^a)$ or $\cos(\theta^b + \alpha^b)$

where α is the lock-in phase. The two data streams from the individual multiplications are then individually low-pass filtered and saved for future reference.

We would like to point out that lock-in detection or demodulation is best suited for measuring small signals relative to a noisy background. The signals produced by the comagnetometer are large compared to the background noise. The data that follows utilizes lock-in detection. Given the chance to repeat these measurements however we would replace lock-in detection with a real-time fitting algorithm (See Ch. 4.5).

In order to excite both isotope's a and b simultaneously we need merely modulate the Rb polarization such that it has large Fourier coefficients near each isotope's resonance frequency (see Ch. 2). Additionally, the modulation waveform should have minimal power at frequencies besides each isotope's resonance. Ideally the modulation would avoid producing any linear polarization as such ruins the Rb magnetometer. In the sections that follow we compare the comagnetometer performance for square and sinusoidal modulation.

3.3 Square Modulation

Excitation

We developed two modulation waveforms which produce large Fourier amplitudes at the Xe resonances while avoiding linear polarization. They can be written as,

$$S_+^1(t) = S_0 \,\mathrm{sign}[\cos(\frac{\omega^a + \omega^b}{2}t + 2\cos(\frac{\omega^a - \omega^b}{2}t))], \tag{3.5a}$$

$$S_+^2(t) = S_0 \,\mathrm{sign}[\cos(\frac{\omega^a + \omega^b}{2}t)]\,\mathrm{sign}[\cos(\frac{\omega^a - \omega^b}{2}t)]. \tag{3.5b}$$

Figure 3.8 shows the simulated time dependence and power spectrum of each modulation waveform assuming $\omega^a = 27$ Hz and $\omega^b = 8$ Hz. Both waveforms have maximum Fourier coefficients at ω^a and ω^b, with the amplitudes of S_+^2 slightly larger than S_+^1. Their power

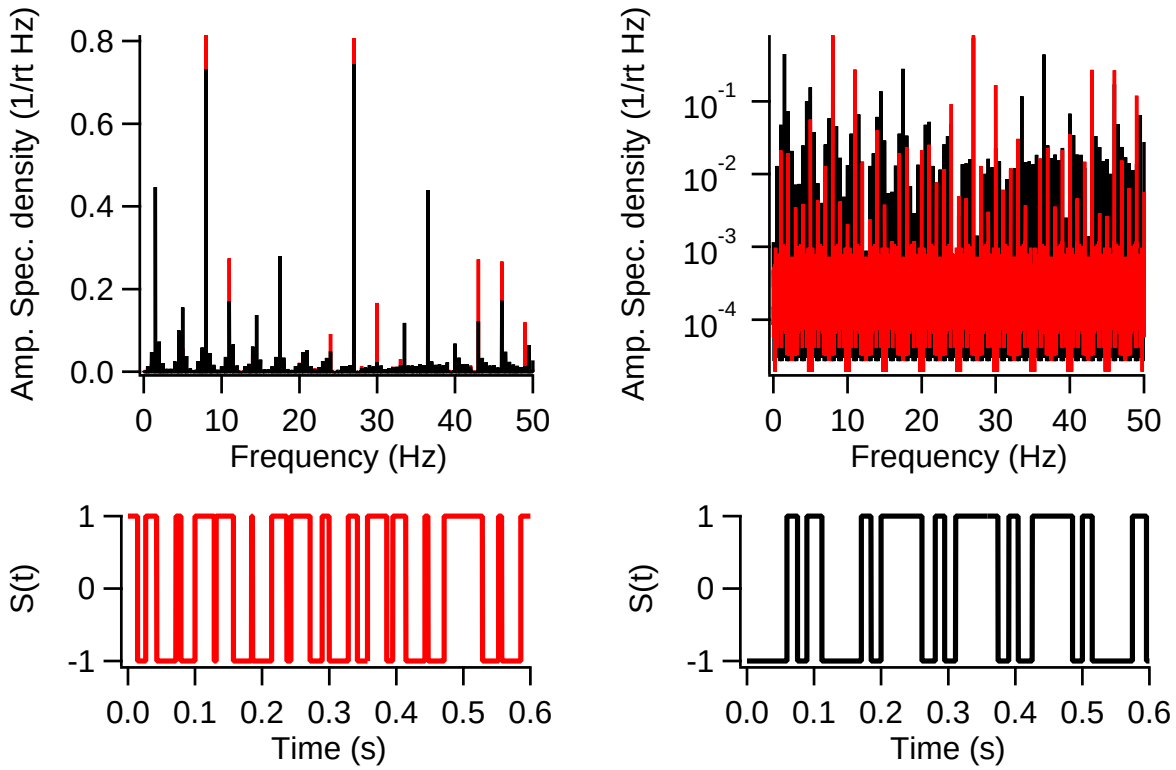

Figure 3.8: Comparison of simulated PM waveforms. Top-left: Linear scale of amplitude spectral density. Top-right: Log vertical scale of amplitude spectral density. Bottom-left: time series of $S_+^2(t)$. Bottom-right: Time series of $S_+^1(t)$.

spectra also contain (many) other peaks at the same frequencies. In general the Fourier amplitudes of these spurious peaks are larger for S_+^1 (see log plot). In particular, S_+^1 has substantial spectral content at a sideband which is less than 1 Hz. The white noise floor for S_+^2 is slightly higher than that of S_+^1. Looking at their respective time series we see that S_+^1 has a minimum separation between transitions whereas S_+^1 does not. In general we have found no difference in performance between these two waveforms. In practice S_+^2 requires less logic to synthesize on the FPGA.

Detection

Figure 3.9 shows the measured (un-rectified) Faraday rotation noise. We see that the probe noise (green) is greater than the electronic noise (blue) for all frequencies. This suggests that

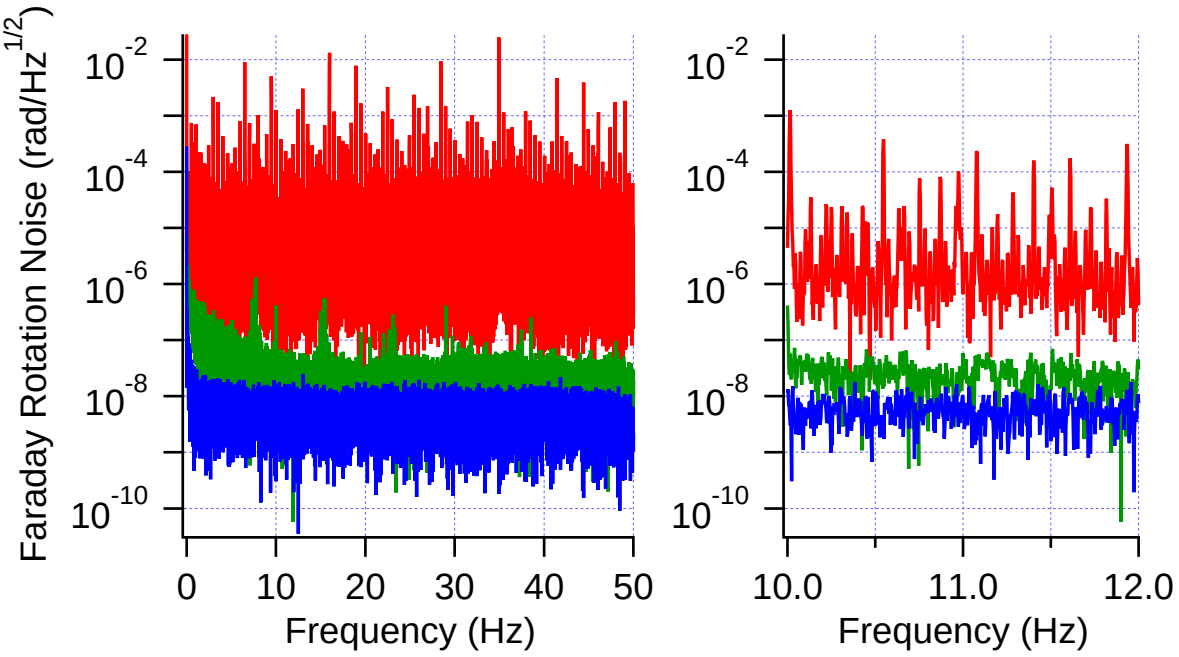

Figure 3.9: Measured Faraday rotation amplitude spectral density. Blue: pump and probe lasers blocked, Green: pump lasers blocked, Red: dual species Xe excitation (all lasers unblocked). Left: full spectrum, Right: zoom in from 10 to 12 Hz. The DC magnetic response for this data was 85 rad/G with a bandwidth of several hundred Hz.

the probe power is sufficiently high (if the electronic noise is equal to the probe noise then you should increase the probe power). For frequencies > 10 Hz the probe noise is dominated by white noise. This white noise level is within a factor of 2 of the computed photon shot noise. For frequencies < 10 Hz the probe noise is dominated by $1/f$ detection noise. We believe this detection noise stems from beam pointing fluctuations due to air turbulence. The structure at multiples of ~ 7 Hz may be due to optical table vibrations (the table the experiment is mounted on is not floated). The detected un-rectified Xe (red) exhibits many discrete peaks as well as white noise. This signal is only probe noise limited for frequencies $<<$ 1 Hz. The source of the white noise is not well understood. We find that the white noise is greatly improved when $S_+(t) \sim \text{scos}(\omega t)$ instead of $S_+^{1,2}$ (see Fig. 3.10). We originally attributed this reduction in noise to pump pointing which was altered between the green and red trace. The S_z white noise has also exhibited linear dependence on the number of 2π

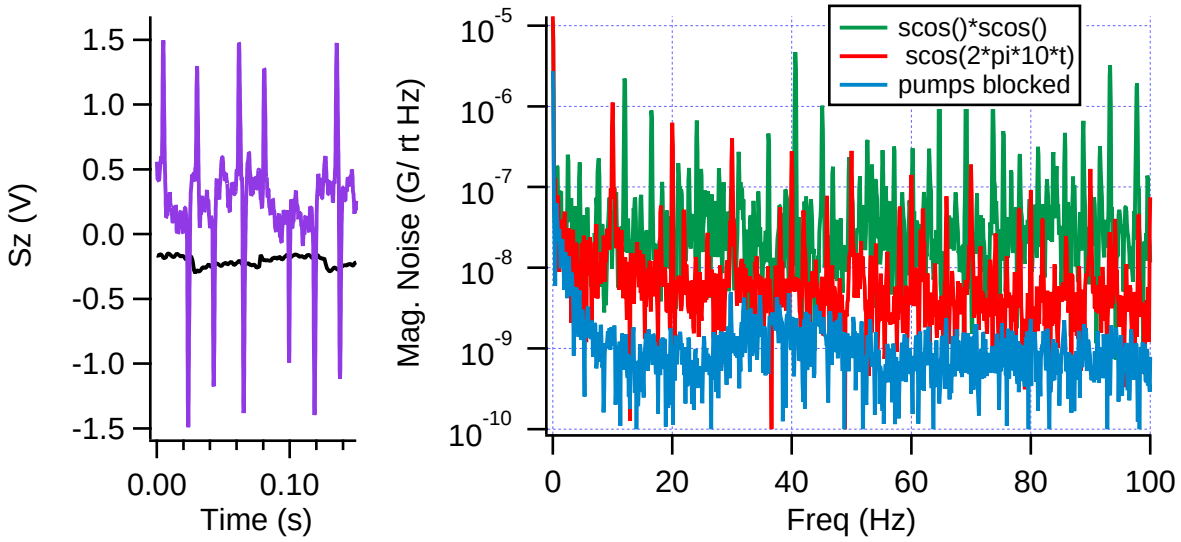

Figure 3.10: Left: influence of pump laser pointing on optical pumping transients. Purple: non-orthogonal pump pointing corrected with B_y. Black: orthogonal pump pointing. Note: the purple data was acquired with dual frequency square modulation whereas the black data was acquired with a single frequency square modulation. Right: Influence of dual vs single frequency modulation on measured S_z noise. The dual frequency modulation produces 5x the white noise on S_z as single frequency modulation.

precessions each bias pulse causes the Rb to precess by (see Fig. 4.10). The mechanism for this remains unknown.

Another subtlety regarding detection is the pointing of the pump laser. Recall from the static solution to the Bloch equation that $S_z \sim R_z$. The direction of $\hat{z}$ in the lab frame is dictated by the propagation direction of the probe laser. If the pump has a non-zero projection along $\hat{z}$ then $R_z \neq 0$. Since we modulated the pump polarization, R_z produces an AC S_z just like a DC B_y. One could inadvertently compensate for a pump beam which is not orthogonal to the probe beam by applying a B_y. Since R_z can be a source of noise and we desire to operate at zero field, proper pump pointing is important. We found that the optical pumping transients are an excellent indicator of the orthogonality between the pump and probe. When the optical pumping transients are minimized, the pump is orthogonal to the probe. Figure 3.10 shows how the time series of S_z is altered by optimizing the pump

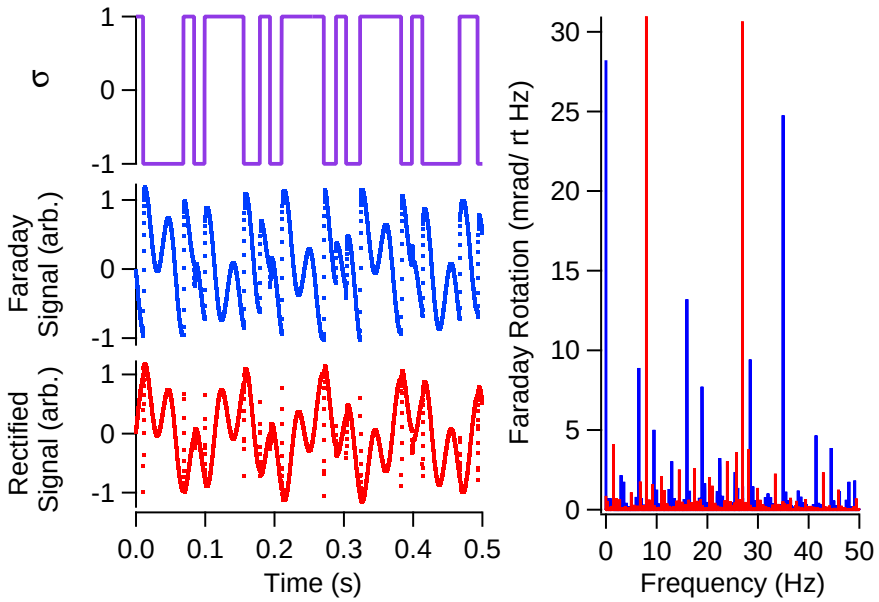

Figure 3.11: Measured square wave PM signals. Top: $S_+^1(t)$. Middle: $S_z(t)$. Bottom: Rectified $S_z(t)$. The plot on the right shows the amplitude spectral density with (red) and without (blue) rectification.

pointing and B_y to minimize optical pumping transients. Please note that for the purple trace $S_+(t) = S_+^1$ while for the purple trace $S_+(t) \sim \text{scos}(\omega t)$.

Figure 3.11 shows the time series of the measured S_z with and without rectification when we drive both isotopes near resonance simultaneously using S_+^1. We see that rectification reveals the sinusoidal precession of each isotope. The outlying data on the rectified signal, which occur when the polarization is reversed, are due to the optical pumping transients of the Rb magnetometer. Although rectification collects the many Xe signal sidebands into the two Xe carrier frequencies (see power spectrum on right), it also maps $1/f$ detection noise S_{z0} to the carrier frequencies as well. The mapping of S_{z0} noise to the carrier frequencies can be prevented by high pass filtering (HPF) S_z with a 1 Hz corner prior to rectification.

Figure 3.12 shows the NMR for each isotope. These data were acquired by driving one isotope on resonance while varying the other isotope's drive frequency and recording its K_x and K_y derived using demodulation. We see that the lineshapes are nearly Lorentzian with

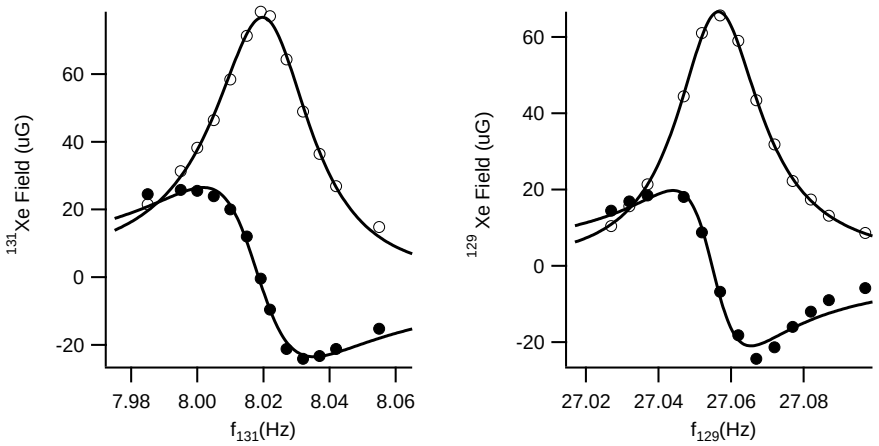

Figure 3.12: Measured NMR of each species. Filled circles are K_y, open circles are K_x, and lines are Lorentzian fits.

linewidths (half-width at half-max) of $\sim$ 15 mHz and amplitudes of approximately 60 μG. The on resonance amplitudes are in agreement with estimates (see App. A). The implied T_2s from the fits are in good agreement with independent measurements of each isotope's T_1. The 15 mHz linewidths are only possible because of two elements; (i) the use of a Rb hydrid cell coating (without which T_2^b would be substantially shorter and T_2^a much longer), and (ii) the application of a magnetic compensation field B_x that cancels the Rb SE field experienced by the Xe. Figure 3.13 shows how the measured line width of each isotope depends on the respective amplitude of compensation field $B_x(t) = B^a \sin(\omega^a t) + B^b \sin(\omega_b t)$. The size of the compensation field required to narrow both isotopes linewidths is in good agreement with the estimated Rb SE field. As long as the phase of the compensation field is carefully chosen, the on resonance amplitude is normally within a few percent of the uncompensated on resonance amplitude.

Figure 3.14 demonstrates the amplitude spectral density of the phase noise measured for each isotope under simultaneous resonant excitation conditions. We see that for frequencies less than 1 Hz the spectra are dominated by $1/f$ noise which is $\sim \rho$ greater for isotope a (black traces) than for isotope b (red traces) suggesting their source is magnetic in

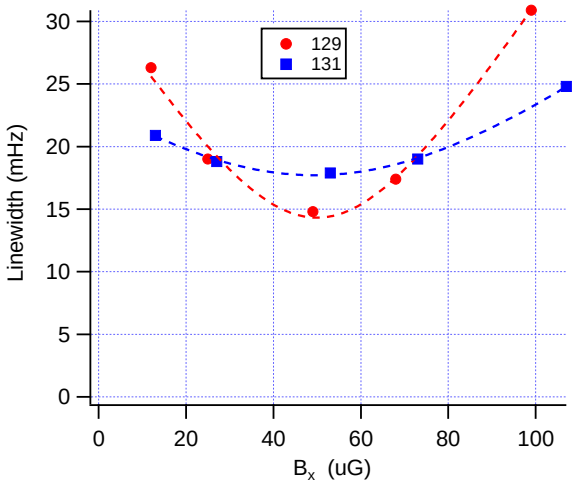

Figure 3.13: Dual species narrowing of NMR linewidth by cancellation of Rb SE field with AC B_x.

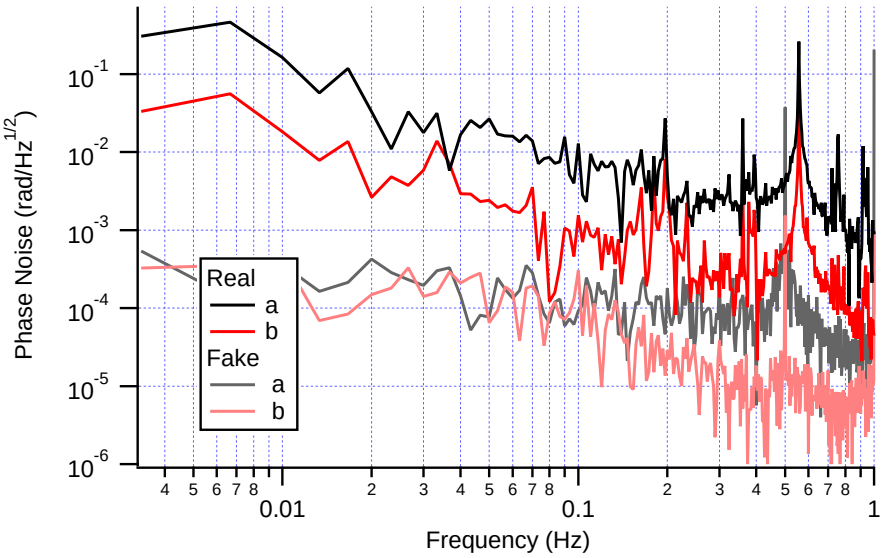

Figure 3.14: Measured phase noise of each species. Traces labeled "Real" are recorded when the Xe are excited on resonance. Traces labeled "Fake" are recorded when the Xe isotope's are both driven off resonance (not excited) and an AC B_y is applied to the magnetometer at the off resonance drive frequencies.

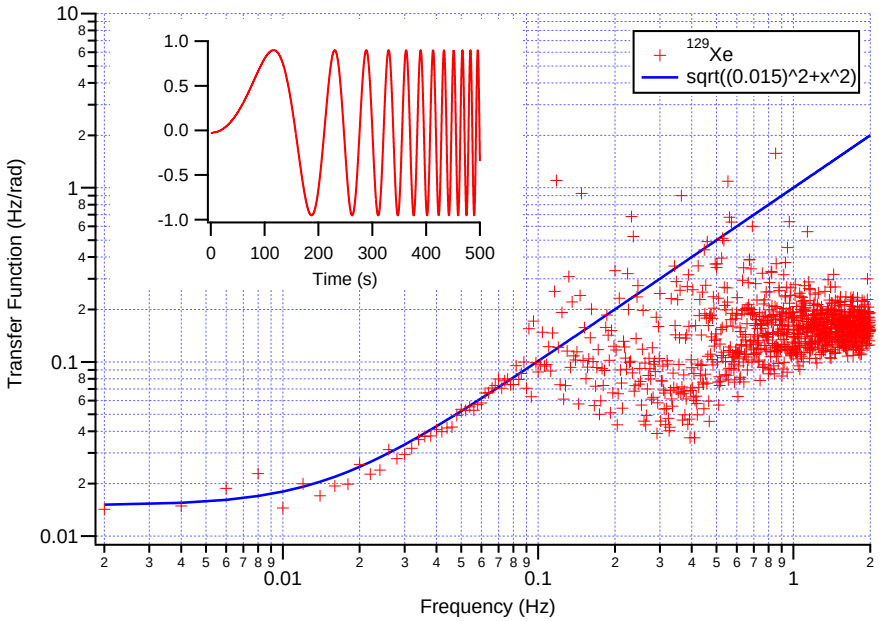

Figure 3.15: Transfer function of ^{129}Xe.

nature. Also shown is the phase noise measured when the Xe isotopes are off resonance (not excited) and a so called "fake" Xe signal is applied along B_y. The amplitudes of this signal $A^a \sin(\omega^a t) + A^b \sin(\omega^b t)$ are chosen to produce the same size magnetometer signal as real Xe. We note that this fake Xe signal is planar unlike the real Xe signal which rotates. The fake signal allows us to measure the SNR of the Rb magnetometer. These signals do not show $1/f$ dependence because, unlike the real Xe phase, the SNR of the magnetometer does not depend on the bias magnetic field to first order. The phase noise of each fake Xe measurement is uncorrelated and limits the possible field suppression when constructing $\tilde{R}$. The SNR for each isotope is $\sim 5000\sqrt{\text{Hz}}$. This limit is too small to be from finite DNR from the EOMs (see Fig. 3.6) but is likely due to the unexplained white noise present on S_z (see Fig. 3.9).

Comagnetometry

We perform comagnetometry by subtracting magnetic field correlations between the two isotope's frequencies of precession. Since our device measures phase, we need to know or measure the transfer function from phase to frequency. In Ch. 2 we calculated the transfer function to be (see Eq. 2.12)

$$\tilde{\delta} = -\frac{\tilde{\Delta} \pm \Gamma_2 \tilde{\epsilon}_z}{\Gamma_2 + i\omega}, \tag{3.6}$$

where $\Gamma_2 = 1/2\pi T_2$. We measured the transfer function of each isotope by recording the response of the measured phase δ to sinusoidal modulation of B_z. Figure 3.15 shows the measured transfer function for isotope a. We use a chirp waveform to modulate the bias field $B_z^{mod}(t) = B_0 \sin(2\pi[e^{t/T_2} - 1 - t/T_2])$, the time series of which is shown in the inset of Fig. 3.15. This modulation waveform allows us to measure the transfer function from 0.02 to 0.1 Hz with good SNR in a single data acquisition. The transfer function is the ratio $\gamma^K \tilde{B}_z^{mod}/\tilde{\delta}$. We fit the data according to Eq. 2.12 and find excellent agreement with the linewidth derived from the NMR.

Although conversion from phase to frequency for the measured Xe phases is possible using a measured transfer function, feedback is desirable because (in the high gain limit) the conversion from phase to frequency becomes insensitive to changes in the transfer function. For the PM comagnetometer we used the measured precession phase of isotope a to stabilize the bias field and the measured transfer function of isotope b to convert its measured phase noise to frequency noise. Under such conditions the frequency noise of isotope b is proportional to rotation. We write

$$\tilde{B}_z = \tilde{G}(\tilde{\delta}^a - \tilde{\epsilon}_z) \rightarrow \frac{1}{\gamma^a}[\tilde{\omega}^R + i\omega\tilde{\epsilon}_z], \tag{3.7}$$

where the arrow implies the high gain limit $\tilde{G} \rightarrow \infty$. The measured phase of isotope b

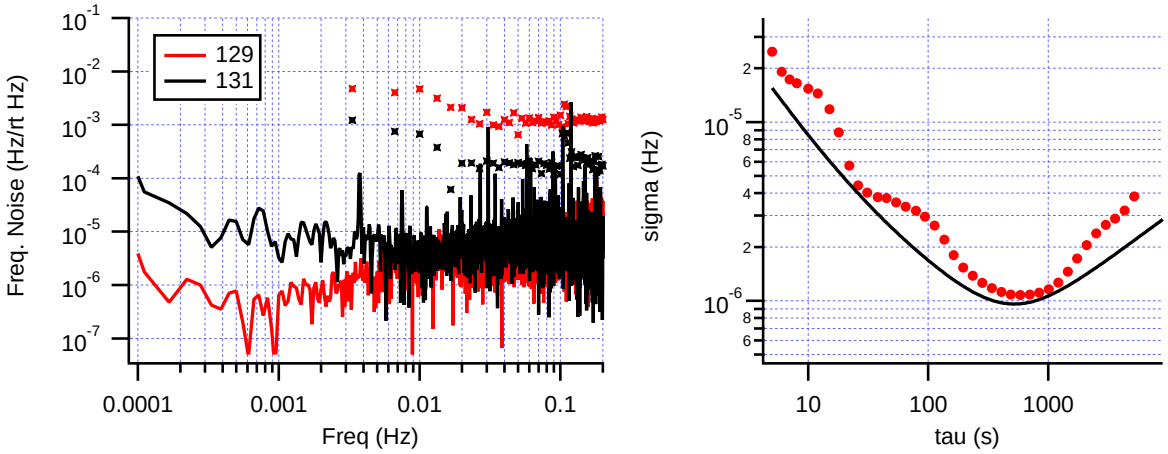

Figure 3.16: Measured Comagnetometry noise and stability. Left: the amplitude spectral density of frequency noise. The cross marks indicate open loop frequency noise. The solid lines are frequency noise when measured phase noise of isotope b is used to stabilize bias field. Right: modified Allan deviation of ω^b. Filled circles are measured data. Solid line shows the quadrature sum of $7 \times 10^{-5}\tau^{-1}$, $1.5 \times 10^{-5}\text{Hz}/\sqrt{\text{Hz}}\tau^{-1/2}$, $3 \times 10^{-7}\text{Hz}\sqrt{\text{Hz}}\tau^{1/2}$.

converted to frequency is

$$\tilde{\omega}^b = (\tilde{\delta}^b + \tilde{\epsilon}_z)(\Gamma_2^b + i\omega) = (\rho^{-1} + 1)(\omega^R + i\omega\epsilon_z) \tag{3.8}$$

We see that in the high gain limit, when correcting the bias field to keep the measured phase of isotope a equal to zero, the rotation is simply $\tilde{\omega}^R = \rho\,\tilde{\omega}^b/(1+\rho)$ assuming $\tilde{\epsilon}_z$ is negligible.

The best performance we observed with bias field feedback activated is shown in Fig. 3.16. The feedback consisted of two analog inverted zero gain stages. The influence of bias field feedback is dramatic from 0.1 to 200 mHz. The servo suppresses $\tilde{\omega}^a$ to below 1 $\mu\text{Hz}/\sqrt{\text{Hz}}$ at long times which is nearly 10^4x less than the open loop noise. Because magnetic noise dominates each isotope's precession, servoing the measured phase of isotope a also greatly suppresses $\tilde{\omega}^b$. We observe at least 100x improvement in $\tilde{\omega}^b$ due to feedback. The modified Allan deviation suggests a rotation ARW sensitivity of $\sqrt{2}\ 15\mu\text{Hz}/\sqrt{\text{Hz}}\frac{\rho}{1+\rho} \sim 16\ \mu\text{Hz}/\sqrt{\text{Hz}}$ and a bias instability of 1 μHz $\frac{\rho}{1+\rho} \sim 800$ nHz. The size of ARW is within a factor of 3 of the ratio of the measured linewidths divided by the SNRs (shown in Fig. 3.14). The peaks in the

Allan deviation at 15 and 100 s of integration are due to low frequency narrow band large amplitude noise peaks in $\tilde{\omega}^b$ which we attribute to the PM waveform. The bias instability is limited by $\tau^{1/2}$ trending noise of unknown origin. We find that feedback causes the measured phase of isotope b to trend linearly in time. The source of this frequency bias is uncertain. Although the trend is very stable over the course of a data run, the trend is not consistent between data runs. The bias instability demonstrated in Fig. 3.16 was difficult to reproduce. Typically the bias instability we measured was several μHz.

Cross Talk

Once we had measured the stability of the PM comagnetometer we desired to know if the detection channel designed for measuring isotope a's phase wasn't really measuring a linear combination of isotope a and b's phases. If such cross talk were present then the scale factor (or how we convert the measured precession frequencies to rotation) would change. Suppose there exists cross talk in both channels such that $\omega^a = \gamma^a B_z + \beta\omega^b - R$ and $\omega^b = \gamma^b B_z + \beta'\omega^a + R$ where β and β' represent the cross talk between detection channels. Solving for R we find

$$R = \frac{\omega^b(\rho + \beta') - \omega^a(\rho\beta + 1)}{1 + \rho}, \tag{3.9}$$

where if $\beta = \beta' = 0$ we return to the expression for rotation derived previously. Non-zero cross talk is undesirable because the accuracy with which it is known (or measured) limits the accuracy of conversion from measured precession frequencies to rotation (or any other non-magnetic spin-dependent interactions). A measurement of cross talk is vital since an important alleged feature of our comagnetometer is having a scale factor which is determined solely by ρ.

We measure cross talk between detection channels by starting with both isotopes excited on resonance. The phases of each demodulation detection channel are carefully chosen such

Scheme	fake a	fake b
	Ch. A, Ch. B	Ch. A, Ch. B
Ideal	1, 0	0, 1
Rect.	1, 0.03	0.04, 1
Rect., HPF	1, 0.2	0.07, 1

Table 3.2: Cross talk measurements. The HPF increases the cross talk.

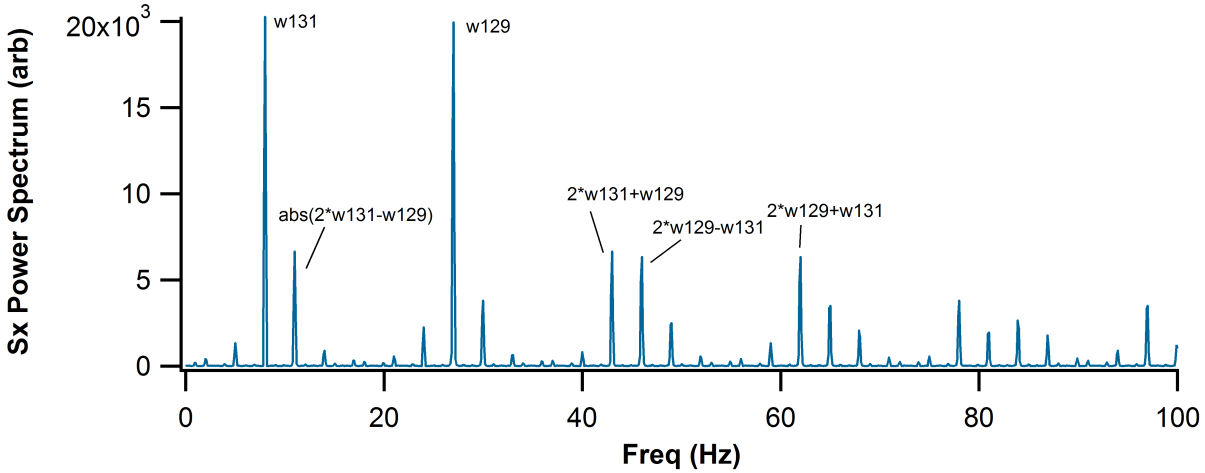

Figure 3.17: Simulated Amplitude spectral density of S_+^1 modulation with sidebands labeled in terms of ω^a and ω^b.

that NMR scans produce purely dispersive lineshapes in the detected quadrature of each channel. Without activating feedback, the average bias pulse repetition rate is then changed so that neither isotope is excited on resonance. A fake Xe signal is applied to mimic the signal produced by an individual isotope. The magnitude detected by each channel is then recorded. If there were no cross talk then the application of a fake isotope a signal should only produce signal on channel A and vice verse. Table 3.2 lists the measured cross talk when fake Xe signals are applied. We find that the cross talk is a few percent when the HPF is omitted. We attribute this to the finite response of the magnetometer which is not accounted for in the rectification. The addition of the HPF increases the cross talk. We attribute this to phase shifts introduced by the HPF which are not accounted for in the rectification.

The source of cross talk can be attributed to the higher order harmonics of the PM waveform. Recall that $S_z \propto S_x K_\perp$. Figure 3.17 shows a simulated amplitude spectral density of S_+^1 where its higher order peaks are labeled. For the case of $2f$ detection without rectification,

$$S_z^{2a} \propto S_x^a K_\perp^a + S_x^{2a+b} K_\perp^b + ..., \tag{3.10}$$

where we use the short-hand $a = \omega^a$. We see that the non-zero Fourier amplitude of S_x at $2\omega^a + \omega^b$ mixes the phase information of $K_\perp^b$ into $K_\perp^a$'s detection channel. Rectification of S_z should prevent cross talk. However, we find that the rectification we employ is insufficient to suppress the cross talk completely. This is likely due to the finite response time of the magnetometer and the phase shifts introduced by the HPF which our demonstrated rectification does not account for.

We further characterized the cross talk introduced by square PM by detuning one isotope's drive frequency by ~ 300 mHz and then scanning the average pulsing frequency. The 300 mHz detuning ensures that both isotopes are not simultaneously on resonance for a given bias pulse repetition rate. The magnitude of each isotope's detection channels' are normalized and plotted vs their respective equivalent drive frequency $\omega^K = \omega_{2\pi}\gamma^K/\gamma^S$. Cross talk is manifest as deviations of the measured magnitude from a Lorentzian line shape. Discrepancies due to cross talk are most pronounced when one isotope is very near resonance and the other is not. Figure 3.18 shows measurements of cross talk for $2f$ (without rectification) and $1f$ (with rectification) detection schemes. The $2f$ scheme exhibits the most severe cross talk. When isotope a is excited and isotope b is not, isotope b's detection channel exhibits non-zero signal and vice verse. We attribute this to the lack of rectification which provides first order correction for the mixing caused by the high order sidebands. A phase sensitive measurement with $1f$ detection reveals cross talk despite the rectification. The signal leaked into the other isotope's detection channel is curiously dispersive in nature. We estimate

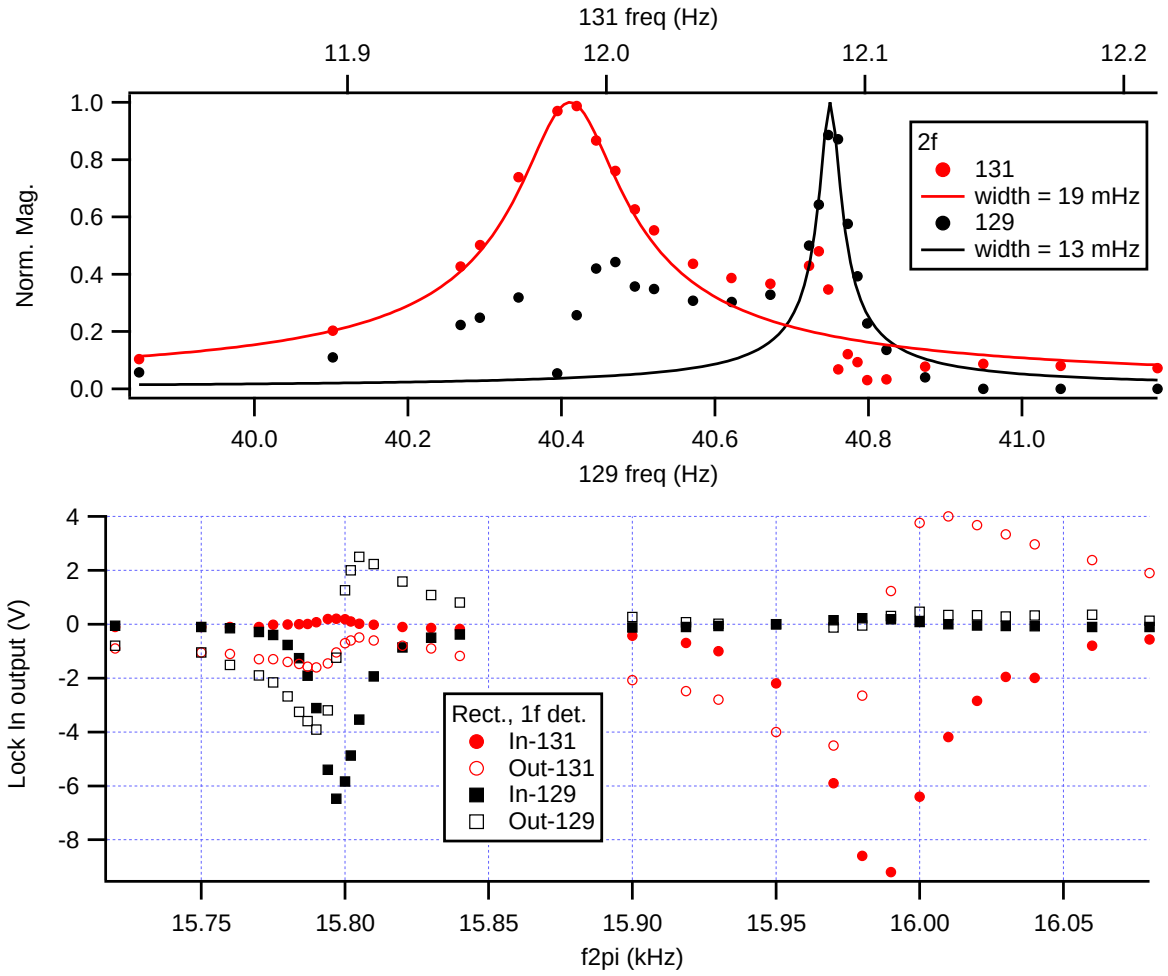

Figure 3.18: Measurement of cross talk. Top: $2f$ (without rectification). Bottom: $1f$ (with rectification). Both measurements are DC coupled. The bottom plot shows the in-phase and out-of-phase components of each detection channel whereas the top plot merely depicts the magnitude of each channel.

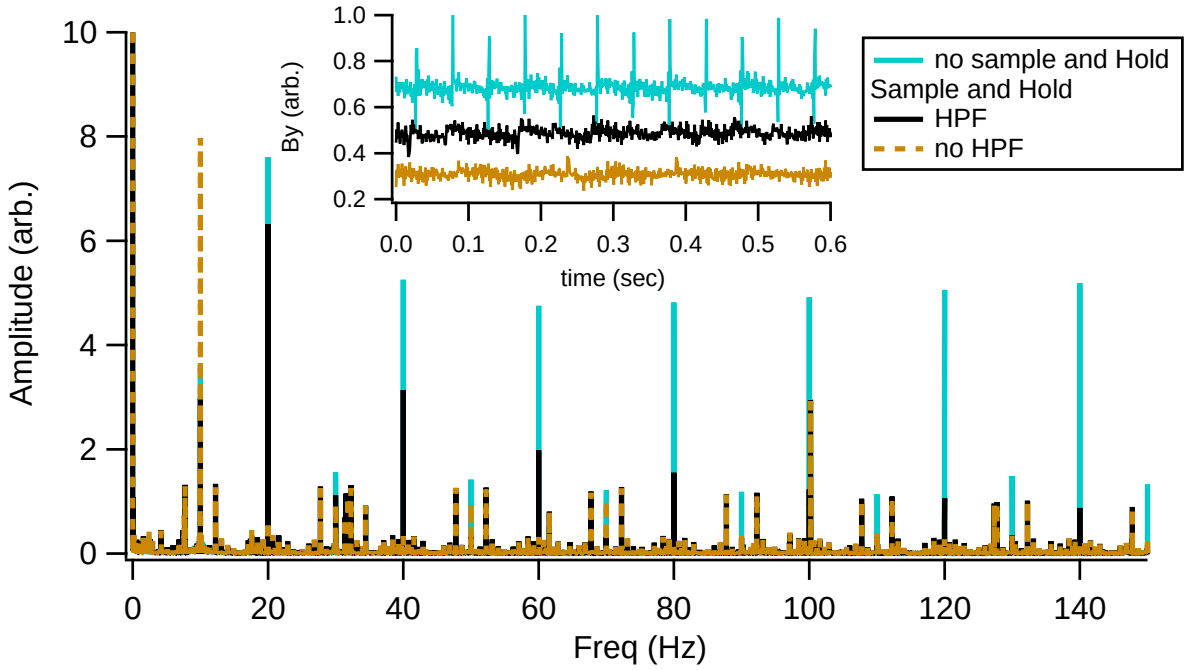

Figure 3.19: Influence of sample and hold during optical pumping transients and HPF-ing on the rectified S_z. This data was acquired when no Xe excited and single frequency square wave PM. The even harmonics depend on both the sample and hold and the HPF.

$\beta = Q^b_{pp}/Q^a_{pp} = 0.17$ (when isotope a is on resonance) and $\beta' = Q^a_{pp}/Q^b_{pp} = 0.07$ (when isotope b is on resonance), where Q^K_{pp} is the peak-to-peak quadrature signal of isotope K

In order to test how important the finite response time of the magnetometer was in contributing to cross talk we built a sample/hold functionality into the FPGA acquisition software which allowed us to greatly suppress the optical pumping transients. Figure 3.19 shows the influence of the sample and hold on the time series and amplitude spectral density of the rectified S_z. Also shown is the influence of the HPF. This data was acquired by setting $S_+(t) = \text{sign}[\cos(\omega t)]$ where $\omega = 2\pi \times 10$ Hz was not equal to either Xe resonance. The presence of even harmonics after rectification with this drive scheme implies the presence of cross talk after rectifying the dual frequency PM waveform. The power in the even harmonic sidebands is minimized when the sample and hold is engaged and the HPF removed.

Since we demonstrated that the HPF adds considerable cross talk we desired to know how

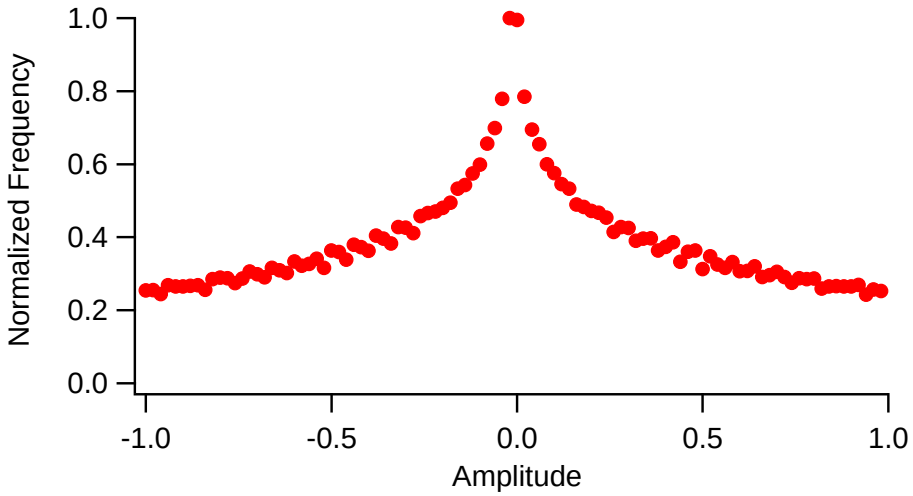

Figure 3.20: Histogram of sum of two sine waves.

much the SNR is degraded if the HPF is removed. We found that the 1 Hz HPF improves the SNR of each isotope by 10x. This is not surprising as the $1/f$ noise of the detection is substantial. We note in passing that we were able to suppress the $1/f$ noise of the Faraday rotation by installing a photo-elastic modulator after the cell which allowed us to AC couple the detection [Seltzer (2008)]. The idea is that probe polarization fluctuations (signal) are scattered to a higher frequency whereas systematic noise sources (such as probe pointing) which appear as $1/f$ polarization noise are not similarly scattered to high frequency. The performance of the PEM was unreliable however so the PEM was removed.

3.4 Sine Modulation

In pursuit of minimizing cross talk without sacrificing SNR we chose to explore sinusoidal PM. Sine wave modulation should not have any higher order sidebands to produce cross talk. Consequently, one could detect at $2f$ without rectification at the cost of some signal. The implementation of sine wave modulation is very similar to square wave modulation. The only difference is $S_+(t) = S_0\ [\sin(\omega^a t) + \sin(\omega^b t)]/2$. Since the retardance of the EOM goes as $\sin(V_{eom})$ the time dependence $V_{eom}(t) = \sin^{-1}(\sin(\omega t))$ produces $S_+(t) = \sin(\omega t)$.

So an arc-sin look up table was programmed into the FPGA. We originally chose to avoid sine wave modulation because the superposition of two sine waves is most frequently near zero (see Fig. 3.20). Hence, the pump light would spend a considerable amount of time linearly polarized which is maximally bad for optically pumping the Rb. However, after associating cross talk with imperfectly rectified higher order modulation sidebands, we decided to attempt sine wave modulation anyways.

Optics: Because the polarization is continuously varied from σ^+ to σ^- the optics which influence the state of polarization (SOP) must be much more carefully considered (and maintained) then for square PM. For instance, the $\sin^{-1}$ transfer function of the EOM is extremely forgiving near $V_{\pm\pi/2}$, the voltage which causes $\pm\pi/2$ retardance, which is where the EOM spends nearly all of the time for square PM. Near zero volts, which is where the EOM spends a disproportionate amount of time for sine PM, the SOP is maximally sensitive to V_{eom}. Additionally, the reflectance of di-electric mirrors (DM) depends on the incident angle and SOP of incident light. For square PM the influence of DM is easily compensated because there are only two SOPs. For sine PM however, the influence of DM mirrors is very difficult to compensate for all SOPs. As a result, the DM can produce amplitude modulation at the PM frequencies. For these reasons we replaced the DM with un-coated gold mirrors.

Another subtlety we discovered was the spatial overlap between pump A and pump B in the EOMs. Since the voltage required to produce a particular retardance depends on the SOP before entering the crystal and the interaction length of the laser light in the EOM crystal we found that proper spatial overlap of the two pump beams was crucial to having any chance of achieving satisfactory sine PM. Perhaps the best way to ensure that the spatial overlap is optimal is to launch both pumps into a single mode fiber before coupling into each EOM. We did not end up implementing such a scheme.

We optimized the SOP by applying a triangle modulation waveform to the EOMs and a DC B_y to the magnetometer. Using a lock-in we detect the power on S_z at the 2nd and 3rd harmonics of the triangle modulation carrier frequency. We found that the 2nd harmonic is

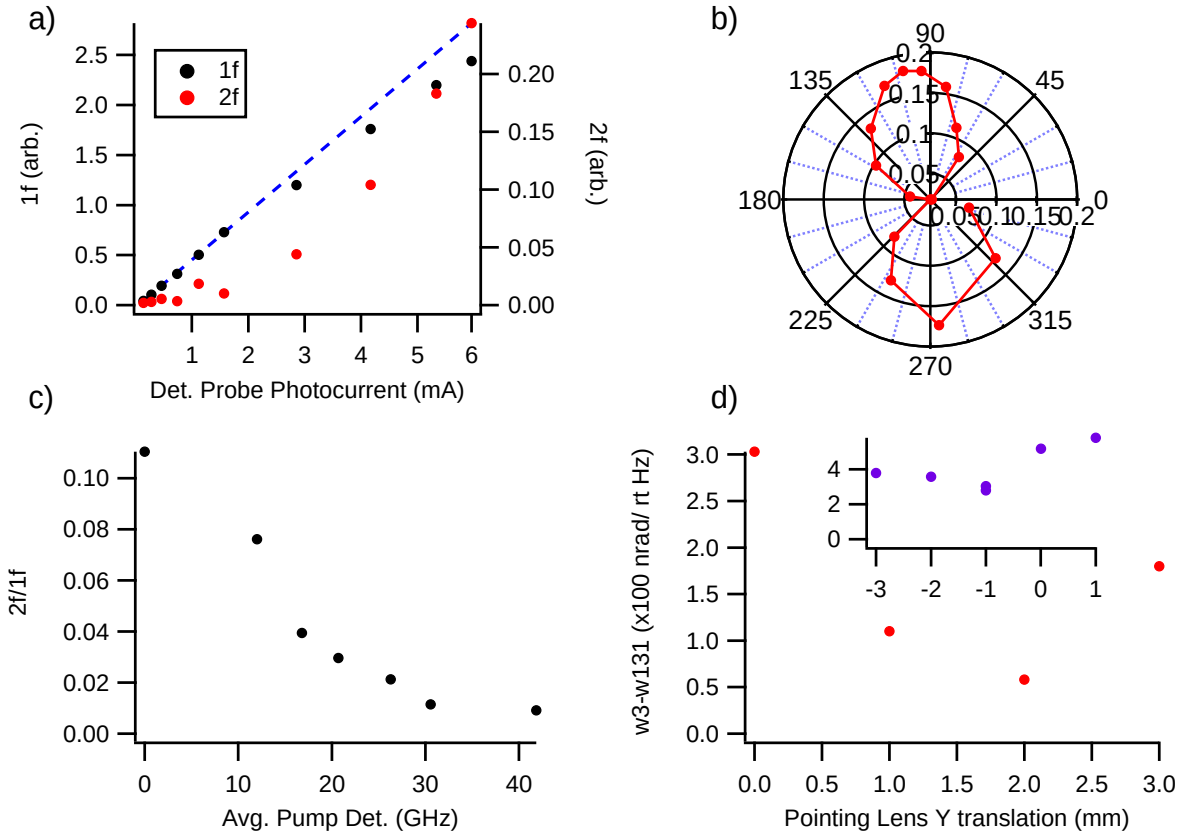

Figure 3.21: Sine polarization modulation non-linearity. a) $1f$ and $2f$ sideband power vs detected probe photo current. b) ratio of $2f/1f$ vs orientation of probe polarization. Zero is parallel to the optical table. c) ratio $2f/1f$ vs average pump laser detuning. d) sideband power vs pump pointing vertical (inset: horizontal) lens translation when applying a third modulation to the pump polarization at several hundered Hz.

mostly dependent on the V_{eom}'s offset voltage. Since applying a DC voltage to the EOM crystal can cause dielectric breakdown, we instead vary the quarter wave-plate following the EOM, which has the same influence on the SOP. The quarter wave retardance effectively changes the SOP for $V_{eom} = 0$. If the SOP (experienced by the Rb atoms in the vapor cell) for $V_{eom} = 0$ is not purely linear then the PM will no longer be an odd function. We found that non-zero power at the third harmonic was a good indicator of incorrect triangle modulation amplitude. If the retardance $> \pm\pi/2$ then the crest of the sine wave develops an inward facing cusp. If the retardance $< \pm\pi/2$ then the sine wave looks more like a triangle wave.

Pump and Probe Settings: Even after careful optimization of the SOP of the pump laser light incident to the cell we found that other probe and pump laser characteristics had profound influence on the sidebands produced by sine PM. The total pump power incident on the cell is ~ 40 mW with an e^{-2} beam diamter of about 8 mm such that the intensity is 5 mW/cm^2. The maximum power of the probe is 10 mW and its e^2 diameter is 5 mm such that its maximum intensity is 3 mW/cm^2. Although the probe is linearly polarized, it is good practice to keep the intensity 10x less than the pump such that any influence of residual circular polarization of the probe is negligible. Figure 3.21 shows how the power in the $1f$ and $2f$ sidebands of S_z depend on probe power. Once again the polarization was modulated sinusoidally at a single frequency and DC B_y applied to produce non-zero S_z. We see that the power at $1f$ depends non-linearly on probe power for probe power greater than roughly a mW. The power at $2f$ also depends non-linearly on the probe power. Besides the probe power, we also noticed that the orientation of the probe polarization relative to the optical table influenced the ratio of $2f/1f$ (see Fig. 3.21).

Also shown in Fig. 3.21 is the influence of pump detuning and pointing on the sidebands. As the pump detuning increases, the ratio $2f/1f$ decreases exponentially. This suggests that optical thickness effects may be present. The pointing angle of the pump lasers transverse to the optical table influenced the power at the sideband more than the pointing angle parallel to the optical table. We believe this behavior is due to the AC Stark shift. Recall that $S_z \sim \Omega_x R_y - \Omega_y R_x$. When we vary the vertical pointing of the pump we change R_y. An AC stark shift produces a magnetic field experienced by the Rb parallel to the pump polarization. If $\mathbf{R}$ is modulated at $1f$ and the AC stark shift is not balanced such that Ω_x also has $1f$, then S_z will have a $2f$ component. There is not a similar coupling for horizontal beam pointing (R_x). Also recall that $S_z \sim \Omega_z(\mathbf{\Omega} \cdot \mathbf{R})$. The product $\mathbf{\Omega} \cdot \mathbf{R}$ gives rise to $2f$ modulation on S_z for $\Omega_z \neq 0$. Consequently, the $2f$ sideband is very sensitive to bias pulse area.

Figure 3.22 shows the spectrum of S_z for dual frequency sine PM after careful optimization

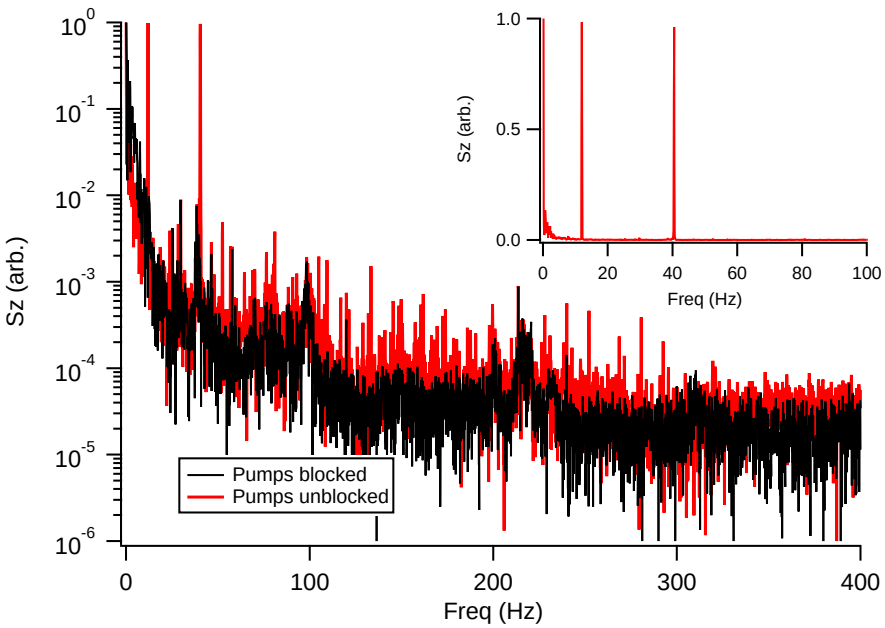

Figure 3.22: Measurement of S_z with DC B_y applied for dual frequency sine PM (no Xe excited). The black trace represents the Faraday rotation noise floor. Inset depicts linear scale of same data.

of the EOMs, magnetic fields, as well as pump and probe settings. The higher order harmonics are barely visible above the Faraday rotation noise. The Faraday detection noise is white noise limited for $f > 200$ Hz. Daily tuning of the pump SOP and magnetic fields was required to maintain such high fidelity sine PM. We believe the dominant source of day to day drift in the pump SOP is the EOM temperature.

Detection

We utilized two schemes dubbed $2f$ and S^{mod} to detect the Xe precession continuously and simultaneously. Neither detection scheme utilizes rectification. Consequently, the signal sizes are reduced compared to square PM with rectification, but there is no chance of $1/f$ detection noise being mapped to the Xe demodulation frequencies. The $2f$ detection scheme has been described above. Simply stated, since the Xe precesses at $1f$ and the gain of the magnetometer is modulated at $1f$, the magnetometer signal will have Xe phase information at $2f$ and DC.

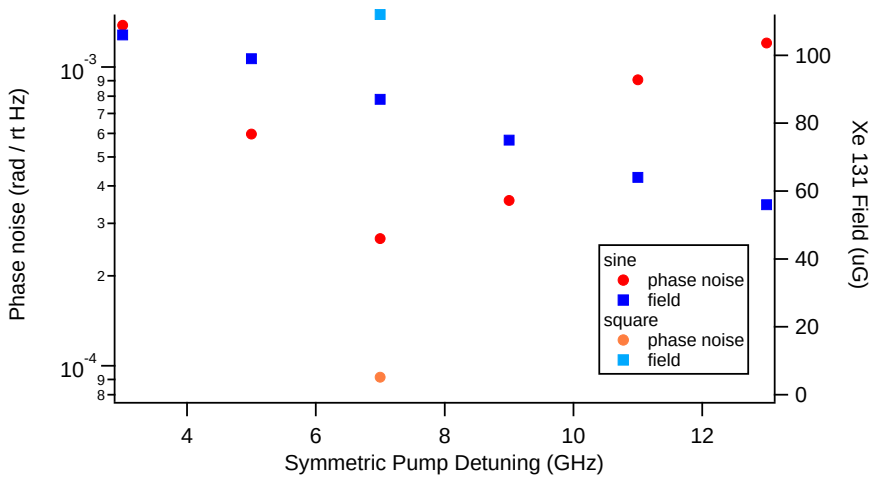

Figure 3.23: Phase noise and single species NMR amplitude vs pump detuning. Filled squares depict peak NMR amplitude (right axis). Filled circles depict phase noise (left axis). The RTD read 130 C for this data.

The phase information at DC is ignored because of the $1/f$ detection noise and the fact that both isotopes' phase information is present. For S^{mod} detection, we add an additional sinusoidal modulation to the pump PM such that $S_+(t) = [\sin(\omega^a t) + \sin(\omega^b t) + \sin(\omega_3 t)]/3$. The idea is for the ω_3 term to scatter signal up to higher frequency where the detection noise is lower. Detection takes place at $\omega_3 \pm \omega_K$. Figure 3.22 shows that the detection noise (black trace) at 300 Hz is nearly 10x lower than at 20 Hz. Adding a third modulation does reduce the detected signal by roughly 2x compared to $2f$ detection. This is because the amplitude of modulation which drives the Xe is reduced from 1/2 to 1/3. The modulation which scatters signal is also similarly reduced from 1/2 to 1/3.

Figure 3.23 shows how the SNR and excited NMR field of isotope b depends on average pump detuning. For this data $S_+(t) = \sin(\omega^b t)$ so that only isotope b was excited. The phase noise reported is for $2f$ detection. We see that the best phase noise is achieved for a detuning of 7 GHz. The excited Xe SE field depends very weakly on the pump detuning. Whatever noise is limiting the phase noise is strongly dependent on the pump detuning. Also included is a single measurement of the phase noise and excited Xe SE field for square wave PM (also $2f$ detection). We see that the increase in excited NMR amplitude is insufficient

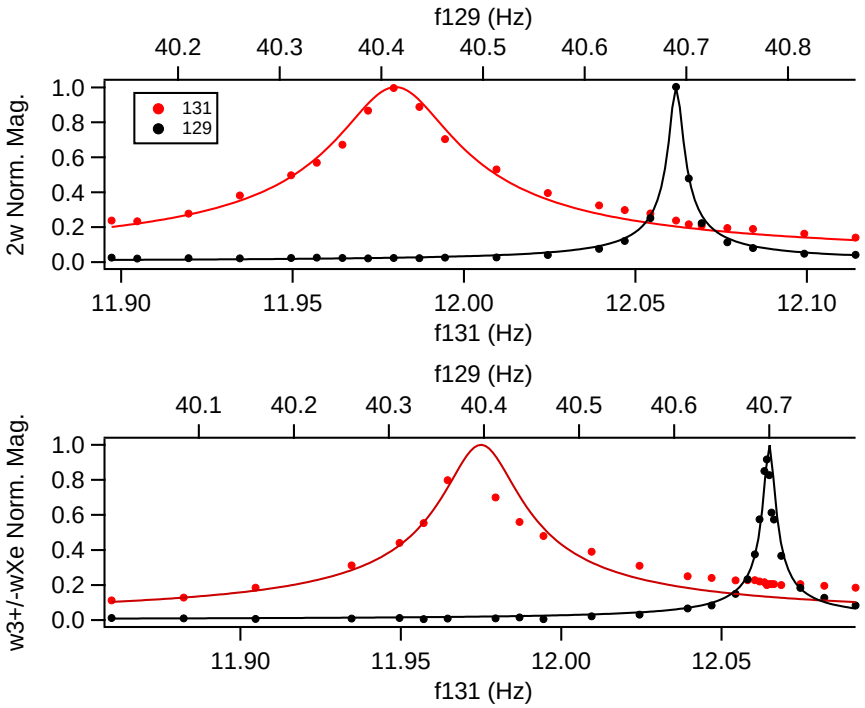

Figure 3.24: Sine PDM cross talk measurement. Top: $2f$ detection, bottom: S^{mod} detection. The limited deviation from the Lorentzian guides to the eye (solid lines) indicates low cross talk. The skewed ^{131}Xe NMR for S^{mod} comes from an interfering background signal.

to explain the improved SNR for square PM as compared to sine PM. For some reason sine PM has a lower SNR than square PM.

Cross Talk

Figure 3.24 shows the cross talk measured for $2f$ and S^{mod} detection schemes. We find little evidence of cross talk for either isotope in both detection schemes despite not rectifying. We attribute such low cross talk to the reduced amplitude of the PM sidebands. The S^{mod} detection scheme demodulation of isotope b is skewed because of an interfering background signal. The source of the interfering background was never completely understood. We found that the background depended on many of the same parameters which optimized the sine PM.

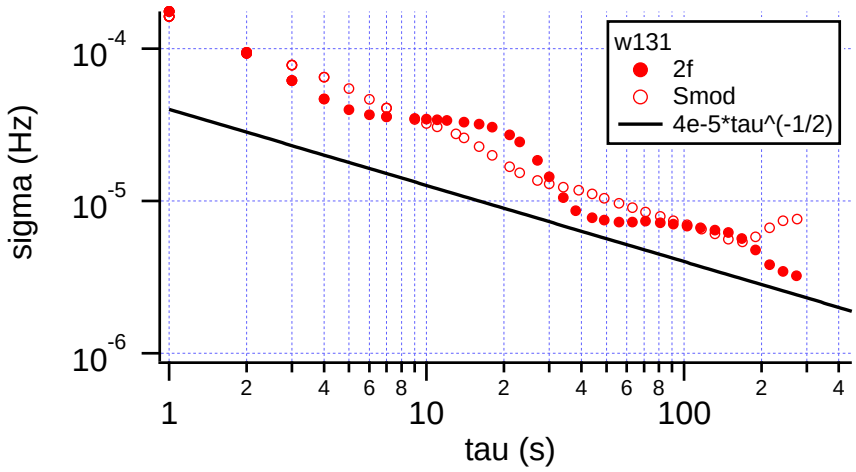

Figure 3.25: Sine PM Allan deviation of isotope b's calculated frequency with the measured phase of isotope a used to stabilize the bias field for both S^{mod} and $2f$ detection schemes.

Comagnetometry

Figure 3.25 shows the Allan deviations of the calculated ω^b for each detection scheme. Both detection schemes exhibit similar ARW of $\sqrt{2}$ 40 μHz/$\sqrt{\text{Hz}}\frac{\rho}{1+\rho} \sim 44$ μHz/$\sqrt{\text{Hz}}$ which is 3x greater than the ARW demonstrated with square PM. If the ARW were detection noise limited, then we would expect the ARW of S^{mod} to be better than $2f$ detection by a factor of 3 or more (see Fig. 3.22). The similar ARW between the two detection schemes suggests that their is some noise source inherent to sine PM which is absent in square PM and independent of detection noise. This conclusion is supported by the factor of 3 higher SNR found when implementing square PM as compared to sine PM (see Fig. 3.23).

Chapter 4

Pulse Density Modulation Excitation

> *The process of discovering that one's former beliefs are wrong...is what makes the pursuit of science so engrossing. The world would be a far better place for all of us if this joy in exposing one's own misconceptions were more common in other areas of human endeavor.*
>
> — N. David Mermin

Our motivation for pursuing a PDM comagnetometer has both esoteric and practical components. From an esoteric perspective, applying the bias field as a sequence of pulses enables the novel capability of producing bias field modulations which are experienced much more strongly by the noble gas nuclei than by the alkali-metal atoms. The PDM comagnetometer fully leverages this unique capability. From a practical point of view, as is outlined in Chapter 3, the PM comagnetometer detection scheme failed to detect the precession phase of each isotope individually with high fidelity. Since we attributed this shortcoming to PM itself we desired to excite the Xe without PM and hence solve the cross talk issue. This chapter demonstrates successful suppression of cross talk while maintaining the SNR and stability demonstrated with the PM comagnetometer. This progress was realized by developing a novel detection scheme which uses the unique response of each

isotope to the bias field modulation to detect their individual phases.

In this chapter the Xe NMR are excited by modulating the density (repetition rate) of bias pulses. We demonstrate a pulse driving circuit whose average area is at least 200x less sensitive to pulse density compared to the previously implemented pulsing circuit. The drive-to-noise ratio (DNR) of the PDM produced using the circuit is measured to be ~ 3500 $\sqrt{\text{Hz}}$. Using expressions from Ch. 2 we compare the efficiency with which each Xe isotope is excited for two different driving schemes. We demonstrate how gating the bias pulses enables rejection of gain modulation inherent to varying the pulse density while keeping the pulse width fixed. We excite $b_K^S K_\perp \sim 20$ μG for each Xe isotope simultaneously in a purely transverse fashion and show that the linewidth broadening caused by $B_S^K S_\perp$ is well compensated with DC transverse fields enabling NMR linewidths of ~ 15 mHz. We demonstrate the influence of ϵ_z on the phase of Xe precession as measured by the Rb atoms. We measure the cross talk of our unique demodulation scheme and find $\beta = -0.016$ and $\beta' < 0.002$ (see Eq. 3.9). We demonstrate real time feedback of each isotope's NMR making them effective oscillators. We demonstrate comagnetometry sufficient to resolve an ARW of ~ 10 $\mu\text{Hz}/\sqrt{\text{Hz}}$ and a bias instability < 1 μHz. The ARW is similar to the measured linewidths divided by the DNR and within a factor of 2 of the measured linewidths divided by the measured detection noise floor, suggesting that both DNR and detection noise floor need to be improved to reduce the ARW. The field suppression is measured to be 1800 when the influence of ϵ_z is accounted for which we estimate is sufficient to resolve a bias instability of ~ 200 nHz if the device were limited by bias field fluctuations. We show evidence suggesting the dominant sources of drift that limit the bias instability to greater than this value are $1/f$ transverse fields, and pump laser detunings.

We begin by reviewing the conclusions of Ch. 2 regarding PDM. We then describe modifications to the PM apparatus necessary to realize a PDM comagnetometer. We discuss what we learned as we optimized the apparatus. We demonstrate PDM comagnetometry and discuss measurements of various systematics. We conclude the chapter with a discussion

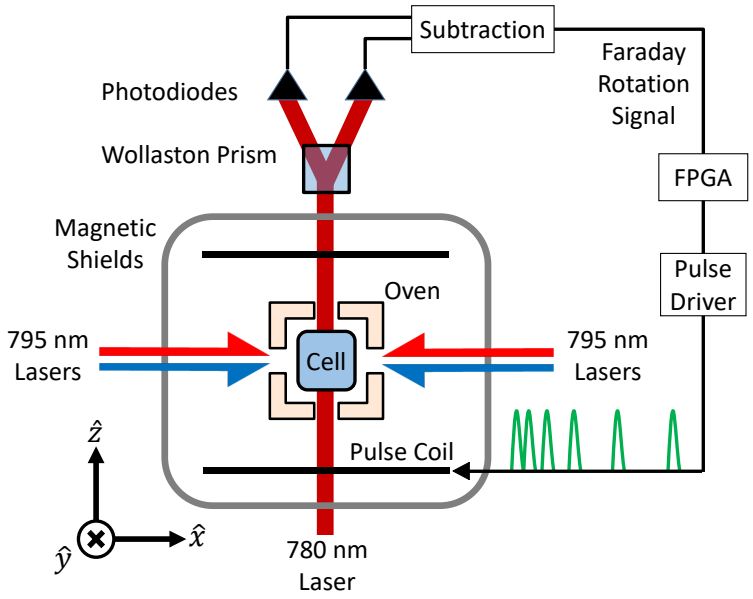

Figure 4.1: Schematic of apparatus. Field shim coils are not shown. The green trace depicts the frequency modulated bias field pulses.

of ongoing studies and future paths of inquiry. Unlike Chapter 3, many of the contents of this chapter have been published [Thrasher et al. (2019)].

4.1 PDM general principles

Figure 4.1 shows the schematic for PDM excitation. In contrast to PM excitation, the polarization of the pump lasers is constant in time so the EOMs are no longer present. The repetition rate of the bias pulses is modulated to excite both Xe isotope's NMR simultaneously (depicted in green).

	A	B
$\omega_d^a =$	$3\omega_1 + \omega_2$	ω_2
$\omega_d^b =$	ω_1	ω_1

Table 4.1: PDM drive scheme comparison.

Excitation

As derived in Ch. 2, the time average of the transverse Xe polarization of isotope K for PDM excitation is

$$K_\perp = \frac{\Gamma_S^K S_\perp}{\Gamma_2} j^K, \tag{4.1}$$

$$j^K = J_{-p}(\frac{\gamma^K B_1}{\omega_1}) J_{-q}(\frac{\gamma^K B_2}{\omega_2}) \tag{4.2}$$

where p and q are chosen to satisfy the resonance condition $\omega_d + p\omega_1 + q\omega_2 \sim 0$. In Ch. 2 we also showed that the influence of finite SNR on rotation is minimized when $K_\perp^b = \rho K_\perp^a$. The size of modulations B_1 and B_2 which achieve this ratio of $K_\perp$ depends on the resonance condition, i.e. choice of p and q. Figure 4.2 depicts j^K vs B_1/B_0 for two resonance conditions (summarized in Table 5.1) assuming $B_2 = B_0 - B_1$. The B_1 that satisfies $K_\perp^b = \rho K_\perp^a$ for pumping scheme A produces a $K_\perp^a$ roughly twice that produced at the B_1 that satisfies $K_\perp^b = \rho K_\perp^a$ for pumping scheme B. For this reason we find pumping scheme A superior to pumping scheme B. The rest of the data presented in this chapter is acquired using pumping scheme A unless noted otherwise.

Detection

From Eq. 2.8 and Eq. 2.16, the magnetometer signal S_z can be written as

$$S_z = A_\perp^a \sin(\delta^a + \alpha^a - \epsilon_z) + A_\perp^b \sin(\delta^b + \alpha^b + \epsilon_z), \tag{4.3}$$

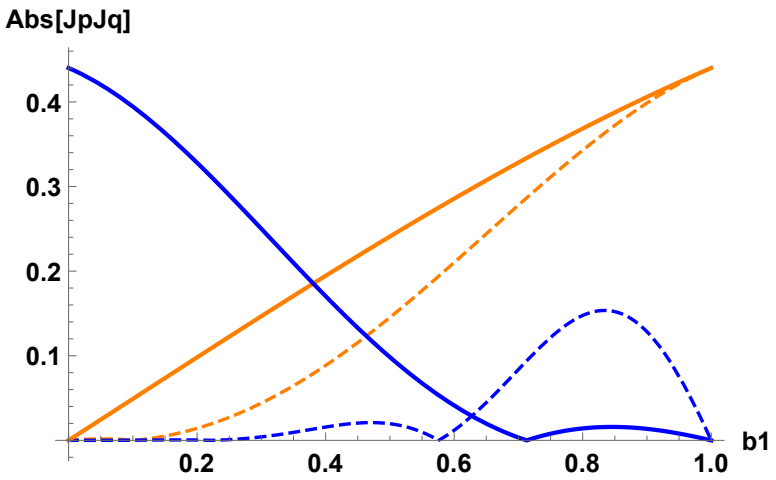

Figure 4.2: Plot of magnitude of $J_{-p}(\frac{\gamma B_1}{\omega_1})J_{-q}(\frac{\gamma B_2}{\omega_2})$ vs $b_1 = B_1/B_0$ for two different pumping schemes with $B_2 = B_0 - B_1$. Blue traces are for isotope a and orange traces are for isotope b. Dashed lines are for pumping scheme A: $p^a = 3$, $q^a = 1$, $p^b = 1$, $q^b = 0$. Solid lines are for pumping scheme B: $p^a = 0$, $q^a = 1$, $p^b = 1$, $q^b = 0$.

where $A_\perp = -\gamma^S b_K^S K_\perp R/\Gamma'^2$. Note that the Rb precession phase includes both the Xe precession phase shift δ and the magnetometer phase shift ϵ_z. In contrast to PM excitation, Eq. 4.3 does not need to be rectified before lock-in detection.

The precession phase of each isotope can be extracted from S_z by demodulation with $\cos(\alpha)$. We refer to this demodulation method as "α-space" demodulation. For example,

$$\int d\alpha_0^b S_z \cos(\alpha_0^b) = \int dt \frac{d\alpha_0^b}{dt} S_z \cos(\alpha_0^b) = A_\perp^b \sin(\delta^b + \epsilon_z) + res., \tag{4.4}$$

where $\alpha_0^K = \alpha_{off}^K + p^K\theta_1 + q^K\theta_2 + \gamma_0^K \int dt B_z(t)$ is the reference phase generated on the FPGA. Our chosen drive scheme (see discussion above) means $\theta_1 = \int \omega_d^b dt$ and $\theta_2 = \int \left(\omega_d^a - 3\omega_d^b\right) dt$ such that the only free parameters in the expression for α_0^K are γ_0^K and α_{off}^K. The parameter α_{off}^K is chosen such that the quadrature is purely dispersive vs δ. We simply choose $\gamma_0^a = 1177.69$ Hz/G and $\gamma_0^b = 349.1$ Hz/G. The exact value used is superfluous however because $B_z(t)$ is AC coupled (see cross talk discussion below for more details). We sample evenly in time for experimental convenience, necessitating the $\frac{d\alpha}{dt}$ in the demodulation.

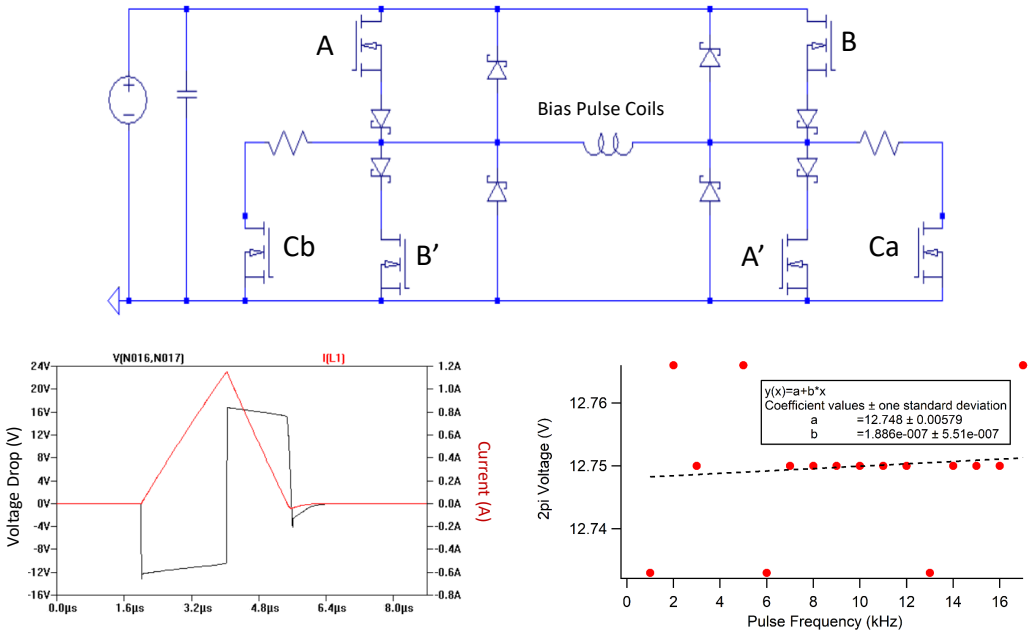

Figure 4.3: Modified pulsing circuit. Top: Circuit schematic. Bottom left: simulated voltage and current across inductor. Bottom right: measurement of $V_{2\pi}$ vs pulsing frequency.

4.2 Apparatus

The apparatus used for the data described in this chapter is similar to that described in Ch. 3. Cell M was used for all the data in this chapter. The only significant change to the apparatus was the circuit used for driving the pulsing coils. The pulsing circuit was modified to reduce pulse area dependence on repetition rate. Such an improvement was necessary because the magnetometer gain would be modulated at the PDM frequencies if the pulse area does not produce precisely 2π precession of the Rb atoms. Modulation of the magnetometer gain at the PDM frequencies is undesirable because it could lead to cross talk (see discussion below).

A schematic of the new pulsing circuit developed by Mike Bulatowicz and Susan Sorensen is shown in Fig. 4.3. The circuit is based on a bipolar H-bridge design and is capable of producing both positive and negative pulses. The research presented in this chapter only

utilized pulsing with a single polarity. When a pulse is desired, a TTL trigger from the FPGA activates the A MOSFETs so that current from the capacitor flows from A to A' through the bias pulse coils. After a few microseconds the A MOSFETs are opened such that a recovery current flows through the Zener diodes parallel to the B MOSFETs. Finally, gate C_a is closed so that ringing due to parasitic capacitance of the Zener diode and MOSFETs is snubbed.

We measured how the voltage required to produce 2π pulses varied with pulsing frequency $f_{2\pi}$ by first nulling the magnetometer response to AC B_x and B_z fields while the pulses were not triggered. We were careful to cancel the AC stark effect. Next, we triggered the bias pulses at a constant $f_{2\pi}$ of our choosing and increased the voltage across the pulsing circuit's capacitor (thereby changing the magnetic pulse's area) until the second voltage the Rb showed minimal response to an AC B_x (the first dip in response occurs when the pulse area corresponds to π Rb rotation). This process was then repeated for various $f_{2\pi}$. The resolution with which we can vary $V_{2\pi}$ was limited to 15 mV by the power supply we used. Figure 4.3 depicts a linear fit to the data. The measurement is clearly limited by the resolution of the power supply. The upper bound on the slope is 2×10^{-4} V/kHz, roughly 200x smaller than the slope measured using the old pulsing circuit [Korver (2015)]. We believe a key ingredient to the improved performance of this circuit compared to the old circuit was the use of low recovery diodes which exhibit very weak dependence on temperature. When the pulse density increases, the average power dissipated by the diode also increases. If the diode is sensitive to temperature then variations in pulse density can cause changes to the bias pulse area.

Besides exhibiting minimal dependence of $V_{2\pi}$ on the bias repetition rate, we also desire the circuit to produce bias repetition rate modulations with high fidelity. Since for PDM excitation we drive the Xe NMR using the bias pulse repetition rate, the fidelity with which we modulate the pulses limits the DNR of the Xe isotopes. The Xe precession phase is sensitive to both the timing jitter of the 2π pulses as well as variations in pulse area (the Rb

is sensitive to pulse area fluctuations but first order insensitive to timing fluctuations).

We measure the PDM DNR in a way which is similar to the measurement of the DNR of the EOMs mentioned in Ch. 3. Whereas the phase noise from the EOMs produces S_z fluctuations, phase noise from the PDM appears as B_z noise. Since S_z is not first order sensitive to B_z we utilize a parametric modulation technique [Li et al. (2006)]. We apply an AC B_x at $\omega_{pm} = 900$ Hz and $B_{pm} \sim 1$ mG. The S_z signal at ω_p (which we isolate using a lock-in amplifier) is proportional to [Korver et al. (2015)],

$$S_z(\omega_{pm}) \sim \frac{\gamma^S B_{pm} S_x}{\Gamma'^2} B_z. \tag{4.5}$$

To measure the DNR we modulate our pulse density according to $\omega_p(t) = \omega_{p0} + b_1 \sin(\omega_1 t + \phi_1)$. If the pulse area is not 2π then this modulation will appear as a B_z experienced by the Rb such that $B_z = B_{z0} + \beta\omega_p(t)/\gamma^S$, where B_{z0} is the stray magnetic noise inside the shield, and β is the discrepancy of the pulse area from 2π. We isolate the contribution to $S_z(\omega_{pm})$ from ϕ_1 by using a second lock-in amplifier referenced to ω_1. The outputs of this second lock-in are,

$$V_Q = \langle S_z(\omega_{pm}) \cos(\omega_1 t) \rangle \sim \eta\, \beta \sin(\phi_1) + \delta V_Q, \tag{4.6}$$

$$V_I = \langle S_z(\omega_{pm}) \sin(\omega_1 t) \rangle \sim \eta\, \beta \cos(\phi_1) + \delta V_I, \tag{4.7}$$

where V_Q and V_I are the quadrature and in-phase components respectively, $\eta = b_1 B_{pm} S_x / \Gamma'^2$, and the δVs represent measurement noise inherent to each component. The ratio V_I/V_Q is equal to $\cot(\phi_1) \equiv DNR$ in the large β limit.

Figure 4.4 shows three separate measurements of V_I/V_Q vs bias pulse width (which is proportional to β) for $\omega_1 = 5$, 50, and 100 Hz. We fit the data for each ω_1 using the ratio of Eqs. 4.6 and 4.7. Figure 4.4 shows the resulting $\delta\phi_1$ and its uncertainty from the fit for each ω_1. The DNR shows a weak dependence on ω_1 and is approximately 6000 $\sqrt{\text{Hz}}$. This is more

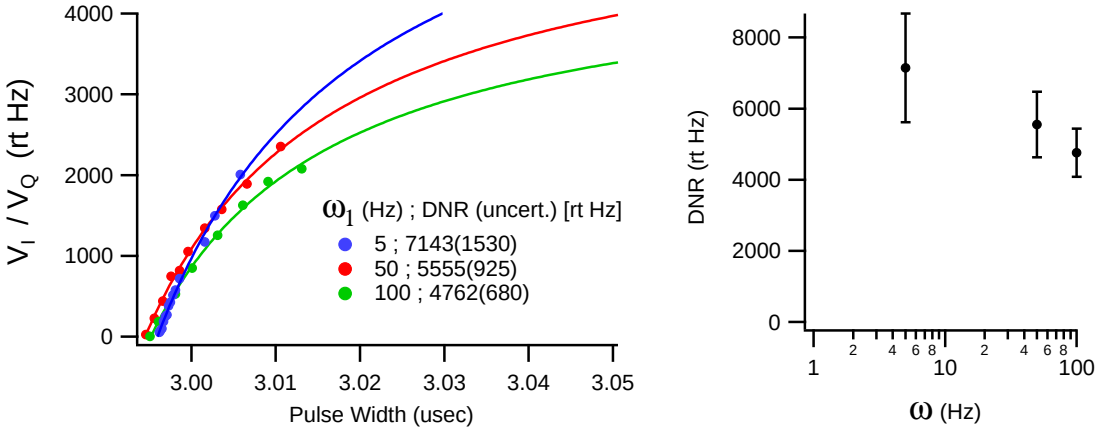

Figure 4.4: Measurement of the DNR of PDM for three different ω_1. Left: V_I/V_Q vs pulse width for various ω_1. Filled circles are measured data and lines are fits to the data. The legend lists the DNR and its uncertainty from the fit for each ω_1. Right: linear-log plot of DNR from data set fits vs ω_1. Error bars show standard deviation of fit uncertainty. For these data sets $b_1 = 0.74$.

than 100x less than the SNR limit due to photon shot noise (see Ch. 2). We should note that when both Xe isotopes are excited the pulse density modulation is bi-periodic, unlike the experiment described here. This fact may limit the applicability of this data. What limits the DNR of the PDM is uncertain. One possible albeit unlikely source is timing jitter on the pulsing trigger. The FPGA is used to synthesize the bias pusle trigger. The finite update rate of the FPGA DDS calculation (10 MHz) will cause timing jitter on the pulse triggers. Another source of finite DNR may be the pulsing circuit. Perhaps temperature drifts influence the pulse area produced by the circuit.

4.3 Detection optimization

Although we managed to construct a pulsing circuit whose $V_{2\pi}$ is independent of the PDM frequency, the finite duty cycle of the pulses means that the magnetometer gain will still be modulated at the PDM frequencies. Any SE collisions that occur during a bias pulse will contribute to relaxation. Hence, the magnetometer gain will be increasingly degraded

as pulses are applied more frequently with constant pulse width. For the ω_p modulation presented in this work, the observed magnetometer gain varied up to a factor of two due to this effect.

We suppress the influence of gain modulation on the detection by gating the 2π pulses. After the pulses are gated off, we wait for the magnetometer gain to recover before recording the Faraday signal (see Fig. 4.5). If we do not gate the pulses, we see a background on the recorded Faraday signal which corresponds to harmonics of the pulsing modulation frequencies. We find that waiting twice the $1/e$ recovery time of the Rb magnetometer before recording the Faraday signal suppresses this background. We modulate the 2π pulse repetition rate (depicted in Fig. 4.6) as

$$\omega_p(t) = \omega_{p0}\, g(t)(1 + b_1 \cos(\omega_1 t) + b_2 \cos(\omega_2 t)), \tag{4.8}$$

where $g(t) = [\text{sign}(\cos(\omega_3 t)) + 1]$ is the time dependence of the gating, $\omega_1 = \omega^b$ and $\omega_2 = \omega^a - 3\omega^b$, and b_1 and b_2 set the depth of modulation. We note in passing that we originally tried square wave modulation (replace cos in the equation above with sign(cos)) but saw interference between ω_3 and higher harmonics of PDM frequencies. Interference between these two frequencies appeared as narrow peaks in the measured Xe phases at frequencies < 1 Hz.

Figure 4.7 depicts the measured NMR lineshapes deduced using α-space demodulation. The data were acquired with one isotope driven on resonance while the other isotope's detuning was varied. Similar to PM, the linewidths demonstrated are only possible due to cancellation of the Rb SE experienced by the Xe nuclei. Since the Rb polarization is not modulated, the Rb SE field is at DC. Hence, we apply a DC B_x to cancel the Rb SE field. Figure 4.7 also shows the measured linewidths for isotope b as B_x is varied.

The field modulation parameters were, $\omega_3 = 2\pi \times 200$ Hz, $b_1 = 0.73$ and $b_2 = 0.15$, and $\omega_{p0} \approx 2\pi \times 13.2$ kHz, resulting in average precession frequencies of ≈ 33.3 Hz and ≈ 9.9

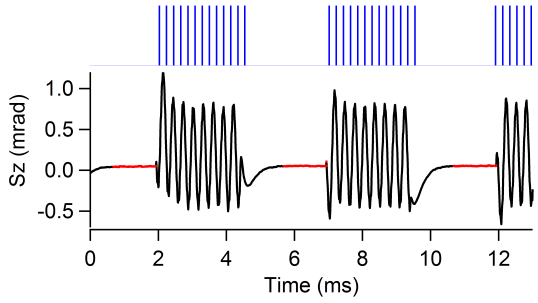

Figure 4.5: Influence of bias pulse gating on Rb magnetometry. (Top) Time dependence of the few percent duty cycle bias pulses. (Bottom) Measured time dependence of raw S_z signal from polarimeter. Red data are averaged together to measure the Xe precession at an effective sampling rate of ω_3. The $\approx$ 3kHz oscillation present when pulsing comes from interference between the AC heater drive and the pulses.

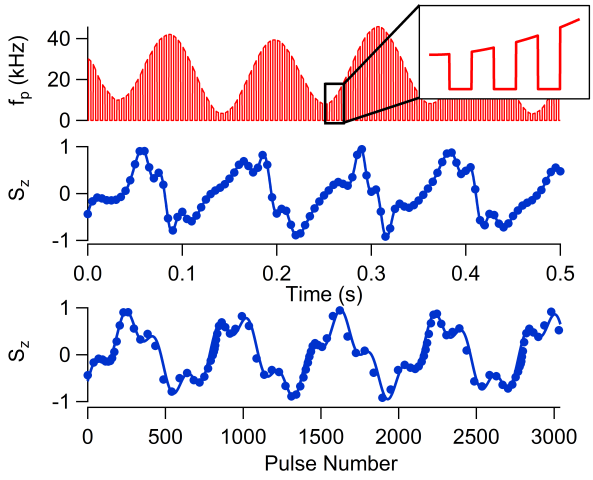

Figure 4.6: Time dependence of bias pulse repetition rate (top) and normalized S_z sampled at ω_3 (middle) for $\Delta^a = \Delta^b = 0$. Corresponding pulse number dependence of normalized S_z (bottom). Filled circles are measured data. Lines are theory fits to the data. Inset depicts gating of the bias pulses.

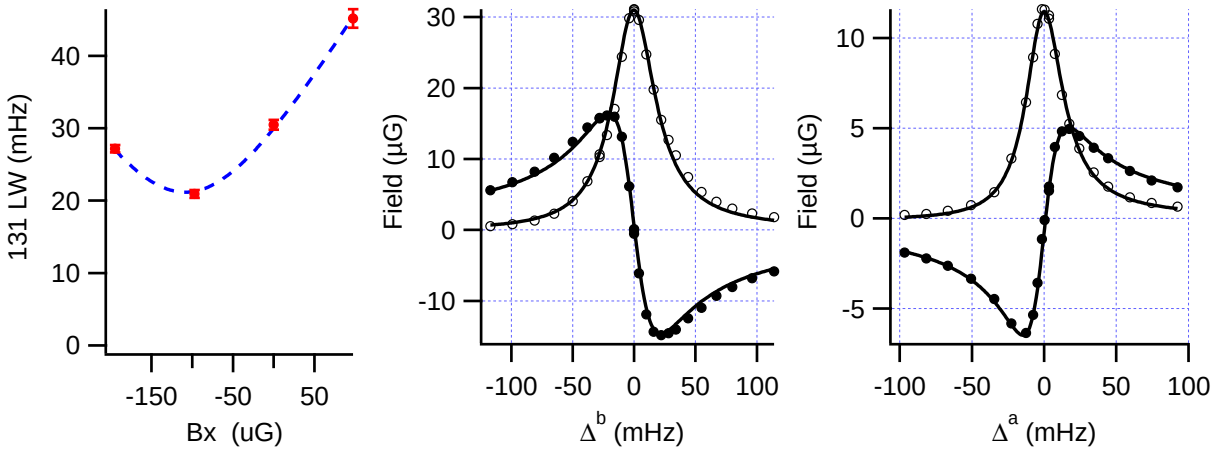

Figure 4.7: Xe NMR Lineshapes. Left: half-width-half-maxmium linewidth of isotope b vs B_x. Middle: $b_a^S K_\perp^a$ vs Δ^a. Right: $b_b^S K_\perp^b$ vs Δ^b. Filled circles are measured K_y and open circles are measured K_x. Lines are Lorentzian fits to the data.

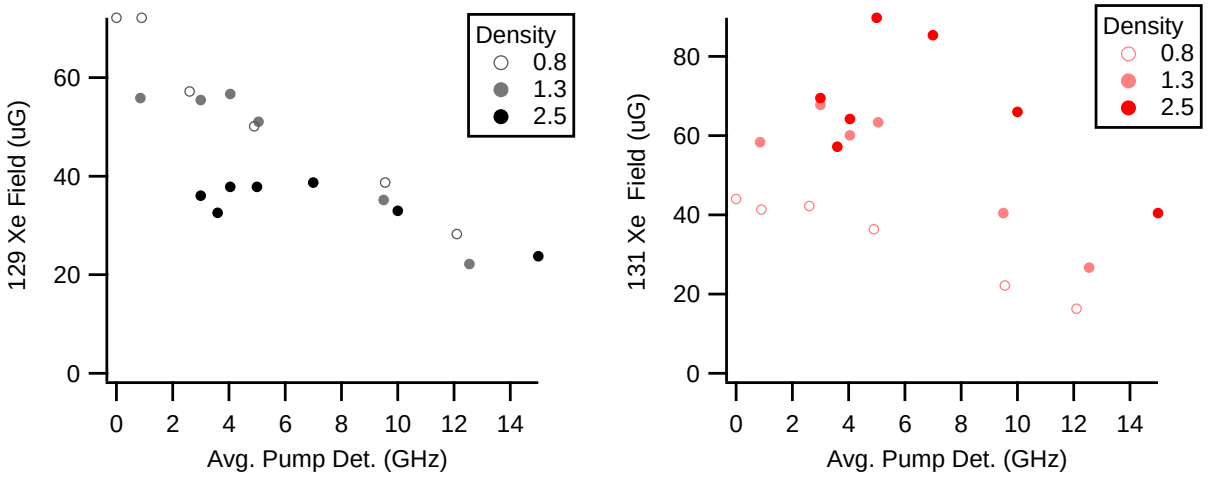

Figure 4.8: Xe amplitudes vs average pump laser detunings. The different colors correspond to different Rb densities ($\times 10^{12}\mathrm{cm}^{-3}$).

Hz for ^{129}Xe and ^{131}Xe, respectively. Under these conditions, the amplitude of B_m was approximately 10 B_w. Only the modulation of 2π pulses allows for the Xe to experience such a large modulation while preserving the fidelity of the Rb magnetometer. Limiting $b_1 + b_2 < 0.9$ avoids producing Xe precessions near the $1/f$ detection noise without requiring reversals of the pulsing direction. For our choice of ω_{p0}, $b_1 + b_2 = 0.88$ ensures that the instantaneous precession frequency of the ^{131}Xe never goes below 1 Hz. We use a moving average filter to perform the integration over time from Eq. 4.4. The moving average filter most strongly attenuates frequency content at integer multiples of ω_3/N. Since ρ was within 0.05% of 27/8, we used the moving average filter to suppress residuals of the demodulation at ω_d^a, $\omega_1 = \omega_d^b$, and ω_2 by setting $\omega_d^a = \omega_3/6$ (at the start of measurements) and fixed $N = 27 \times \omega_3/\omega_d^a = 162$. For ^{131}Xe we measure $b_b^S K_\perp^b \approx 30$ μG or 0.1% polarization and a linewidth of 21.2(3) mHz. For ^{129}Xe we measure $b_a^S K_\perp^a \approx 10$ μG or 0.3% polarization and a linewidth of 15.6(3) mHz. The measured Xe polarizations and SE fields are in agreement with estimates (see App. A).

The influence of varying the average pump detunings on the excited Xe field size is depicted in Fig. 4.8. This data was acquired by choosing the detunings of one of the pump

lasers and then picking the other pump laser's detuning to roughly cancel the average AC stark shift. The average of the two pump lasers detunings was recorded and then NMR of each isotope under simultaneous excitation conditions were scanned. The excited Xe fields of both isotopes are reduced for small detunings as the Rb density is increased. We attribute such behavior to running out of pump photons due to the Rb's increasing optical thickness. We also see evidence of a temperature dependent wall relaxation mechanism for isotope a: as the Rb density increases, isotope a's amplitude hardly changes at large detunings. The amplitude of isotope b however shows more of a linear trend with Rb density at large detunings. The comagnetometry data presented in this chapter is acquired with average pump detunings of 12 GHz unless otherwise noted. We chose to operate at 12 GHz because it is the smallest pump detuning where balancing the AC Stark effect to less than 10 μG equivalent B_y is readily achievable when the Rb density is 10^{13} cm^{-3}.

noise

The gate frequency ω_3 is limited by the response of the magnetometer. The average pulsing frequency should be chosen such that the maximum instantaneous precession frequency of isotope a is less than $\omega_3/2$ to satisfy Nyquist's criterion. The pre-amplifier that converts the difference photo current (from the balanced polarimeter) to a voltage is programmed to have a 12 dB/octave low pass filter with a corner at $f_{LPF} = 10$ kHz. The DAQ acquires $M = 128$ data points at a rate of $f_s^{DAQ} = 100$ kHz every $1/f_3 = 5$ msec. These data are then averaged together to produce a single measurement of S_z at f_3. These parameters were carefully selected to minimize the amount of gain modulation and avoid aliasing white noise onto S_z. An inequality that describes how each of these parameters are related is $2f_{LPF} < Mf_3 < f_s^{DAQ}/2$.

Figure 4.9 demonstrates the influence of gating on the Faraday detection noise. All the traces shown were acquired with $f_3 = 200$ Hz, $M = 128$, $f_1 = 5.1$ Hz, $B_1/B_0 = 0.74$, and

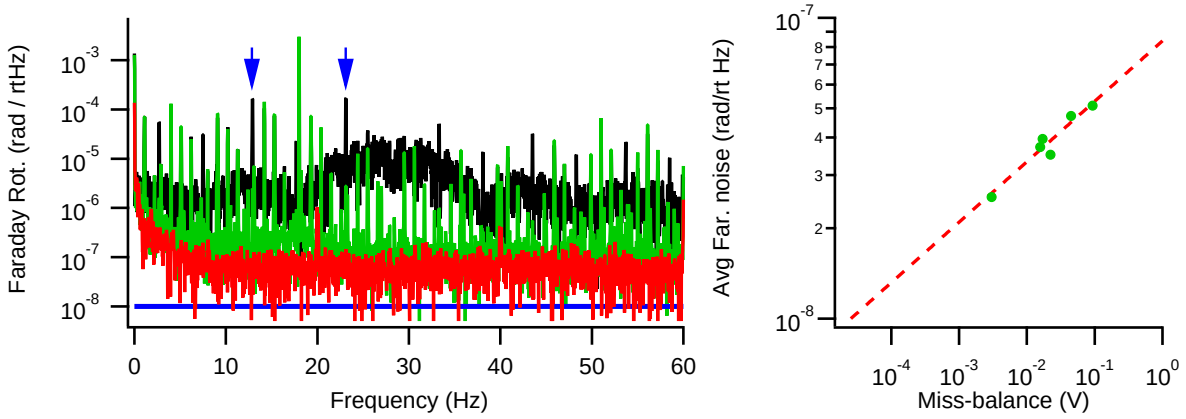

Figure 4.9: Influence of gating on detection noise. Left: amplitude spectral density of Faraday rotation. See text for details. Right: Average Faraday rotation noise vs. miss-balance voltage. The pre-amplifier gain was 20 μA/V.

$B_2/B_0 = 0$. No Xe is excited in this measurement. We apply an 18 Hz AC B_y so that we can measure gain modulations. Gain modulation appears as $f_1 = 5.1$ Hz sidebands on the AC B_y carrier frequency (see the blue arrows). For the black trace, data are acquired while the magnetometer gain responds to the gating of the bias pulse frequency. The noise spectrum is similar to that acquired without gating. The green trace however, depicts data acquired only when the pulses have been gated off for 2.5 msec (similar to the red data in Fig. 4.5). Avoiding recording the Faraday rotation signal while the magnetometer gain responds to the bias pulse frequency change reduces the white noise level down to nearly the probe noise limit and also reduces the content at 18 ± 5.1 Hz by two orders of magnitude. We found that the white noise of the green trace did not change when we switched to dual frequency PDM. This is in contrast to PM where dual frequency modulation resulted in substantial increase to the white noise of S_z (see Fig. 3.10). We note that if we reduce f_3 to 100 Hz the sidebands due to gain modulation can be suppressed down to the white noise floor. We did not choose to operate at $f_3 = 100$ Hz despite the improved rejection of gain modulation because it would require we reduce the average bias field making us more susceptible to $1/f$ detection noise (especially for detecting isotope b).

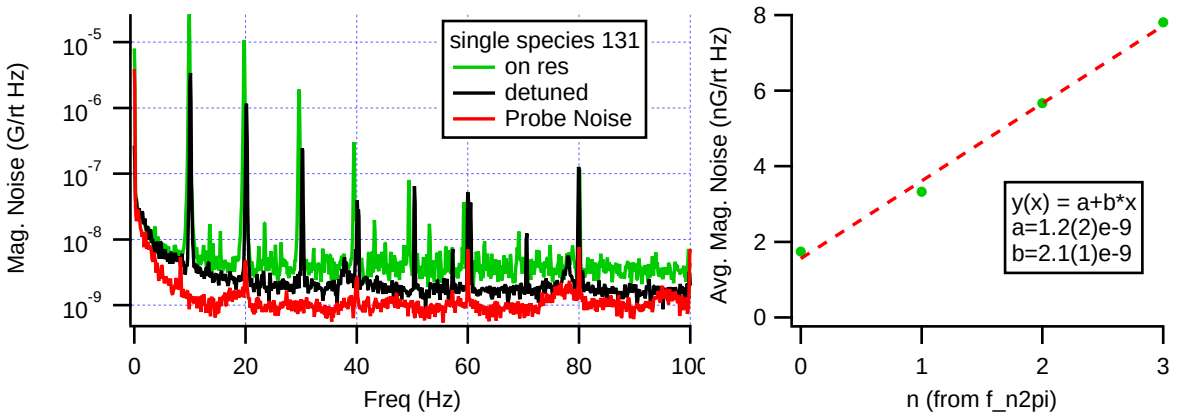

Figure 4.10: Left: magnetic noise when only isotope b is driven. Right: average magnetic noise vs number of 2π Rb rotations per pulse when isotope b is driven on resonance ($n = 0$ is the probe noise).

The probe noise (red trace, acquired by blocking the pump lasers) is roughly an order of magnitude greater than the photon shot noise (blue line) calculated from the total average detected photo current (0.8 mA for this data). Increasing the probe power did not reduce the probe white noise but it did reduce the electronic noise (not shown) which was less than the probe noise. We found that the average Faraday rotation noise from 20 to 100 Hz (pumps unblocked) showed a power law dependence (dashed red line) on miss-balance (I_{diff}) of the polarimeter (see Fig. 4.9). The average value of I_{diff} over a measurement period determines how well the device rejects common mode noise (such as probe power fluctuations) between the two photo diodes. This data suggests that in order to reach the photon shot noise we need to stabilize the average photo current difference to ∼200 pA. This can be achieved using an auto-balancing circuits [Hobbs (1997)]. We did not employ such a circuit during my tenure because, as we will see below, the Xe SNR is not limited by the detection noise.

Besides average I_{diff}, we also found that the white noise of S_z depended on n, the number of 2π precessions the Rb undergo per pulse. Figure 4.10 depicts the magnetic noise (Faraday rotation noise scaled by the magnetometer gain) recorded when only isotope b is driven ($b_1 = 0.74$, $b_2 = 0$). The white noise is reduced as the Xe is driven off resonance (compare

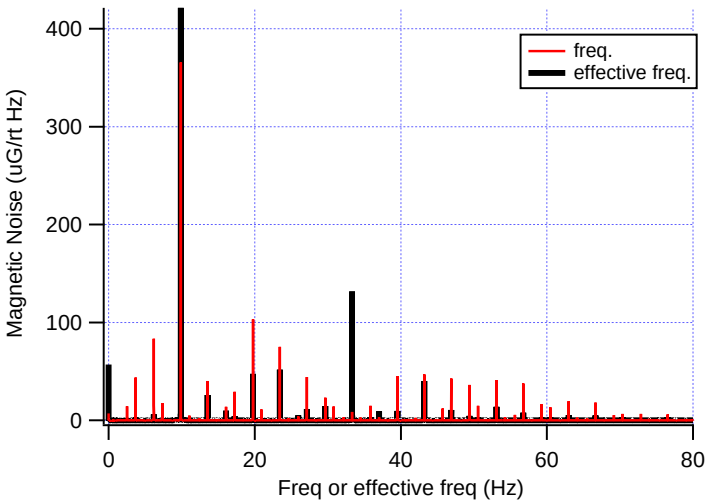

Figure 4.11: Xe sideband collection.

green and black traces). The average white noise from 24.5 to 25.8 Hz (measured while isotope b is resonantly excited) exhibits a linear dependence on n. The source of this white noise is uncertain. The fact that it is proportional to the excited Xe amplitude suggests its source is the Xe. The fact that it is proportional to n suggests it may be due to discrete Xe precession, i.e. the fact that the Xe precesses for only the duration of the bias pulses and not continuously. If such were the case then we expect the dependence of average magnetic noise per n measured when only isotope a is excited to be ρ greater than when only isotope b is excited. We have yet to measure how n influences the magnetic noise when only isotope a is excited. This white noise could possibly really be signal. Our detection of the Xe phase assumes continuous Xe precession. We assumed such because each pulse produces only a few mrad of precession per pulse.

In order to further characterize the validity of our α-space detection scheme we analyzed our signals in terms of pulse number. When the Xe isotopes are on resonance, the complicated precession in time is merely a superposition of sine waves in pulse number (see Fig. 4.6). We record both the pulse number and S_z signal at a constant rate in time. We then plot S_z vs pulse number. Since the pulse repetition rate is constantly varying, the number of pulses

between S_z samples is not fixed. We interpolate the S_z data so that there is one sample of S_z per pulse. We then convert pulse number to an effective time by dividing by the average pulsing frequency. Figure 4.11 depicts the amplitude spectral density of S_z vs frequency (red) and effective frequency (black). We see that the interpolated effective frequency increases the spectral content at the Xe resonance frequencies especially at ω^a which increases an order of magnitude. The sideband collection is not perfect as there is substantial content at other frequencies. A possible source of these spurious sidebands are errors in the linear interpolation. After all, there are times when isotope a is precessing sufficiently fast such that it is only sampled three times in a cycle. Another possible explanation is that there exists Xe precession which is not due to the pulses.

confirmation of ϵ_z

The influence of ϵ_z is readily observed by comparing the phase of response to an AC B_z of each isotope as measured by the Rb. We write,

$$\begin{aligned}\mathrm{Arg}(\tilde{\delta}^a - \tilde{\epsilon}_z) - \mathrm{Arg}(\tilde{\delta}^b + \tilde{\epsilon}_z) \\ \approx \tan^{-1}\left(\frac{\omega(B_w\gamma^a - \Gamma_2^a)}{-\omega^2 - B_w\gamma^a\Gamma_2^a}\right) - \tan^{-1}\left(\frac{\omega(B_w\gamma^b + \Gamma_2^b)}{\omega^2 - B_w\gamma^b\Gamma_2^b}\right), \quad (4.9)\end{aligned}$$

where we have taken $\tilde{\Delta} \approx \gamma\tilde{B}_{z0}$ and $\tilde{\epsilon}_z \approx \tilde{B}_{z0}/B_w$. With both isotopes simultaneously excited on resonance but open loop (no frequency correction), an ancillary AC B_z is applied at frequency f. The phase of oscillation as measured by the Rb ($\delta \pm \epsilon_z$) at frequency f relative to the ancillary B_z is recorded for each isotope. The difference of the phase of responses vs f is shown in Figure 4.12. If there were no magnetometer phase shift (i.e., if $\tilde{\epsilon}_z = 0$) the phase difference would approach zero with increasing frequency (see dashed line in Fig. 4.12). Instead, we see the phase difference increase with f, consistent with $\tilde{\epsilon}_z \neq 0$. The solid line is a fit to the data. The fit suggests a $B_w = 3.5 \pm 0.3$ mG, in agreement with the B_w we

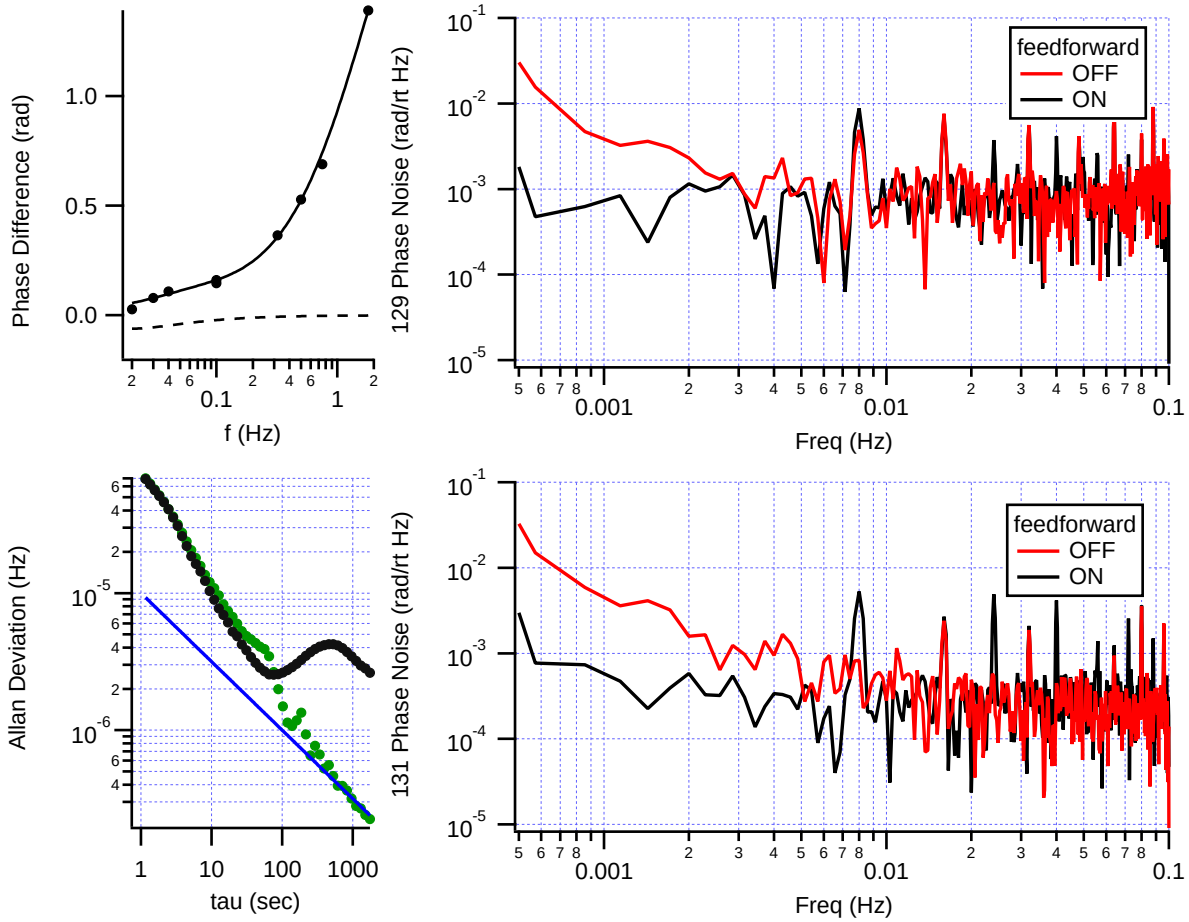

Figure 4.12: Influence of ϵ_z. Top left: difference of each isotope's phase of oscillation as measured by the Rb ($\delta \pm \epsilon_z$) relative to the ancillary B_z vs frequency of ancillary B_z. Top right: phase noise of fake isotope a with and without ϵ_z feedforward. Bottom right: phase noise of fake isotope b with and without ϵ_z feedforward. Bottom left: Standard Allan deviation of rotation computed using fake Xe phase noise with (green) and without (black) feedforward. The blue line shows 10^{-5} Hz/$\sqrt{\tau \text{Hz}}$.

measure by recording the magnetometer response vs applied B_y of 3.1 ± 0.1 mG.

A second confirmation of our model for ϵ_z is long term drift of the phase of a rotating fake Xe signal as measured by the Rb. For real Xe, our detection scheme measures $\delta \mp \epsilon_z$. For a rotating fake Xe however $\delta = 0$. Hence, any drift we observe in each isotope's phase detection channel when fake Xe signals are applied attributed to ϵ_z. Figure 4.12 depicts the phase noise measured when fake Xe signals for each isotope are simultaneously applied

to the magnetometer. We see the presence of distinct $1/f$ noise. We prove that this drift stems from ϵ_z by making an in situ independent measurement of ϵ_z and then subtracting its drift from each isotope's demodulation phase. In this way, ϵ_z noise is "eaten" via feed forward. We measure ϵ_z in real time by measuring the magnetometer's phase of response to an ancillary rotating $B_\perp$. The variation of this phase measurement is then added or subtracted (depending on the sign of each isotope's γ) to the demodulation phase of each isotope. The influence of this feed foward is also shown in Fig. 4.12. Feed forward reduces the $1/f$ noise on the fake Xe phase measurement down to the white SNR limit. There are some spurious peaks which appear on the demodulated Xe phase when feed forward is activated. These peaks stem from interference between the frequency modulated fake Xe signals and the constant frequency of the ancillary $B_\perp$. Presumably these peaks could be avoided by applying $B_\perp$ as an α-periodic waveform such that any nearby sidebands from the Xe precession would always be more than 1 Hz away. The standard Allan deviation of the rotation computed using the measured fake Xe phases with and without ϵ_z feed forward are shown in Fig. 4.12. With feed forward activated the detection noise supports an ARW of $\sqrt{2}$ 10 μHz/$\sqrt{\text{Hz}}$.

We note that, as was shown in Ch. 2, δ itself depends on ϵ_z (see Eq. 2.12). This is what causes the derivative of ϵ_z to appear on the measured Larmor resonance frequencies. So although utilizing feed forward to suppress ϵ_z's influence on the detected phase noise of a fake Xe signal is clearly helpful, the same is not necessarily true for detecting real Xe signals. In the comagnetometry section below we demonstrate how proper treatment of ϵ_z enables order of magnitude improvement in the field suppression of the computed rotation. Feed forward is not used in any other data presented in this chapter unless specifically stated otherwise.

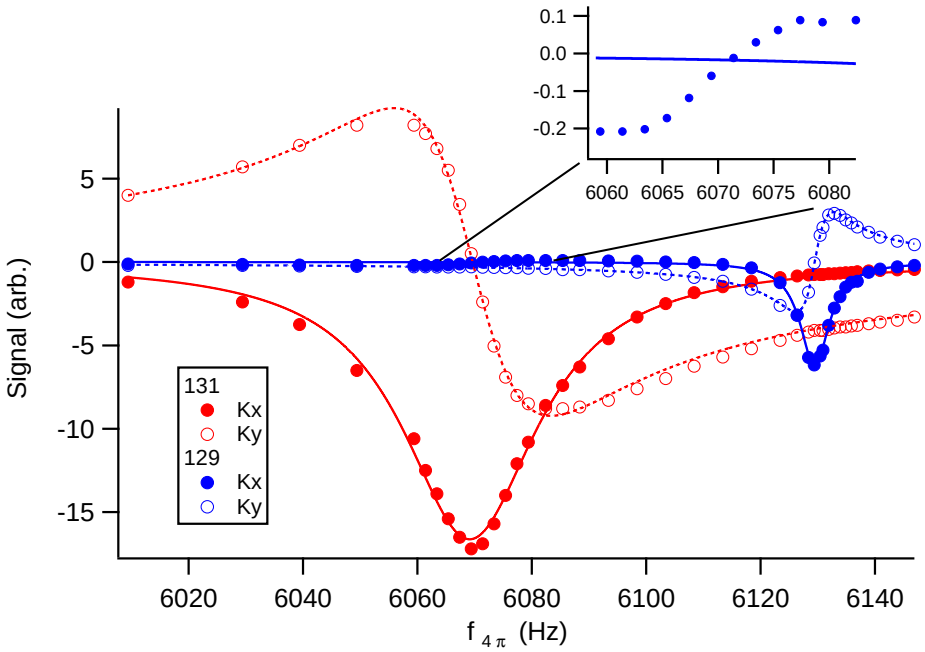

Figure 4.13: PDM excitation cross talk measurement. The in-phase (K_x) and quadrature (K_y) of each isotope's detection channel vs $f_{4\pi}$. The dashed (solid) lines are Lorentzian fits to K_y (K_x). Inset depicts zoom-in on K_x^a when isotope b is near resonance and isotope a is far from resonance.

Cross Talk

Figure 4.13 depicts the cross talk measured for PDM excitation with the gating detection system optimized. These data were acquired using the same procedure described in Ch. 3.3. When isotope b is near resonance and isotope a is far from resonance, we see the quadrature component of isotope b appear on the K_x^a detection channel (see inset). The quadrature of isotope a does not appear on the K_x^b detection channel. The data are consistent with $\beta = 0.016$ and $\beta' < 0.002$ (see Eq. 3.9), which are found by dividing the peak to peak value of the cross talk signal divided by the peak to peak value of the original quadrature signal. Only an upper bound can be placed on β' as the cross talk signal is unresolved.

We believe that finite suppression of gain modulation can contribute to cross talk. For

instance, the input to isotope b's LPF is (see Eq. 4.4),

$$I^b = [A^a_\perp \sin(\alpha^a + \delta^a) + A^b_\perp \sin(\alpha^b + \delta^b)] \cos(\alpha^b_0) \frac{d\alpha^b_0}{dt}, \tag{4.10}$$

where we have assumed that $\epsilon_z = 0$ for the purpose of this discussion. We can rewrite this expression above in terms of a sum of sines such that

$$I^b = \frac{1}{2} \frac{d\alpha^b_0}{dt} [A^a_\perp [\sin(\alpha^b_0 + \alpha^a + \delta^a) + \sin(\alpha^b_0 - \alpha^a - \delta^a)] \tag{4.11}$$

$$+A^b_\perp [\sin(\alpha^b_0 + \alpha^b + \delta^b) + \sin(\alpha^b_0 - \alpha^b - \delta^b)]] \tag{4.12}$$

where $\alpha^b_0 \pm \alpha^a = (\gamma^b_0 \pm \gamma^a) \int dt B_z(t)$ and $\alpha^b_0 \pm \alpha^b = (\gamma^b_0 \pm \gamma^b) \int dt B_z(t)$. Insofar as $\gamma^b_0 = \gamma^b$ we find

$$I^b = \frac{1}{2} \frac{d\alpha^b_0}{dt} [A^a_\perp [\sin(\gamma^- \mathbf{B} + \delta^a) + \sin(\gamma^+ \mathbf{B} - \delta^a)] \tag{4.13}$$

$$A^b_\perp [\sin(2\gamma^b \mathbf{B} + \delta^b) + \sin(-\delta^b)]] \tag{4.14}$$

where $\gamma^\pm = \gamma^b \pm \gamma^a$ and $\mathbf{B} = \int dt B_z(t)$. Recall that $B_z(t) = B_0 + B_1 \cos(\omega_1 t) + B_2 \cos(\omega_2 t)$. Insofar as the $A_\perp$'s are DC, low pass filtering I^b will result in a signal only proportional to δ^b. However, gain modulation causes the $A_\perp$'s to oscillate at integer multiples of ω_1 and ω_2 such that I^b acquires a DC component proportional to δ^a. This model suggests that increasing the gain modulation should make the cross talk more obvious. We have yet to demonstrate that such is the case.

Feedback

In Ch. 2 we learned how the Larmor resonance frequencies of each isotope can be measured in real time by correcting ω_d using the measured phase of precession ($\delta \pm \epsilon_z$). We streamed the demodulated signals (K_x and K_y) of each isotope from the FPGA to a computer at a

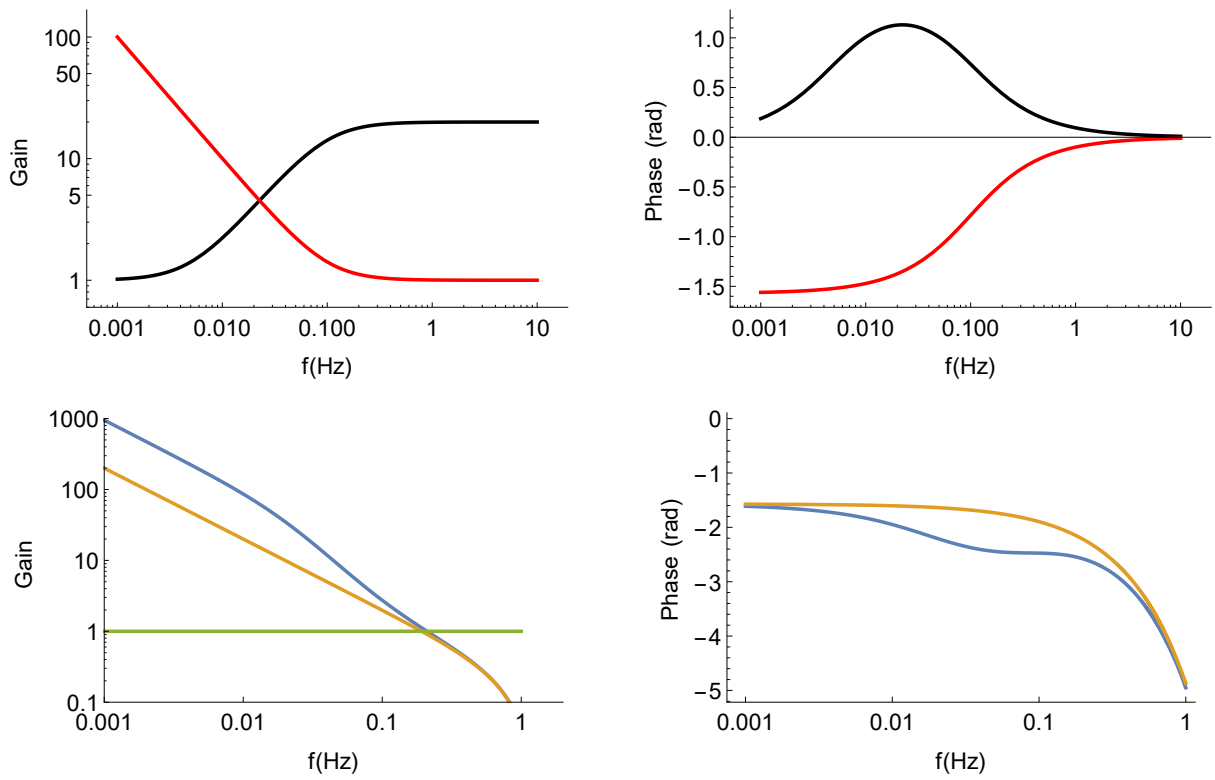

Figure 4.14: Top: Simulated Bode plots of inverted-zero (red trace, $\omega_0 = 0.1$ Hz and $P = 1$) and lead compensator (black trace, $\omega_1 = 0.1$ Hz, and $a = 20.$). Bottom: Simulated Bode plots of $L(s)$ with (blue trace, $\omega_0 = \omega_1 = 2$ Hz, $a = 20$, and $P = 0.01$) and without (orange trace, $\omega_0 = 0.021$ Hz, $P = 0.2$) lead compensator. Both traces assume $\Gamma_2 = 21$ mHz.

rate of 200 samples per second per channel. We then compute the phase of precession of each isotope by calculating $\text{atan}(K_y/K_x)$. The calculated phase of each isotope was then sent through a digital filter whose transfer function (in Laplace space, $s = i\omega$) is

$$K(s) = P(1 + s_0/s)\left(\frac{1 + as/s_1}{1 + s/s_1}\right). \tag{4.15}$$

The first portion in parentheses of this control law is known as an inverted-zero and the second is a lead compensator. Figure 4.14 depicts the magnitude and phase vs. frequency for each of these individual gain stages. In order for a control loop to be stable, the round-trip gain $L(s) = G(s)K(s)$, where $G(s)$ is the open loop gain, must have the following properties [Bechhoefer (2005)]: (i) high gain at low frequency, (ii) low gain at high frequencies,

(iii) phase lag smaller than 180 deg for frequencies where the gain is greater than 1, (iv) gain trend as $1/i\omega$ at the frequency of unity gain. If $G(s)$ were simply the Xe transfer function then the inverted-zero gain stage would suffice. At high frequencies however, the phase shifts from the second order Butterworth and moving average filters utilized in the α-space demodulation dominate. These phase shifts are partially compensated for by the lead compensator, allowing us to increase the gain of the control law before oscillations ensue. The open loop Xe transfer function is

$$G(s) = \left(\frac{1}{s+\Gamma_2^K}\right)\left(\frac{1}{(s/s_a)^2/ + \sqrt{2}s/s_a + 1}\right)\left(e^{-s\pi N/f_s}\mathrm{sinc}(-s\pi N/f_s)\right), \qquad (4.16)$$

where the first portion in parenthesis is due to the Xe, the second is due to the second-order Butterworth LPF (s_a is the filter corner), and the third is due to the moving average (N number of samples, f_s sample rate). Figure 4.14 depicts the magnitude and phase of $L(s)$ vs. frequency. In order to satisfy criterion (iv) without the lead compensator, we must set $\omega_0 = \Gamma_2$. The gain P is then increased until the Gain=1 at the frequency where the phase=-π. Adding the lead compensator allows us to let $\omega_0 >> \Gamma_2$ without violating criterion (iv) so long as $\omega_1 \sim \omega_0$. We see that adding the lead compensator enables a factor of 5 increase in gain from 1 to 100 mHz. We find that the results from this simulation are in agreement with experiments. We note in passing that the control law implemented here is a specialized type of proportional-integral-derivative gain, where the proportional and integral gain are related to one another (inverted-zero) and the derivative gain is truncated (in contrast to purely derivative gain which increase with f monotonically).

The servoed error signals ($\delta\omega_d^K$) are used to adjust the drive frequency of each isotope. We chose to implement the software such that we calculate $\omega_1 = \omega_d^b + \delta\omega_d^b$ and $\omega_2 = \omega_d^a + \delta\omega_d^a - 3(\omega_d^b + \delta\omega_d^b)$. Figure 4.15 depicts the measured phase noise of each isotope when feedback is activated. Feedback suppresses the low frequency phase noise of each isotope. Residual low frequency phase noise persists despite feedback, suggesting that compensation

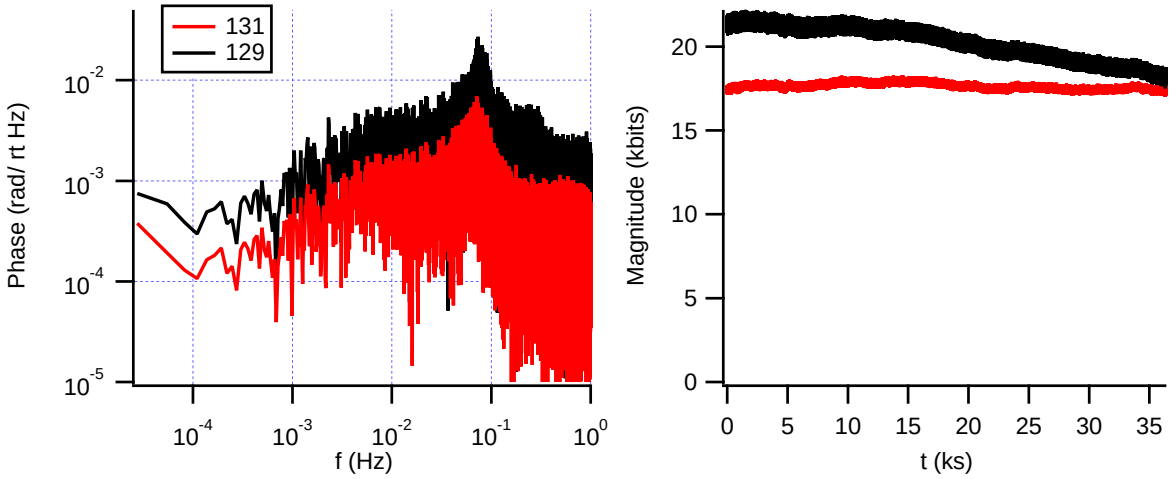

Figure 4.15: Influence of feedback on Xe phase and amplitude. Left: measured phase noise of each isotope with feedback engaged. Right: magnitude of detected Xe signals vs time. The feedback for this data did not include the lead compensator.

for finite gain (as discussed in Ch. 2) may be necessary. We also found that the amplitudes of each isotope, especially isotope a, drift over hour length time scales when feedback is engaged (also shown in Fig. 4.15). The rate of drift was found to be proportional to the gain at high frequency (with the lead compensator installed isotope a's amplitude would drop to zero after 10 ks), and variable from data set to data set. If the servo is dis-engaged, the amplitudes largely return to their original state suggesting that the demodulation phase α_0^a has an error which accumulates over time.

We believe that this drift stems from rounding errors which occur when the servoed error signals, which are double precision (DBL) numbers, are rounded to 64 bit integers and then sent to the FPGA. In App. B we show that the integer increment Δn of a counter composed of X bits whose update rate is f_{up} produces a periodic waveform of frequency f_0 according to $\Delta n = f_0\beta$ where $\beta = 2^X/f_{up}$. The increment for θ_1's phase register is $\Delta n_1 = \Delta n_1^0 + \beta\text{Round}[G(\delta^b + \epsilon_z)]$ where Δn_1^0 is the drive frequency determined under open loop conditions. The Round notation denotes rounding. The increment for θ_2's phase register is $\Delta n_2 = \Delta n_2^0 + \beta\text{Round}[G(\delta^a - \epsilon_z) - 3G(\delta^b + \epsilon_z)]$. Recall $\alpha^a = 3\theta_1 + \theta_2 + \int dt B_m$. We can

rewrite the first two terms as

$$3\theta_1 + \theta_2 \sim \int (3\Delta n_1 + \Delta n_2)dt = 3\Delta n_1^0 + \Delta n_2^0 + 3\beta\text{Round}[G(\delta^b + \epsilon_z)] + \beta\text{Round}[G(\delta^a - \epsilon_z) - 3G(\delta^b + \epsilon_z)]]. \quad (4.17)$$

We see that if the Round functions were discarded then the terms with $\delta^b + \epsilon_z$ cancel. The rounding allows for isotope b's correction frequency to influence α_0^a! This model explains why isotope a's magnitude drifts substantially more than isotope b's magnitude. Possible solutions are to change the θ_1 and θ_2 phase registers to ϕ^a and ϕ^b registers so that the subtraction of two rounded numbers is avoided. Alternatively, one can change driving schemes such that $\omega_1 = \omega_d^b$ and $\omega_2 = \omega_d^a$ (drive scheme B mentioned previously, see Ch. 4.5 for preliminary results). The rest of the data presented in this chapter suffers from this rounding issue unless otherwise noted.

4.4 Comagnetometry

With frequency feedback implemented so that we can measure each isotope's Larmor resonance frequency continuously and in real time we are prepared to evaluate the degree to which magnetic fields produce correlations between the two measured resonance frequencies. Each isotope is phase locked to line center with an accuracy of ± 0.3 mHz. The drive frequency of each isotope then tracks the resonance as defined by the phase of precession as measured by the Rb.

Stability

Figure 4.16 depicts the measured resonance frequencies plotted on separate linear scales over 10 hours of continuous measurement. We see that the two resonance frequencies are highly

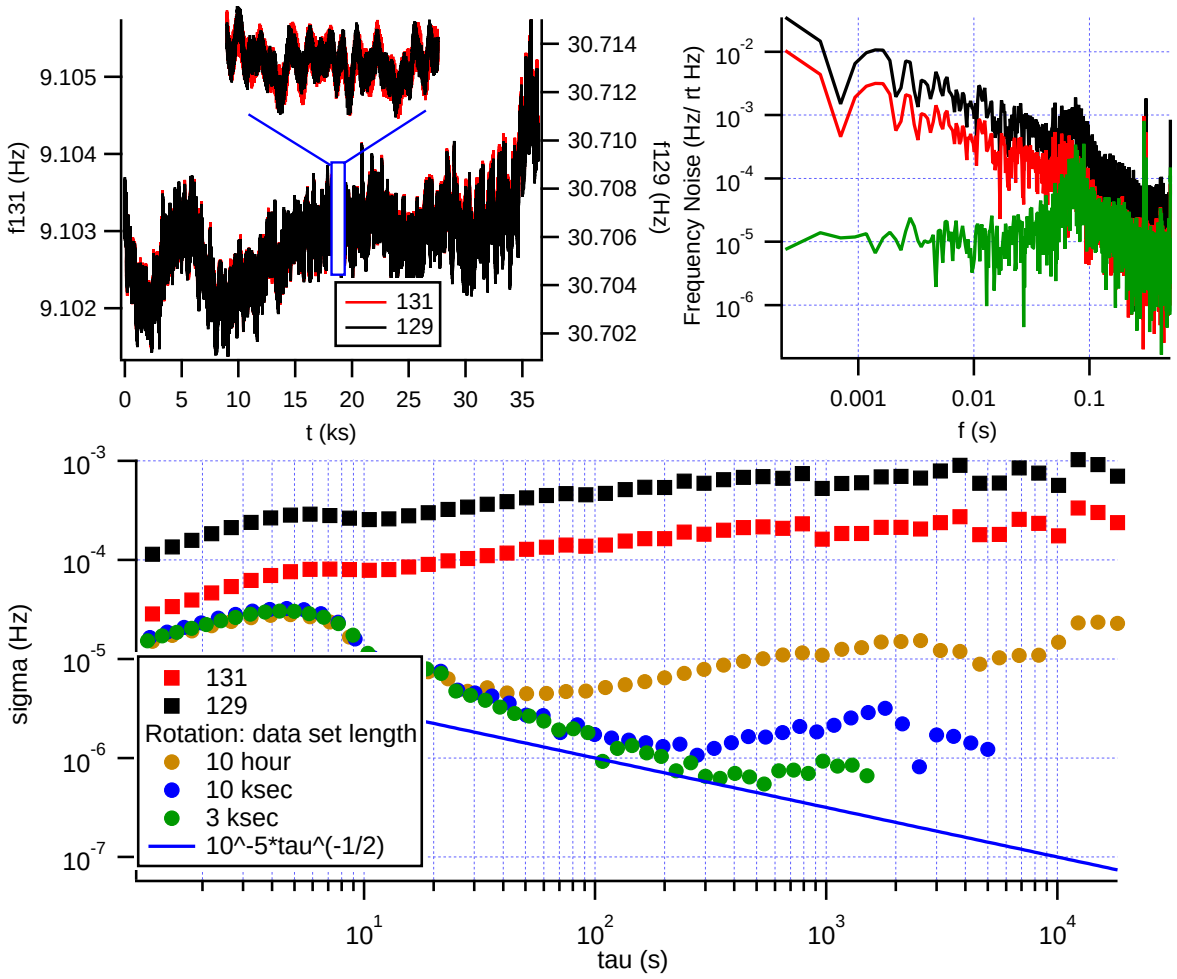

Figure 4.16: PDM comagnetometer noise. Top left: measured Larmor resonance frequencies for each isotope plotted on separate linear scales vs time. The inset depicts 200 sec of the same data. Top right: power spectrum of first 3 ks of data. The green trace depicts the calculated ω^R. Bottom: standard Allan deviation of measured Larmor resonance frequencies and computed ω^R using the first 3 ks, 10 ks, and entire data set.

correlated over short (see 200 sec inset) and long time scales. The amplitude spectral density of the resonance frequencies show clear $1/f$ noise which is approximately ρ larger for isotope a than isotope b suggesting the noise is of magnetic origin. We calculate the rotation using $(1+\rho)\,\omega^R = \rho\omega^b - \omega^a$ where $\rho = \bar{\omega^a}/\bar{\omega}^b = 3.37322$, and the bar denotes averaging over the length of the data set. We note that this data was not corrected for finite gain. We found that correcting for finite gain only influenced the field suppression when an ancillary B_z was applied. The expected ρ from the literature is $\rho_0 = 3.373417(38)$ [Makulski (2015)]. If we assume that isotope b is responsible for the entirety of this discrepancy (due to quadrupole frequency shifts due to electric field gradients on the cell walls for instance) then we write,

$$\rho = \frac{\rho_0\omega^b}{\omega^b + \delta\omega^b} \rightarrow \delta\omega^b = \frac{\rho_0 - \rho}{\rho}\omega_b \sim 0.5\,\text{mHz}. \tag{4.18}$$

The amplitude spectral density of ω^R exhibits white noise of frequency from 0.1 to 20 mHz. From 20 to 80 mHz the noise goes as f (white phase noise). Both the white frequency noise and white phase noise are due to finite SNR of the comagnetometer. The white phase noise does not continue for frequencies greater than 80 mHz because of the LPF used in conjunction with α-space demodulation (see discussion above).

The standard Allan deviations of the time series of measured Larmor resonance and computed ω^R are also depicted in Fig. 4.16. We see that each isotope trends as $\tau^{1/2}$ indicative of $1/f$ magnetic noise. We find that the Allan deviation of ω^R (σ_R) depends on the amount of data (length of time) used for its computation. If we compute σ_R for the first 3 ks, the σ_R trends as τ^{-1} from 10 to 100 s due to white phase noise and then trends as $\tau^{-1/2}$ from 100 to 600 s suggesting an effective SNR of $\sim 1500\ \sqrt{Hz}$. The confidence in the final data points is insufficient to know whether the increase in σ_R at 1 ks is an artifact of finite sample number or bias instability. In subsequent data sets (not shown here but see [Thrasher et al. (2019)]) we improved the ARW by a factor of two by changing from 4π pulses to 2π pulses (see discussion concerning Fig. 4.10). The measured SNRs were 3200 and 5300 $\sqrt{\text{Hz}}$ for

isotopes a and b respectively. The SNR of isotope b is very similar to the measured DNR of the PDM (see Fig. 4.4). Because of our drive scheme we expect $SNR^b \sim \rho\, SNR^a$. The fact that we observe $SNR^b < 2\, SNR^a$ suggests that SNR^b is limited by the PDM DNR.

Continuing our discussion of Fig. 4.16, if we compute σ_R for the first 10 ks of data, the $\tau^{-1/2}$ trend is never resolved due to a $\tau^{1/2}$ trend. The dominance of the $\tau^{1/2}$ trend increases when we compute σ_R using the full 10 hr data set. These observations lead us to believe that there exists a systematic frequency drift in the measured phase of one of the isotopes, the influence of which on σ_R increases with time. This data belongs to the same data set as was used to produce Fig. 4.14. We believe that the drift of the measured magnitude of isotope a is likely related to the influence of data set length on σ_R. The minimum σ_R calculated over 3 ks is 550 nHz. Although we have two other data sets whose bias instability was ~ 300 nHz, we found that measuring a bias instability < 1 μHz was difficult to repeat. In the following sections we discuss measurements we made to better understand what noise sources may limit the bias instability.

Study of systematics

In this section we summarize our exploration of how various experimental parameters influence ω^R. For experimental convenience we often make a change to some experimental parameter X and then watch how ρ responds over time. Plotting ρ vs. X we find $\partial\rho/\partial X$. By measuring the fluctuations of X we can then estimate the noise of ρ as

$$\delta\rho = \frac{\partial\rho}{\partial X}\delta X. \tag{4.19}$$

The noise of ρ is then cast in terms of rotation as

$$\delta\omega^R = \delta\rho\frac{\omega_0^b}{1+\rho}, \tag{4.20}$$

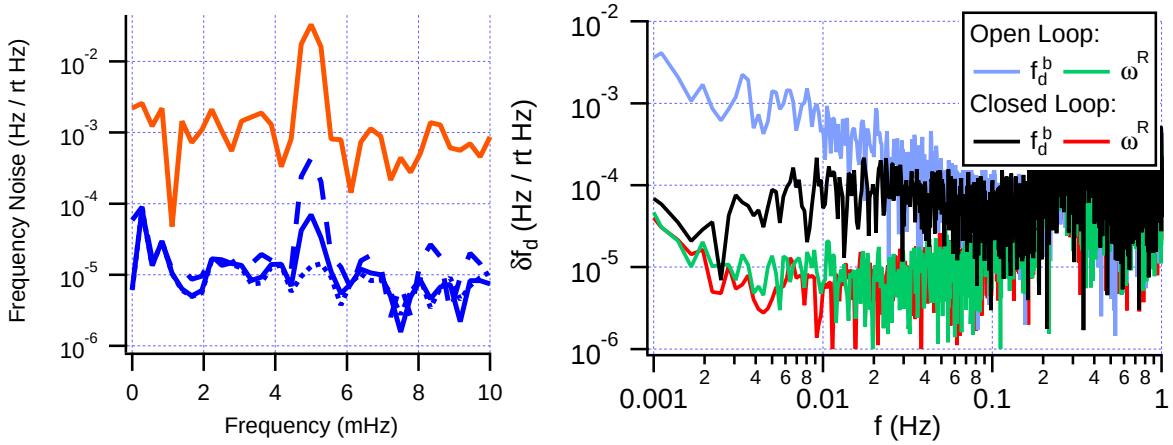

Figure 4.17: Left: amplitude spectral density of isotope b's Larmor resonance frequency (orange) and computed rotation (blue) with an ancillary 5 mHz AC B_z applied. Large dashed line depicts no ϵ_z correction. Solid line depicts ϵ_z correction with $B_w = 3.4$ mG. Small dashed line depicts ϵ_z correction with $B_w = 2$ mG. Right: influence of real-time bias field stabilization using the sum of the two Larmor resonance frequencies on ω_d^b and ω^R.

where ω_0^b is the average resonance frequency of isotope b.

Field Suppression: Since the goal of a comagnetometer is to sense non-magnetic spin-dependent interactions, we characterize how well the device rejects bias magnetic field perturbations. Finite magnetic field suppression will lead to bias instability if the magnetic drift is severe enough. In order to characterize the field suppression factor (FSF) of the comagnetometer, we record the drive frequencies while applying an ancillary 5 mHz 4.3 μG B_z. We define the FSF to be $\tilde{\omega}_d^b/\tilde{\omega}^R$ at the frequency of the ancillary B_z. We define the FSF in this way because if one only had a single isotope with which to sense non-magnetic phenomena one would naturally choose the isotope with the smallest γ, which in our case is isotope b. Hence, the frequency stability of isotope b is used as a metric for the frequency stability of the computed rotation. The drive frequencies used for computations mentioned below were corrected for finite gain (as discusses in Ch. 2) in post processing.

Recall from Ch. 2 that the computation of ω^R does not cancel all of the magnetic field dependence of the measured Larmor resonance frequencies due to the influence of ϵ_z which

is proportional to B_z. As such, we expect that ignoring the influence of ϵ_z will degrade the FSF. If we ignore ϵ_z we measure an FSF of 75 (see Fig. 4.17). We can correct for ϵ_z by subtracting the time derivative of B_z fluctuations normalized by B_w and measured in-situ by the sum of the Xe isotope's Larmor resonance frequencies. We write,

$$\omega_c^R = \frac{\rho\tilde{X}_z^b - \tilde{X}_z^a}{1+\rho} + i\omega\tilde{\epsilon}_z - i\omega\tan^{-1}\left(\frac{1}{B_w}\frac{\tilde{\omega}_d^a + \tilde{\omega}_d^b}{\gamma^a + \gamma^b}\right) \tag{4.21}$$

Computing ω^R in this way requires knowledge of B_w. If we compute ω^R using the average of the two independent measurements of B_w mentioned previously in this chapter ($B_w = 3.4$ mG) we find an FSF of 470. However, the maximum value of FSF occurs for $B_w = 2.0$ mG and is 2300. Clearly, ϵ_z introduces substantial phase shifts to the comagnetometer signal. This is not surprising when one considers that it is the derivative of ϵ_z that is added to ω^R. Since the ancillary B_z modulation is sinusoidal, ϵ_z contributes a 90 deg phase shifted oscillation at the same frequency to ω^R.

In order to prevent uncertainty in B_w from influencing the FSF, we built an additional feedback loop which corrected B_{z0} such that the sum $\omega_d^a + \omega_d^b$ was kept fixed. Assuming that B_{z0} is the dominant contribution to ϵ_z, this will stabilize the magnetometer phase shift. The gain of this feedback loop was sufficient to suppress $\tilde{\omega}_d^b$ by a factor of 15 at 5 mHz compared to when the sum $\omega_d^a + \omega_d^b$ was not stabilized, as shown in Fig. 4.17. The FSF was 1800 (not shown) with this additional feedback loop (taking into account the factor of 15 suppression of $\tilde{\omega}_d^b$). Similar to finite gain corrections, stabilizing the bias field using the sum frequency did not improve the noise or stability of the computed rotation. This is strong evidence that finite FSF is not responsible for the bias instability we observe.

We can estimate what the bias instability would be if it were limited by the FSF by finding the τ at which the σ_0 due to ARW equals the σ_{-2} due to suppressed $1/f$ magnetic noise. Figure 4.16 shows that $\sigma_0 = 10^{-5}\text{Hz}/\sqrt{\text{Hz}}\tau^{-1/2}$. The scaled sum frequency amplitude spectral density (not shown) exhibits clear $1/f$ dependence with a slope of $\sqrt{A_{-2}} = 10$ nG Hz$/\sqrt{\text{Hz}}$.

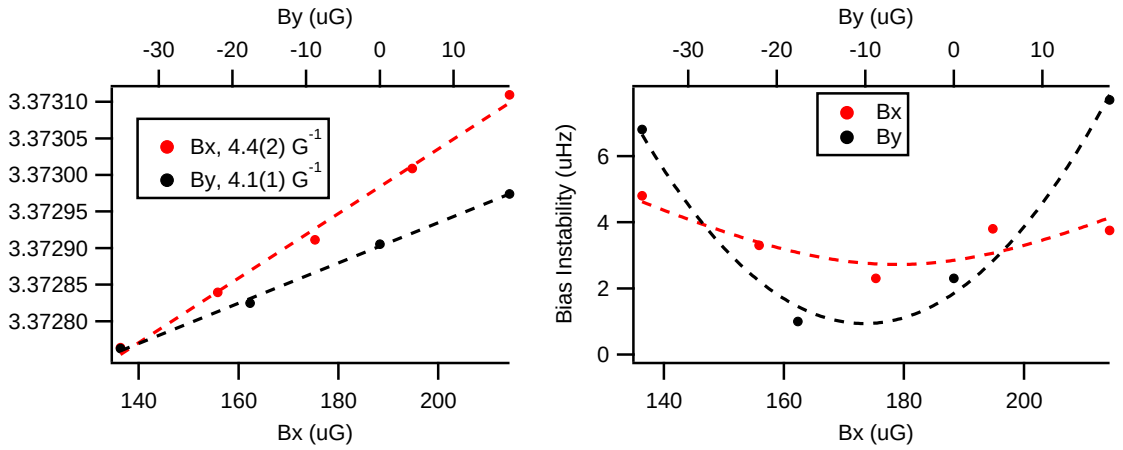

Figure 4.18: Left: Influence of B_x and B_y on the average measured ρ. Dashed lines are linear fits to the data. The slope from the fits are listed in the legend. Right: Influence of B_x and B_y on the bias instability of ω^R. Dashed lines are quadratic fits to the data. B_x was scanned first for this data set.

Hence, the expected $1/f$ magnetic noise contribution to rotation is $\sqrt{h_{-2}} = \gamma^b\sqrt{A_{-2}}/\text{FSF}$. The standard Allan deviation's dependence on h_{-2} is $\sigma^2_{-2} = \pi^2 h_{-2}\tau 2/3$ [Vanier and Audoin (1989)]. Setting $\sigma_0 = \sigma_{-2}$ with FSF = 1800 we find $\tau = 2$ ks. Hence, the FSF-limited bias instability is estimated to be ~ 200 nHz.

Transverse Fields: Here we describe how changing the DC transverse fields (B_x and B_y) influences the comagnetometer. The first experiment we performed was to measure the Allan deviation for various ancillary B_x and B_y fields. Figure 4.18 shows the resulting data. We find that the average ρ depends linearly on B_x and B_y. We also find that the bias instability of ω^R is quadratically sensitive to both B_x and B_y. The bias instability is more sensitive to B_y then B_x. The bias instability has a lower minimum when B_y is scanned because B_x was already optimized when B_y was scanned. We have found that if the bias instability is poor then the DC transverse fields are likely sub-optimal.

In Ch. 2 we derived how transverse fields produce noble gas phase shifts (see Eq. 2.19-2.20).

In the high gain limit such that $\delta^K = \mp\epsilon_z$ and to first order in ϵ_z we find

$$\rho = \frac{\gamma^a B_0 - \Gamma_2^a \, \eta^a \left[B_x B_y - \epsilon_z (B_x^2 - B_{y0} B_y)\right]}{\gamma^b B_0 - \Gamma_2^b \, \eta^b \left[B_x B_y - \epsilon_z (B_x^2 - B_{y0} B_y)\right]} \tag{4.22}$$

where $B_0 = \sqrt{B_z^2 + B_x^2 + B_y^2}$ (the Xe precession frequency depends on the magnitude of the magnetic field in the vapor cell), $\eta^K = (j^K \gamma^K / \Gamma_2^K)^2$, and $B_i = B_{i0} + b_S^K S_i$ are time averaged classical and SE fields. This function has the feature that for $\delta^K = \mp\epsilon_z = 0$

$$\left.\frac{\partial \rho}{\partial B_x}\right|_{B_y > 0.1 \ \mu\mathrm{G}} = \left.\frac{\partial \rho}{\partial B_y}\right|_{B_x > 0.1 \ \mu\mathrm{G}}. \tag{4.23}$$

We fit the ρ vs. $B_{x,y}$ data separately using Eq. 4.22 assuming $\epsilon_z = 0$. We also assume that $b_S^K S_x = 175$ μG as this is the same B_x which minimizes the bias instability. Likewise we assume $b_S^K S_x = -10$ μG. We also fix $\gamma^a = 1177.69$ Hz/G, $\Gamma_2^a = 15$ and $\Gamma_2^b = 20$ mHz, and $j^a = j^b = 0.2$ (the data were acquired with pumping scheme B and $b_1 = b_2 = 0.4$). Fitting the ρ vs. B_x data we find $\gamma^b = 349.1598(6)$ Hz/G and $B_y = 15.4(7)$ μG. Fitting the ρ vs B_y data we find $\gamma^b = 349.1664(3)$ Hz/G and $B_x = 14.2(5)$ μG. Apparently the measured behavior of ρ vs $B_{x,y}$ can be accounted for by cancellation of $b_S^K S_{x,y}$ to no better than 15 μG. These realistic fit parameter results suggest that our model may accurately account for ρ's behavior.

Using Eq. 4.20 and our measured slope $\partial\rho/\partial B_{x,y} = 4$ G^{-1} we find $\partial\omega^R/\partial B_{x,y} = 9$ Hz/G. If we assume that the $1/f$ noise of $B_{x,y}$ is the same as B_z (10 nG Hz/$\sqrt{\mathrm{Hz}}$) then we expect $\sigma_{\omega^R} = 233$ nHz $\sqrt{\mathrm{Hz}}\sqrt{\tau}$, which at 100 s equals ~ 2 μHz. This is very similar to the bias instability we most often observe after carefully optimizing B_x and B_y. It is unclear why we are unable to optimize the transverse fields such that $B_{x,y} < 10$ μG (as suggested from our data fit above) and therefore further reduce $\partial\omega^R/\partial B_{x,y}$. One possible explanation is (again) the drift of the transverse fields. The standard Allan deviation of the transverse fields (again assuming that the $1/f$ noise is the same as the measured B_z $1/f$ noise) is $\sigma_{B_z} = 25$ nG

$\sqrt{\text{Hz}}\sqrt{\tau}$. Hence, if at $t = 0$ we set $B_{x,y} = 0$ the drift of the transverse fields would cause $\sigma_{B_{x,y}} \sim 1$ μG after 100 s.

It is interesting to consider how transverse fields influence ω^R. Assuming the isotopes are frequency locked on resonance and only experience frequency shifts due to classical magnetic fields we write

$$\omega^R = \frac{B_x B_y}{1+\rho}(\rho\Gamma_2^b\eta^b - \Gamma_2^a\eta^a). \tag{4.24}$$

We normally choose the modulation depths such that $j^b \sim \rho j^a$. Under such conditions we find $\rho\Gamma_2^b\eta^b - \Gamma_2^a\eta^a = (j^a\gamma^a)^2[\rho/\Gamma^b - 1/\Gamma^a] \sim 10^7$ G^{-2}. One could consider instead choosing the modulation depths such that $\rho\Gamma_2^b\eta^b - \Gamma_2^a\eta^a = 0 \rightarrow j^b/j^a = \sqrt{\rho\,\Gamma^a/\Gamma^b} \sim 1.6$. In this way the sensitivity of ω^R to B_x and B_y should be suppressed.

Pump Laser Detuning: The SE field $b_S^K S_\perp$ depends on the alkali pumping rate R which itself depends on the pump laser detunings. Since we have seen that transverse fields influence ω^R it behooves us to study how pump laser detuning influences ω^R as well. The pump detunings also influence the AC Stark effect as well as ϵ_z (since $\epsilon_z = S_y/S_x, S_x \sim R$). Similar to the temperature studies mentioned above, we measured ρ vs. time after we made discrete changes to the pump detuning(s). Figure 4.19 depicts the average ρ for each pump detuning. These data were acquired without bias field stabilization, correction for finite gain, or correction for ϵ_z. We find that ρ depends linearly on each pump laser's detuning such that (see Eq. 4.20) $\partial\omega^R/\partial\Delta_{pump} \sim 77$ μHz/GHz for pump A and 43 μHz/GHz for pump B.

We measure the pump laser detuning noise using the transmission through our hot vapor cell at zero field. We record the amplitude fluctuations of the light transmitted through the vapor cell and convert to detuning noise by measuring $\partial I_{PD}/\partial\Delta_{pump}$ where I_{PD} is the photo current detected by a single photodiode. Figure 4.19 depicts the standard Allan deviation of each pump laser's detuning noise scaled to rotation frequency using the respective $\partial\omega^R/\partial\Delta_{pump}$. We see that the implied rotation noise from pump A is 800 nHz at

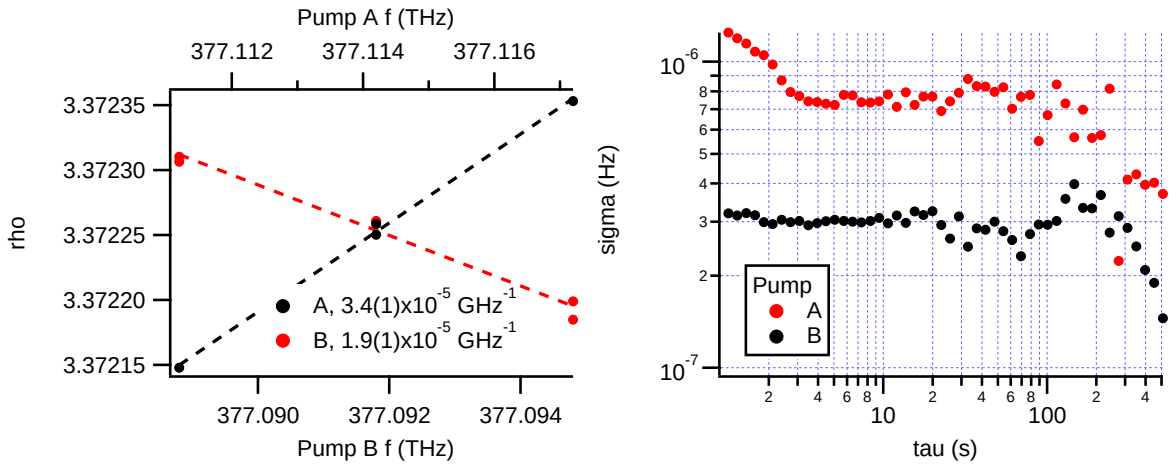

Figure 4.19: Left:ρ vs. pump detuning. Filled circles are measured data. Dashed lines are linear fits to the data. The slope of each fit is listed in the legend. The D_1 resonance is 377105.2 GHz in our vapor cell. Right: standard Allan deviation of pump detuning noise scaled to rotation frequency.

100 s of integration, very near to the observed rotation noise of $\sim$ 1 μHz. Pump B's implied rotation noise is $3x$ less than pump A's rotation noise. This is likely due, at least in part, to the fact that pump A is normally operated at a smaller detuning than pump B in order to cancel the average AC stark. This data suggests stabilizing one or both pump detunings may improve the rotation frequency bias instability. Stabilizing the pump laser detuning at a detuning of $\sim$ 10 GHz is difficult using standard atomic spectroscopy techniques such as a dichroic atomic vapor laser lock. An alternative would be to make corrections to the pump detuning to keep the magnetometer response to an ancillary rotating $B_\perp$ constant. This has not yet been attempted.

Temperature: Cell temperature can influence the measured Larmor resonance frequencies in several ways. If the Xe is not driven exactly on resonance then the temperature dependence of Γ_2^a is expected to be larger than the temperature dependence of Γ_2^b due to an anomalous temperature dependent wall relaxation mechanism. Another possibility is through $\epsilon_z = S_y/S_x$ as S_x will exhibit temperature dependence in an optically thick (photon starved) vapor cell. A third possibility is quadrupole frequency shifts of isotope b having a

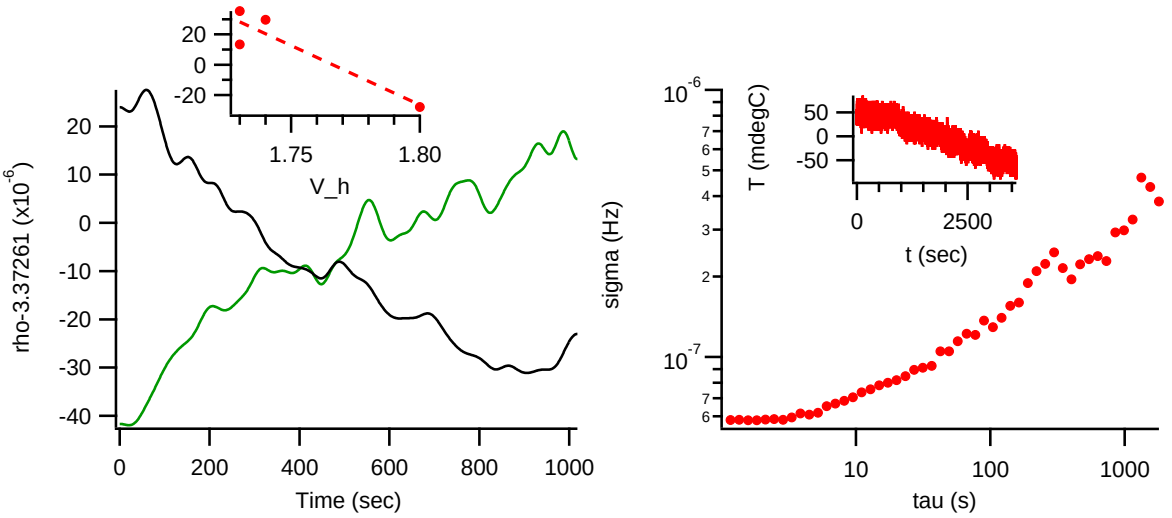

Figure 4.20: Temperature dependence of ρ. Left: ρ vs time where the heater voltage is changed in step like fashion at $t = 0$. Inset shows steady state ρ vs V_h with a linear fit (dashed line). Right: standard Allan deviation of cell temperature as measured by the RTD and converted to rotation frequency under normal operating conditions. Inset shows the time series of the cell temperature as measured by the RTD.

temperature dependence.

We tested how cell temperature fluctuations relate to rotation instability by recording the Larmor resonance frequencies of each isotope as the power (via heater voltage V_h) to the cell heaters is changed. Figure 4.20 shows $\rho = \omega^a/\omega^b$ (not corrected for finite gain) vs time. At $t = 0$ the power to the cell heaters is changed in step like fashion. The several hundred second response time of the cell temperature to the change in heater power is clearly visible in ρ. We measure $\partial\rho/\partial V_h = 8(2) \times 10^{-4}$ 1/V. We can convert this rate to $\partial\rho/\partial T$ as follows

$$\frac{\partial\rho}{\partial T} = \frac{\partial\rho}{\partial V_h}\frac{\partial V_h}{\partial n}\frac{\partial n}{\partial T}, \tag{4.25}$$

where $\partial V_h/\partial n$ comes from spectroscopic measurements of n (Rb density) at various V_h and $\partial n/\partial T$ comes from the Rb vapor pressure curve. We find that $\partial\rho/\partial T = 8 \times 10^{-6}$ degC^{-1}. Using Eq. 4.20 with $\rho = 3.3734$ and $\omega_0^b = 10$ Hz we find $\partial\omega^R/\partial T = 18$ μHz/degC. We measured the cell temperature fluctuations using the RTD in contact with the vapor

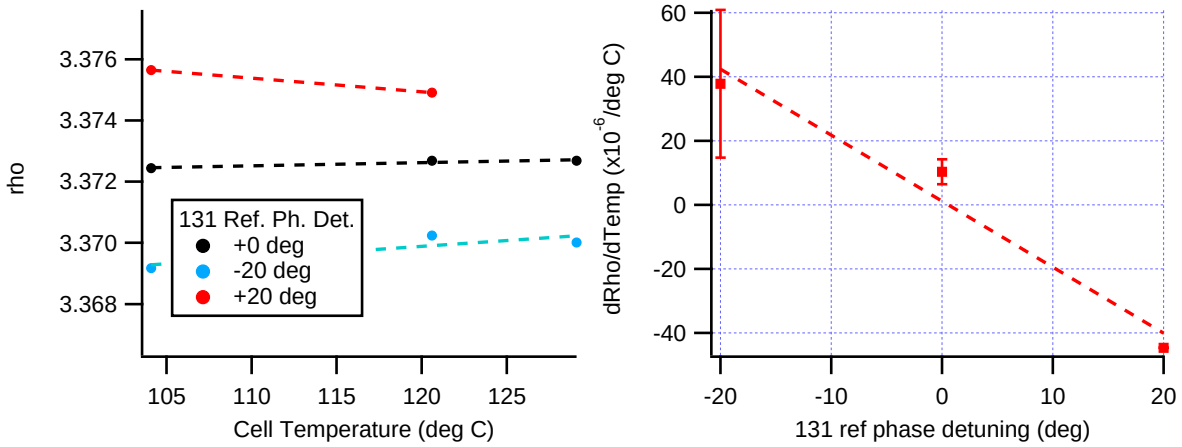

Figure 4.21: Left: ρ vs. cell temperature for three different detunings. Dahsed lines are linear fits to each data set. Right: measured $\partial\rho/\partial T$ (slopes from data on the left) vs. δ^b. Dashed line is linear fit to the data.

cell. Figure 4.20 depicts the cell temperature vs. time derived from the measured RTD's resistance. The standard Allan deviation of the measured temperature fluctutions scaled by $\partial\omega^R/\partial T$ is also shown. At 100 s, σ is only 200 nHz suggesting that the temperature stability of this particular data set fails to account for the 1 μHz bias we normally encounter after 100 s of integration. One possible issue with this logic is that $\partial\omega^R/\partial T$ is likely frequency dependent. We have assumed that large temperature changes over short periods of time influence ρ the same amount as small temperature changes over long periods of time, which is likely not the case.

We also studied how δ^b influenced $\partial\rho/\partial T$. We did so by recording the steady state of ρ at various cell temperatures with different δ^b. Figure 4.21 shows $\partial\rho/\partial T$ vs. δ^b_0. Resonance is located at/near δ^b_0=0. We see a linear relation between $\partial\rho/\partial T$ and δ^b_0 which goes through zero when δ^b_0=0. Temperature dependence of quadrupole frequency shifts and/or Γ^b_2 could account for this behavior. We note that the best performance of the NGC gyro was achieved by carefully choosing δ^b such that the temperature dependence of ω^R becomes non-linear [Walker and Larsen (2016)]. We have yet to study how the temperature dependence of ω^R changes with δ^a.

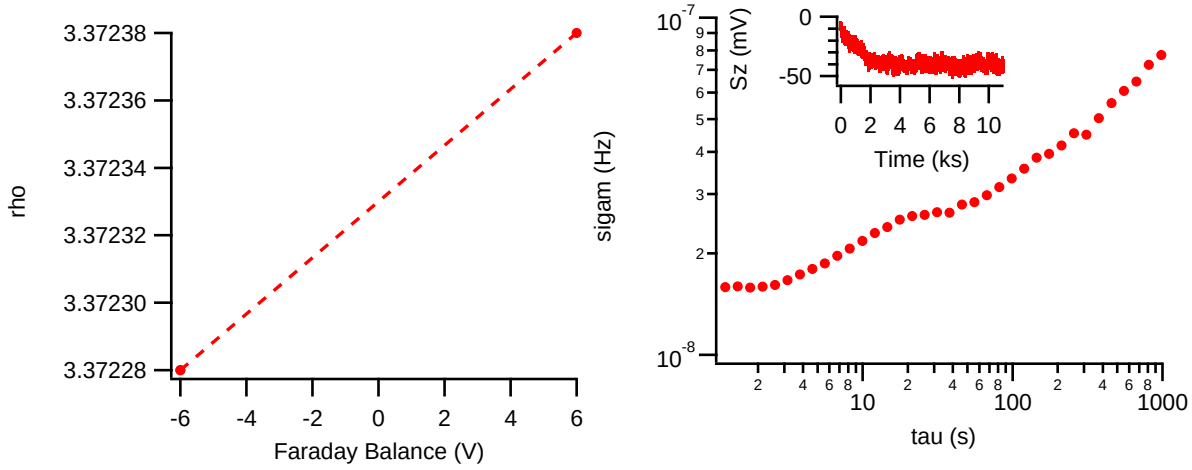

Figure 4.22: Left: ρ vs. V_{diff}. The data are fit with a line (dashed line) of slope $8{\times}10^{-6}$ V^{-1}. Right: standard Allan deviation of photodiode balance scaled to rotation frequency units. Inset depicts time series of V_{diff}.

Other: We also investigated how varying the pulse area and pump beam pointing influenced ρ. Neither made a measurable impact on the steady state value of ρ.

DC voltage into DAQ: We found that the DC voltage digitized by the DAQ influenced the measured ρ. We measured $\partial\rho/\partial V_{diff} = 8 \times 10^{-6}\ V_{diff}^{-1}$(see Fig. 4.22). In order to estimate the noise of V_{diff} we simply recorded V_{diff} overnight while Xe was not excited. The standard Allan deviation of the measured V_{diff} noise scaled to rotation frequency is depicted in Fig. 4.22. We see that at 100 s of integration the rotation frequency noise due to photodiode balance drift is 30 nHz, significantly less than the observed bias instability of 1 μHz. Although the photodiode balance drift does not appear to limit the performance of the comagnetometer we were surprised by its existence. We have determined that ρ's dependence on photodiode balance stems from our implementation of α-space demodulation. Simply put, our demodulation waveforms have non-zero overlap with DC. This can be seen by letting $S_z = S_{z0}$ (the part of S_z at DC such as $1/f$ detection noise) and evaluating Eq. 4.4.

4.5 Ongoing Studies

generalized matrix inverse

We have started using a real time fitting algorithm based on generalized matrix inversion (MI). We make n samples of S_z spaced evenly in time. We compute the value of α at each measurement time. We can write Eq. 4.3 with respect to our multiple measurements as

$$S = \begin{bmatrix} S_1 \\ S_2 \\ \vdots \\ S_n \end{bmatrix} = \begin{pmatrix} \cos(\alpha_1^a), \sin(\alpha_1^a), \cos(\alpha_1^b), \sin(\alpha_1^b), 1 \\ \cos(\alpha_2^a), \sin(\alpha_2^a), \cos(\alpha_2^b), \sin(\alpha_2^b), 1 \\ \vdots \\ \cos(\alpha_n^a), \sin(\alpha_n^a), \cos(\alpha_n^b), \sin(\alpha_n^b), 1 \end{pmatrix} \begin{bmatrix} A^a \sin(\delta^a) \\ A^a \cos(\delta^a) \\ A^b \sin(\delta^b) \\ A^b \cos(\delta^b) \\ S_{z0} \end{bmatrix} = B.V, \qquad (4.26)$$

where we have included the $1/f$ detection noise in the term S_{z0}. We can solve for V using the generalized inverse $V = (B^T B)^{-1} B^T S$, which is guaranteed to exist as $B^T B$ is a square matrix of real values. This scheme is only sensitive to changes in δ which are slow compared to the measurement time of n samples and works best when α makes large (but less than 2π) changes between subsequent samples. In contrast to α-space demodulation, this scheme's measure of δ has no over lap with DC. We implimented the scheme on a computer using LabVIEW. The demonstrated bandwidth is 10 Hz.

In Fig. 4.23 we show a time series of the phase deduced using the old and new (MI) demodulation methods for each isotope. For these data the output of the MI outputs were passed through a ten point moving average filter. The transients are concurrent with changes in the photo diode balance or S_{z0}. We see that, transients aside, the phase deduced using the matrix inverse is independent of S_{z0}. The phase deduced using the old method however acquires an offset proportional to S_{z0}. The measured phase noise of each method, which is dominated by $1/f$ magnetic noise, are in agreement with one another (see Fig. 4.23). Besides

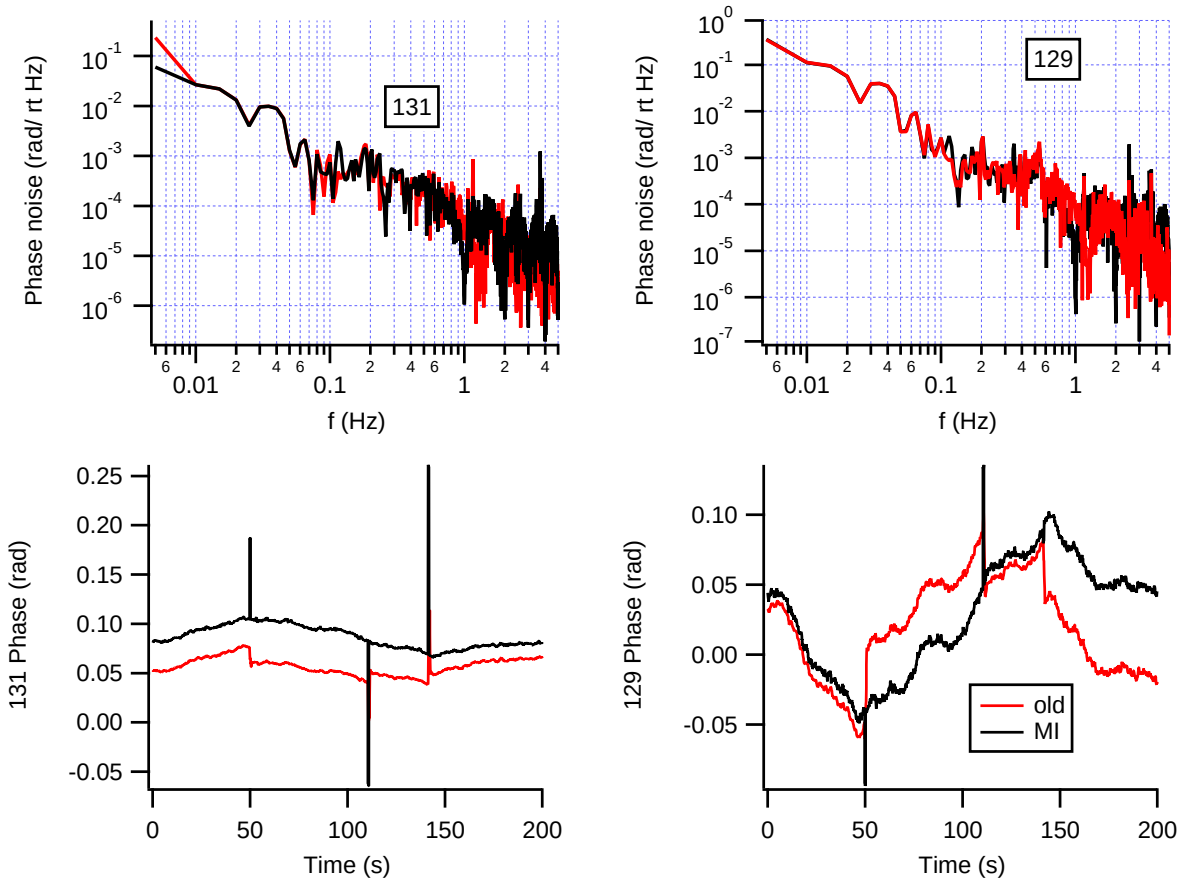

Figure 4.23: Matrix Inverse deduction of Xe phases. Top: amplitude spectral density of isotope b (left) and isotope a (right) using the old (red) and matrix inverse (black) methods. Bottom: Time series of deduced phases.

suppressing the influence of S_{z0}, the MI scheme's performance is independent of the bias field. For the old scheme, as the bias field drifts, the ideal number of data points that the moving average should average together such that high frequency residuals are suppressed changes proportionally. This is not ideal.

We have found that utilizing the MI does not impact the drift of the Xe magnitudes when the detected Xe phases are locked. It also deos not influence the SNR or bias instability of the comagnetometer. Despite such observations, the MI is clearly a superior scheme and will be implemented exclusively in the future.

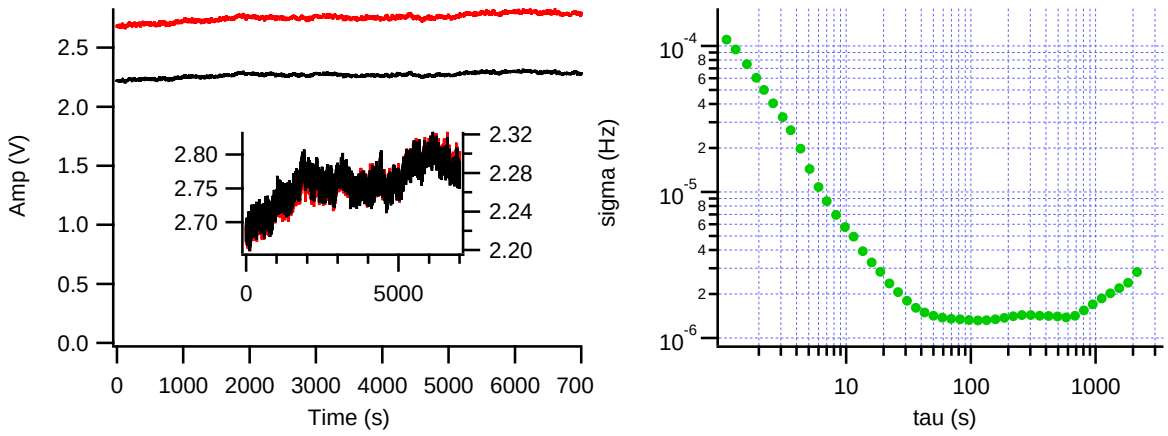

Figure 4.24: New drive scheme preliminary results. Left: measured amplitude of isotope a (black) and b (red) vs. time. The inset shows the same data plotted on individual vertical axes for each isotope. Right: modified Allan deviation of ω^R after scanning B_y and B_x. Fig. 4.18 depicts the bias instability vs B_x and B_y for this data set.

new drive scheme

In addition to implementing the MI fitting algorithm we have also begun exploring drive scheme B (spoken of earlier in the chapter), where $\omega_1 = \omega^b$ and $\omega_2 = \omega^a$. The purpose of the change was to see if the stability of the excited Xe amplitude improved. Figure 4.24 shows the resulting Xe field amplitudes and modified Allan deviation of ω^R for $b_1 = b_2 = 0.4$. Indeed, the drift of the Xe amplitudes (especially isotope a) demonstrate drastic improvement compared to those measured with drive scheme A (see Fig 4.15). We attribute this improvement to the lack of rounding error inherent to drive scheme B (see discussion near Fig 4.15). With the drift due to rounding error resolved, we now see excellent correlation of the magnitudes of the two Xe isotopes (see insert of Fig. 4.24). We attribute these common fluctuations to magnetometer gain drifts which likely stem from pump detuning fluctuations. The modified Allan deviation appears limited by a constant-with-τ noise source at 1 μHz. The ARW is roughly a factor of 2 larger than the ARW demonstrated with drive scheme A as expected due to reduced $K_\perp$ (see Ch. 4.1). Future work will include reprogramming the FPGA so that drive scheme A can be implemented while avoiding error due to rounding.

4.6 Outlook

The detection SNR of isotope a appears to be limited by the DNR of the PDM. The demonstrated ARW is within a factor of 2 of the drive to noise ratio of the pulsing circuit and is similar to the measured detection noise which itself is two orders of magnitude greater than the photon shot noise. The source of limiting noise is uncertain but appears to stem from the bias pulses. One possibility to improve the noise regardless of its source would be to stabilize ϵ_z at high frequency. This could be accomplished by applying an ancillary $B_\perp$ at say 1 kHz and measuring the phase fluctuations (ϵ_z) of the magnetometer's response with a bandwidth of 100 Hz. By making corrections to B_z to keep ϵ_z fixed from DC to 100 Hz the DNR should be improved insofar as the SNR of the measurement of ϵ_z is greater than the pulsing circuits' DNR. Once the ARW is probe (technical) noise limited it may be necessary to implement an auto balancing detection circuit in order to reach the photon shot noise.

Our measurements suggest that the bias instability should reach 200 nHz if: the sum frequency is used to stabilize B_z (thereby enabling an FSF of 1800), the transverse fields are carefully tuned such that $B_{+0} + b_S^K S_+ < 1$ μG and stabilized to have a $1/f$ noise of ~ 1 nG Hz/$\sqrt{\text{Hz}}$, and the pump detuning stability is improved by an order of magnitude. Stabilizing the cell temperature in conjunction with the pump detunings should make the transverse fields which minimize the bias instability the same from day to day. If the bias instability does reach the field suppression limit (200 nHz) then either the field suppression or B_z noise will need to be improved. It is possible that the 10 nG Hz/$\sqrt{\text{Hz}}$ B_z noise we measure is limited by our three layer magnetic shield. If so, upgrading to four layer shield should be pursued. Another possible source of low frequency B_z noise is the pulsing circuit. One could imagine stabilizing the $1/f$ noise from the pulsing circuit by measuring the time average of the voltage sent to the pulsing coil to feedback for correction to the bias field pulse amplitude.

Chapter 5

Future

Discovery is seeing what everyone else has seen, and thinking what nobody else has thought.

— Albert Szent-Gyorgi

Chapters 3 and 4 described the ease with which purely transversely polarized alkali-metal atoms and noble gas nuclei can be produced. The crux of this project is how to detect the noble gas precession via Rb polarization with high SNR and no cross talk. Although the PDM comagnetometer greatly suppressed cross talk while maintaining SNR, the SNR is still orders of magnitude less than the photon shot noise. Furthermore, there exists some source of low frequency drift that limits the bias instability of both devices. The following sections describe options for future inquiry as well as an analysis of how the demonstrated performance could contribute to the precision measurements community.

5.1 Other gas mixtures

We choose to work with vapor cells containing ^{131}Xe and ^{129}Xe because of their similar enhancement factors (which give first order suppression of time averaged S_z) and convenience as our collaborators at NGC share vapor cells with us. There are other advantages to using

these Xe isotopes. Because their masses are similar, their Larmor resonance frequencies are expected to be less dependent on the combined presence of first order magnetic field gradients and temperature gradients [Sheng et al. (2014)]. In addition, their abnormally large enhancement factors contribute directly to the SNR of their detection using the Rb magnetometer. This large signal per unit polarization is advantageous because higher order interactions such as back polarization [Limes et al. (2018)] and through space-J coupling [Limes et al. (2019)] depend on polarization not SE field size.

All of that said, there may be advantages to changing the noble gas pair. The performance of transverse comagnetometry applied to ^{3}He-^{129}Xe cells looks very promising. Compared to ^{131}Xe-^{129}Xe, a ^{3}He-^{129}Xe cell should enable roughly 10 times the T_2 and 10 times the signal [Gentile et al. (2017); Limes et al. (2018)]. If the modest magnetic sensitivity remained the same as our current cell then the anticipated ARW would be 100 nHz/$\sqrt{\text{Hz}}$, an order of magnitude less than what was reported in [Limes et al. (2018)]. Although the improvement in SNR should be dramatic, the sensitivity to longitudinal Rb fields will be much larger ($b_S^a = 110\ b_S^{\text{He}}$[Ma et al. (2011)] versus $b_S^a = 1.002\ b_S^b$[Bulatowicz et al. (2013); Petrov et al. (2019)]), as will the sensitivity to first-order temperature gradients [Sheng et al. (2014)] and back polarization [Limes et al. (2018)].

5.2 Hybrid excitation

Both the PM and PDM comagnetometers have strengths and weaknesses. The strengths of the PM comagnetometer include its insensitivity to $1/f$ transverse magnetic field noise and the fact that it AC couples S_z. The weaknesses of PM are finite SNR due to the dual frequency PM waveform and cross talk due to optical pumping transients and low pass filtering (to prevent $1/f$ detection noise from showing up on the Xe detection channels). One of the strengths of the PDM comagnetometer is its minimal cross talk (likely limited by finite suppression of gain modulation). Its weakness is its sensitivity to $1/f$ transverse

magnetic fields. If one could use both PM and PDM in concert to excite the Xe then all of the weaknesses listed here would be eliminated. In this section we briefly sketched out how such "hybrid" excitation might look. We discuss several possible hybrid drive schemes and calculate the efficiency with which the noble gas isotopes can be excited. We also discuss some finer details salient to Xe phase detection which should mitigate cross talk.

Bloch equation

We find the steady state solution to the Bloch equation describing the Xe nuclei for the case of hybrid excitation where $S_+ = \sum_p s_p e^{ip\omega_1 t} e^{i\epsilon_z}$, and $B_p(t) = B_p 0 + B_1 \cos(\omega_2 t)$. Assuming the transverse fields are well nulled we solve Eq. 2.5a by letting $K_+ = K_\perp e^{\pm i(\alpha+\delta)}$, $\alpha = \int (\omega_d^K + \gamma^K B_1 \cos(\omega_2 t))dt$ and find the real and imaginary parts to be

$$\frac{dK_\perp}{dt} = -\Gamma_2 K_\perp + \Gamma_s s_p J_q (\frac{\gamma^K B_1}{\omega_2}) \cos(\delta \mp \epsilon_z) \rightarrow K_\perp = \frac{\Gamma_s s_p J_q}{\Gamma_2} \tag{5.1}$$

$$\frac{\delta^K}{dt} = -\Delta^K - \frac{\Gamma_s s_p J_q}{K_\perp} \sin(\delta^K \mp \epsilon_z) \tag{5.2}$$

where we have assumed ω_d^K is chosen to satisfy the resonance condition $\omega_d^K + p^K \omega_1 + q^K \omega_2 \sim 0$. There are many possible drive schemes whereby the Xe can be excited. We plot the product $j^K = s_p J_q (\gamma^K B_1/\omega_2)$ for each isotope and several drive schemes (described in Table 5.1) in Fig. 5.1. For this data we assume square wave modulation such that $s_p = 2/(\pi p)$. Note: the argument of the Bessel function can be conveniently rewritten as $\omega^K b_1/\omega_2$ where $b_1 = B_1/B_0$. Drive scheme A minimizes ω_2 but $j^a < 0.12$ for all b_1. Drive scheme B minimizes ω_1 and produces $j^a, j^b > 0.2$ but requires a large b_1. Minimizing ω_1 may be advantageous because doing so reduces the rate of optical pumping transients which can produce cross talk (see next section). Drive scheme C makes $\omega_1 \sim \omega_2$ but produces $j^b < 0.15$ for $b_1 < 1$. Drive scheme D produces the most $j^a + j^b$ for $b_1 < 1$. Although $b_1 > 1$ is possible, it will require the ability to apply opposite polarity bias pulses (e.g. $\pm 2\pi$). These calculations suggest

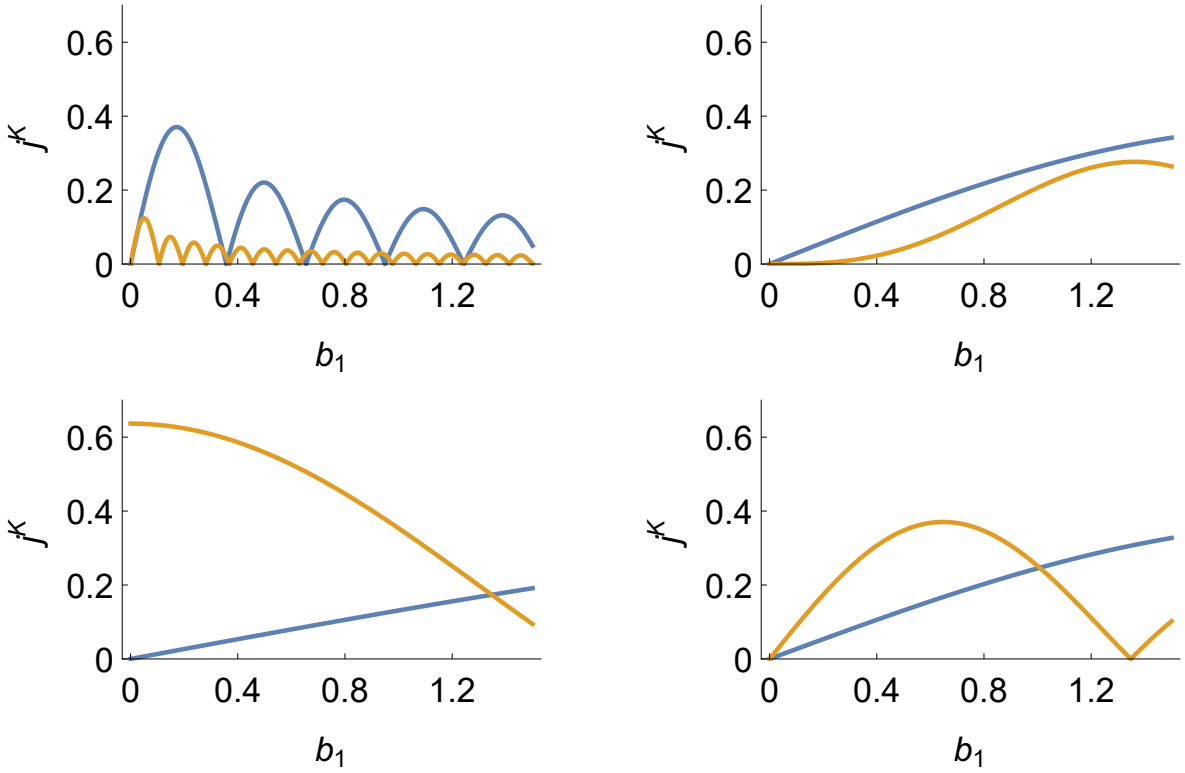

Figure 5.1: Efficiency of excitation for hybrid pumping of isotope a (orange) and isotope b (blue) vs b_1 for various drive schemes. Top: scheme A (left) and scheme B (right). Bottom: scheme C (left) and scheme D (right). See Table 5.2 for drive scheme specifics.

	A	B	C	D
$\omega_d^a =$	$3\omega_1 + \omega_2$	$3\omega_1 + \omega_2$	ω_1	$\omega_1 + \omega_2$
$\omega_d^b =$	$\omega_1 - \omega_2$	$\text{-}\omega_1 + \omega_2$	$\omega_1 - \omega_2$	$\omega_1 - \omega_2$
$\omega_1/2\pi \sim$	11	1	30	20
$\omega_2/2\pi \sim$	1	44	20	10

Table 5.1: Four hybrid excitation schemes. The rows of ω_1 and ω_2 are approximations rounded to the nearest Hz assuming $\omega_0^b/2\pi = 10$ Hz. See Fig 5.1 for corresponding j^a, j^b vs b_1 curves.

that the transverse Xe SE field excited by a hybrid excitation scheme will be similar to that produced by PM and PDM, roughly 10's of μG.

Detection

As Ch.3-4 demonstrate, exciting Xe is much less than half the battle. Here we discuss how to detect the Xe phase of precession while avoiding cross talk for the hybrid comagnetometer. We showed in Ch. 4 that utilizing a detection scheme which takes into account the modulation of the bias field suppresses cross talk between detection channels of the noble gas precession phases. The matrix inverse fitting algorithm (discussed at the end of Ch. 4) can be used for the detection of the hybrid driven Xe signals as well. The fit used to deduce the Xe phases should have the gain reversals due to PM "baked" into it. Possible sources of cross talk include optical pumping transients due to polarization modulation (see Ch. 3), not taking into account asymmetric gain between σ^+ and σ^- pump polarizations, and gain modulation due to PDM (see Ch. 4). Optical pumping transients can be avoided by not sampling S_z during the optical pumping transients. This can be guaranteed by choosing $\omega_3 = n\ \omega_1$, where ω_3 is the bias pulse gating frequency and n is an integer. Gating the bias pulses and detecting S_z when the magnetometer gain has stabilized not only avoids sampling during optical pumping transients but also avoids gain modulation due to PDM. Asymmetric gain between σ^+ and σ^- pump polarizations can be accounted for in the fit function at the cost of roughly doubling the number of fit parameters. Note: the number of S_z samples per fit batch must be larger than the number of free parameters. Additionally, since ω_3 is the effective sampling rate of S_z and acquiring data at anything but a constant rate is inconvenient, one is inclined to fix ω_1 thereby necessitating feedback to B_z and ω_2 to maintain resonance of each isotope (if one fed back to ω_1 then ω_3 would wander around with the bias field!). By following the admonitions found in this paragraph the hybrid comagnetometer should exhibit minimal cross talk.

5.3 Separate vapor cells

In this section I explore the ramifications of separating the two noble gas species into separate vapor cells. Having a single vapor cell with two noble gas species has several advantages. First and foremost is the great prospect for miniaturization to chip-scale. Such a set-up requires only two lasers. The fact that both species sample the same volume also helps alleviate NMR frequency shifts due to bias field inhomogeneities. But these advantages come at a cost. Exciting and detecting both species with the same alkali vapor inevitably reduces the realized T_2 compared to a single species vapor cell and enables cross talk. Additionally, any measure of longitudinal noble gas polarization using the alkali atoms is sensitive to the sum of each isotope's longitudinal polarization. Without knowledge of which isotope is generating K_z one can not make proper corrections to suppress the same. Finally, the co-location of noble gas nuclei enable frequency shifts due to through space J-coupling (see discussion below) directly between the two nuclei.

These disadvantages are all overcome by simply separating the noble gas species into two vapor cells with different alkali species. Doing so would increase the required number of lasers from two to four (a pump and probe laser for each alkali species) as well as double the volume occupied by the noble gases. Comagnetometry would be much more sensitive to the bias field uniformity and the noble gas species would still be sensitive to each other's dipolar field. But there would be marked improvement in each noble gas species T_2 and hence SNR while avoiding the possibility of cross talk all together. The K_z produced by each noble gas species would also be readily obtainable enabling suppression of such. Surprisingly, this separate vapor cell concept has not been explored in the literature.

5.4 Applications

To date, our comagnetometers have only been used to measure noise. In the sections that follow we outline several non-zero spin-dependent interactions that our device could be used to measure.

Scale factor calibration

We have shown that our device can measure rotation rates down to 1 μHz if we assume a scale factor which depends only on the gyro-magnetic ratios and finite gain of the frequency locked loops. We have yet to confirm the scale factor by measuring a standard rotation source. The earth's rotation is such a source. With knowledge of the latitude and orientation of the comagnetometer's sensitive axis one can compute the earth's expected rotation rate to much less than 1 μHz. By mounting our comagnetometer apparatus on a swivel table we can measure the comagnetometer's rotation frequency as a function or sensitive axis orientation relative to the earth's axis of rotation. In order to calibrate the scale factor for rotation rates other than earth's, the device must be installed on a calibrated rate table as was performed with the NGC-gryo [Walker and Larsen (2016)].

Through-space J-coupling

Just as a spin-spin coupling (SSC) enables angular momentum to flow from polarized alkali-metal atoms to noble gas nuclei via spin-exchange collisions, so too there exists a SSC between polarized noble gas nuclei of different species. Although this SSC is readily observed in molecules, SSC in unbound nuclear spin systems (such as vapor cells) are much more difficult to observe due to molecular motion. The first experimental observation of SSC coupling between two different polarized nuclei in a vapor cell was reported just last year [Limes et al. (2019)]. The coupling was manifest in the FID ^{3}He-^{129}Xe comagnetometer by measuring how the cylindrical vapor cell's aspect ratio influenced the comagnetometer's

frequency dependence on longitudinal polarization of ^{3}He. They showed that the dipole field experienced by the Xe can be written as

$$B_z^{Xe} = (1/3 - n_z + 2\kappa_{HeXe}/3)B_z^{He}, \tag{5.3}$$

where n_z is the magnetometric demagnetizing factor, which depends on the cell aspect ratio, and B^{He} is the dipolar magnetic field from the He. The longitudinal polarization of He was varied and not Xe because it was so much larger. The SSC between noble gases contained in a vapor cell depends only on the vapor cell shape because their diffusion rate across the entire cell is much faster than the timescales of transverse relaxation and long-range dipolar interactions. They measured the frequency enhancement factor to be $\kappa_{HeXe} = -0.011$. This was later verified by a second group whose comagnetometer contained polarized He and Xe and relied on a SQUID for precession detection (the Rb was frozen out and removed after SEOP) [Terrano et al. (2019)].

Recent calculations suggests that the enhancement factor between ^{129}Xe and ^{131}Xe, which has yet to be measured experimentally, is $\kappa_{XeXe} = -0.35$ [Vaara and Romalis (2019)]. In order to analyze how large of a frequency shift the SSC between our two Xe isotopes would produce in our vapor cell one need only know n_z and the max longitudinal polarization achievable. Because we assume our cell is symmetric, we believe that $1/3 - n_z \approx 0$. Hence, we can rewrite Eq. 5.3 as $B_z^{a,b} \approx B_z^{b,a}\kappa_{XeXe}2/3$. Since our SE fields measured by the Rb are about 50 μG we expect the dipolar field from the nuclei to be $50\mu\text{G}/500 \approx 0.1\,\mu$G. So if we tipped all of ^{129}Xe's polarization into the $\hat{z}$ direction then we would expect ^{131}Xe's Larmor resonance frequency to shift by $\delta\omega^b = \gamma^b B_z^a \kappa_{XeXe}2/3 \approx 8$ μHz. In practice one would not want to tip all of isotope a into the $\hat{z}$-direction because then isotope a would not precess and the comagnetometer would be compromised. So a more realistic Larmor frequency shift would be more like 1 μHz due to $K_z^a/K_\perp^a = 10\%$.

Although it can be argued that the most unambiguous means of measuring κ_{XeXe} is to

vary the cell shape, the through-space J-coupling between nuclei is the only mechanism which allows for a signed comagnetometer frequency shift whose dependence on K_z^a and K_z^b is the same. Hence, a convincing search for κ_{XeXe} could be pursued by looking for correlations between the comagnetometer frequencies and $K_z^{a,b}$. So how would one produce and measure time averaged K_z of each isotope individually in a controlled fashion? For the case of PM excitation this is simply achieved by applying an AC B_y field which is resonant with the isotope one desires to tip into $\hat{z}$. For the case of PDM this can be achieved by applying $B_x = B_0 \frac{d}{dt} \cos(\alpha^K)$. (Note: the application of a DC B_y to the PDM comagnetometer would produce K_z for both isotopes simultaneously). The amount of K_z produced for either PM or PDM excitation can be monitored using ϵ_z. Because we detect $\delta \mp \epsilon_z$ the production of K_z^i will cause a frequency shift of isotope i (see Eq. 2.3). Such a "self" frequency shift would not be a problem for resolving κ_{XeXe} if we simply looked for correlations between K_z^a and ω^b and vice verse. However, the $1/f$ magnetic noise inside our shield is two orders of magnitude too large to resolve the frequency shifts due to through space J-coupling, thereby requiring we search for the coupling using ρ or ω^R, which will exhibit the self shift as well as the through space J-coupling.

In summary, both our PM and PDM comagnetometers have demonstrated sufficient sensitivity to enable the first measurement of κ_{XeXe}. We have outlined the basic procedure for searching for a through space J-coupling and remarked on several anticipated subtleties regarding the measurement.

Spin-mass coupling

Dual-species synchronous SEOP is an excellent technique for performing a direct search for axion-induced spin-mass couplings. Because of the Yukawa type potentials assumed for spin-mass couplings, miniaturized comagnetometers enable broad energy resolution of the supposed coupling. If the results reported in this study are reproduced in a 2 mm cell, we

anticipate being able to improve the present upper bound in the sub-millimeter wavelength range by an order of magnitude. The previous upper bound was set using a prototype of the NGC-gyro [Bulatowicz et al. (2013)]. The upper bound for scalar-psuedo scalar spin-mass couplings from that work was limited by residual comagnetometer frequency uncertainty of 10 μHz after 20 hours of data acquisitions. The PDM comagnetometer, as shown in Chapter 4, surpasses this uncertainty after merely 10 seconds of integration. Besides switching to a 2 mm inner diameter cubic cell, our apparatus would also need to accommodate a translatable zirconia rod whose diameter is greater than 2 mm. Because this rod must be placed along the $\hat{z}$-direction, in the probe laser's path, the probe will need to be retro-reflected. Because the noble gas nuclei diffuse through the entire cell over a T_2, the closest approach of the rod to the cell center determines the Compton wavelength range that is probed with meaningful sensitivity. Hence, it behooves the experimenter to retro-reflect the probe laser in as compact a fashion as possible. A reasonable solution is to apply a silver coating to the face of the cell the probe laser exits. In this way the probe will be retro-reflected back along the $\hat{z}$-direction from whence it came allowing the zirconia rod to approach as close as possible to the cell wall.

Work on a preliminary prototype with Mike Snow's research group at the University of Indian has already begun. They have developed a compressed air actuator which should translate the zirconia rod in a highly repeatable fashion without producing substantial magnetic fields.

Appendix A

Estimating Γ_S^K, b_K^S, and Γ'

In the two previous sections we derived expressions characterizing the expected time average transverse noble gas polarization $K_\perp$ for PM and PDM excitation. Knowledge of the Rb-Xe SE rate Γ_S^K is required to estimate $K_\perp$. The signal we measure however is the SE field as experienced by the Rb atoms which is proportional to b_K^S, and Γ'. In this section we demonstrate how to estimate the Rb-Xe SE rate, SE field enhancement factor, and Rb relaxation rate given a vapor cells partial pressure composition.

Rb-Xe spin-exchange rate

We define the SE rate to be the SE contribution to T_1 of the Xe nuclei. We will introduce an expression describing the SE rate for ^{129}Xe. The SE rate for ^{131}Xe, which is complicated by its nuclear spin of 3/2, is sufficiently well approximated by dividing Γ_S^a by ρ^2. Assuming that the ^{85}Rb atom spins are in spin-temperature equilibrium we write Walker and Larsen (2016)

$$\Gamma_S^K = \Gamma_{bin}^K + \Gamma_{vdW}^K = k_{bin}[Rb] + k_{vdW}[Rb], \tag{A.1}$$

and

$$k^a_{vdW} = \frac{(\alpha\tau)^2}{2T_X[Rb]}\left(\frac{1+q(\omega\tau)^2/g_I^2}{1+(\omega\tau)^2}\right) \tag{A.2}$$

where k is the SE rate coefficient, Γ_{bin} is the relaxation rate due to binary (Xe-Rb) collisions, Γ_{vdW} is the relaxation rate due to the formation of Rb-Xe van der Waals molecules mediated by N_2 collisions, $[Rb]$ is the Rb density, $1/T_X$ is the molecular formation rate, α characterizes the hyperfine interaction strength (as noted at the beginning of this chapter), τ is the molecular lifetime, $g_I = 2I+1 = 6$ with $I = 5/2$ being the ^{85}Rb nuclear spin, $q = 2+\frac{8}{3+S^2}+\frac{8}{1+3S^2}$ is the slowing down factor for ^{85}Rb (note the dependence on Rb polarization), and $\omega = 2\pi$ 3.0357 GHz is the hyperfine frequency. We can derive an expression for $1/T_X$ by considering that the molecular formation rate must be equal to the rate of molecular breakup such that

$$\frac{[Xe]}{T_X} = \frac{[RbXe]}{\tau} = \frac{k_{chem}[Rb][Xe]}{\tau} \rightarrow \frac{1}{T_x} = \frac{k_{chem}[Rb]}{\tau}, \tag{A.3}$$

where k_{chem} is the chemical equilibrium coefficient. The product $\omega\tau$ was measured at two different temperatures in a He(98%)-N_2(1%)-Xe(1%) vapor cell Nelson and Walker (2001). A linear interpolation of these two data is $(\omega\tau)_{Nelson} = -9.12\frac{\text{amg}}{\text{[He]K}}T + 5340\frac{\text{amg}}{\text{[He]}}$, where T is the cell temperature in Kelvin. As our vapor cells contain Xe and N_2 instead of He we need to take into account the relative molecular breakup rates compared to He. We write $k_{He}[He] = k_{Xe}[Xe] + k_{N2}[N_2]$ so that our expression for $\omega\tau$ becomes

$$\omega\tau = (\omega\tau)_{Nelson}\frac{[He]}{\frac{k_{Xe}}{k_{He}}[Xe] + \frac{k_{N2}}{k_{He}}[N_2]}. \tag{A.4}$$

Table A.1 lists the quantities and their references used to compute k^a_S. Figure A.1 shows k^a_S vs [Xe] and $[N_2]$ for various cell temperatures. We see that k^a_S is maximized when [Xe] is minimized in confirmation of the Saam-Drehus principle, "The secret to achieving high Xe polarization is to not put any Xe in your vapor cell". That said, recall from Eq. 2.3 that the

Term	Value	Ref
α	2π 29 MHz	Bhaskar et al. (1982, 1983)
k_{Xe}/k_{He}	4	Chann et al. (2002)
k_{N2}/k_{He}	1.6	
k_{chem}	213×10^{-24} cm^3 $(T/353)^{-3/2}$	Nelson and Walker (2001)

Table A.1: Values used to compute k_{vdW}.

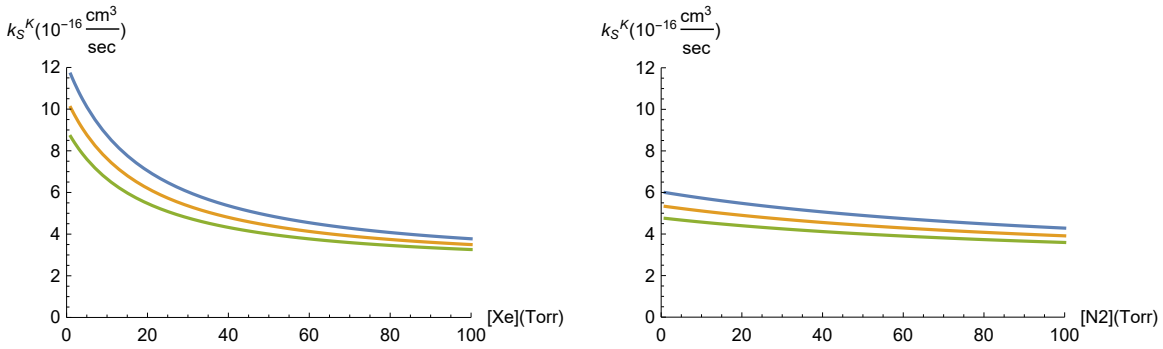

Figure A.1: Influence of cell temperature, [Xe], and [N2] on k_S^a. Left shows k_S^a vs [Xe] for [N2]=50 Torr. Right shows k_S^a vs [N2] for [Xe]=50 Torr. The influence of temperature is displayed using the colors; Blue= 100 C, Orange= 120 C, Green= 140 C. All traces assume Rb polarization of 1/2.

SE field we measure is $b_K^S K_\perp$, where b_K^S depends linearly on [Xe]. In the next section we discuss how to estimate b_K^S.

In conclusion of this section we note that at a Rb density of 10^{13} cm^{-3} (T = 120 C) the ^{129}Xe SE rate is $\Gamma_S^a \approx 6$ mrad/sec while $\Gamma_S^b \approx 0.5$ mrad/sec depending mostly on [Xe]. We can use these numbers to estimate the maximum $K_\perp$ achievable for both isotopes for each excitation scheme. We set the Rb polarization to $S_\perp = 1/2$ and let $s_p = 1$ for PM and $J_p J_q = 1$ for PDM (these are not realistic values but are sufficient to estimate an upper bound). Assuming $\Gamma_2 = 10$ mHz for both isotopes (which is realistic) we find the maximum polarizations to be $K_\perp^a = 0.05$ and $K_\perp^b = 0.004$.

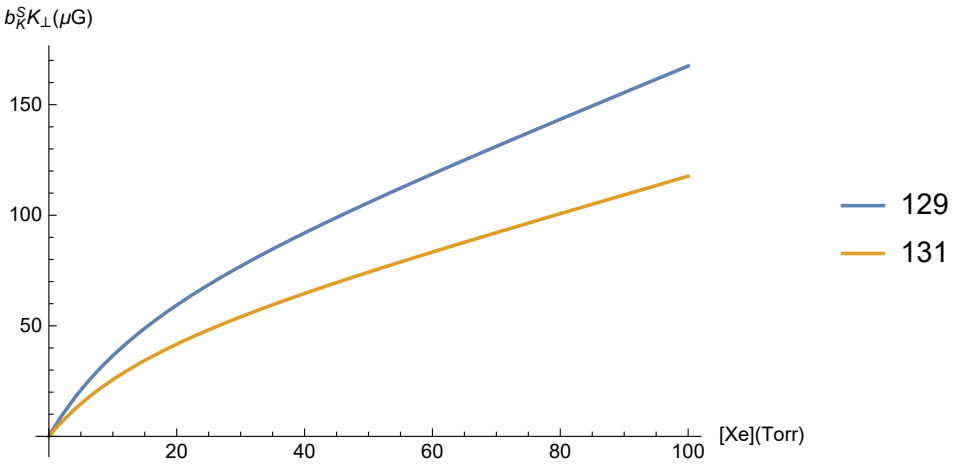

Figure A.2: Dependence of b_a^S and b_b^S on [Xe].

Term	Value	Ref
κ_{XeRb}	518	Nahlawi et al. (2019)
γ^a	1177.7 Hz/G	
γ^b	349.1 Hz/G	
μ_N	762.2591 Hz/G	

Table A.2: Values used to compute b_K^S.

spin-exchange field enhancement factor

From Eq. 2.3 we find $b_K^S = \kappa_{RbXe} g_K \mu_N n_K 8\pi/3$. We need an expression for g_K in terms of the gyromagnetic ratio γ^K. Recall that in a magnetic field the energy of the nuclear spin is $H = -BK_z g_K \mu_N / I = h\gamma B K_z$ where I is the nuclear spin. Hence, $g_K = hI/\mu_N$. We find it convenient to multiply and divide by $\mu_N = \frac{e\hbar}{2Mc}$ where M is the mass of the proton and c is the speed of light so that our expression for b_K^S becomes

$$b_K^S = \frac{8\pi}{3} \frac{\gamma^K}{\mu_N} \frac{I}{2\pi\mu_N} \left(\frac{e\hbar}{2Mc}\right)^2 \kappa_{RbXe} n_K \tag{A.5}$$

In the previous section we found that the expected maximum $k_\perp$ achievable by either excitation scheme for ^{129}Xe was ρ^2 larger than for ^{131}Xe. In order to make the SE fields produced by these very different polarizations similar we enrich the Xe content of our cells

to be 1 part ^{129}Xe to 9 parts ^{131}Xe. Figure A.2 shows the SE field produced as a function of enriched Xe partial pressure according to the equation,

$$B_K^s = b_K^S([Xe])\frac{\Gamma_S^K([Xe])}{\Gamma_1}S_\perp, \tag{A.6}$$

where we assume $S_\perp = 1/2$, [Rb]= 10^{13}cm^{-3} (T = 120 C), and [N2] = 50 Torr. Table A.2 lists specific values we use to compute b_K^S. We see that SE fields on the order of 100 μG are achievable for both isotopes.

Rb relaxation rate

The Rb relaxation rate $\Gamma' = R + \Gamma_K^S$ is determined by the optical pumping rate R and relaxation due to Xe atoms Γ_K^S (relaxation due to the cell wall is negligible). The magnetometer detects

$$S_z = \frac{R\Omega_y^K}{\Gamma'^2 + \Omega^2} \tag{A.7}$$

which optimizes for $R = \Gamma_K^S$. Hence, if we know Γ_K^S we can pick parameters which control R (D1 laser polarization, detuning, and power) to satisfy this relation. This discussion assumes zero field spin-exchange relaxation free (SERF) magnetometry. The influence of our pulsed bias field has been calculated to be $\Gamma'_{pulsed} \approx 3\Gamma'_{SERF}$ Korver (2015). For the purpose of this discussion we find it sufficient to ignore the pulsed bias field.

Similar to Γ_S^K, $\Gamma_K^S = \Gamma_{bin}^S + \Gamma_{vdW}^S$ can be written in terms of binary and vdW terms. The binary contribution depends only on the number of Xe atoms (partial pressure) and was measured to be $\Gamma_{bin}^S/[\text{Xe}] = 321$ sec^{-1} Torr^{-1} Nelson and Walker (2001). The vdW contribution depends on the concentration of all atoms in the cell and the cell temperature. The vdW's contribution was measured at two temperatures in the same mostly He cell mentioned previously. To calculate Γ_{vdW}^S in our cell we need to derive an expression to scale

these measured values, taking into account both temperature and partial pressures. We write

$$\Gamma^S_{vdW} = \frac{2\phi_\gamma^2}{3T_A}, \tag{A.8}$$

where ϕ_γ is the rms precession angle form the spin rotation interaction and the alkali-noble-gas SE interaction, and T_A is the molecular formation rate per Rb atom. In order to find an expression in terms of the cell's constituent partial pressures, we expand $\phi_\gamma = \gamma N \tau$, which comes from the Hamiltonian $H = \gamma \mathbf{S} \cdot \mathbf{N}$, where $\mathbf{N}$ is the angular momentum of the vdW molecule, and $1/\tau$ is the break up rate. Similar to Eq. A we write,

$$\frac{[Rb]}{T_A} = \frac{[RbXe]}{\tau} = \frac{k_{chem}[Rb][Xe]}{\tau} \rightarrow T_A = \frac{\tau}{k_{chem}[Xe]}. \tag{A.9}$$

We can expand $1/\tau$ in terms of each atom's break up rate

$$\frac{1}{\tau} = \frac{1}{\tau_{Xe}} + \frac{1}{\tau_{N2}} + \frac{1}{\tau_{He}} = k_{Xe}[Xe] + k_{N2}[N2] + k_{He}[He], \tag{A.10}$$

where k is the cross section times the velocity. Replacing ϕ_γ, and T_A in Eq. A yields,

$$\Gamma^S_{vdW} = \frac{2(\gamma N)^2 k_{chem}}{3k_{Xe}(1 + \frac{k_{N2}[N2]}{k_{Xe}[Xe]} + \frac{k_{He}[He]}{k_{Xe}[Xe]})}. \tag{A.11}$$

Note how Eq. A is independent of total pressure but depends on the relative pressures. Fitting the two measurements of Γ^S_{vdW} from Ref. Nelson and Walker (2001) to AT^a, where T is the temperature in K yields $A = 7.59 \times 10^9$ sec^{-1} and $a = -2.5$. Finally we write an expression Γ^K_{vdW} for our cell estimated from measurements made on Nelson et al.'s cell as follows

$$\Gamma^K_{vdW} = 7.59 \times 10^9 \text{ sec}^{-1} T^{-2.5} \left(\frac{1 + \frac{k_{N2}}{k_{Xe}}\frac{[N2']}{[Xe']} + \frac{k_{He}}{k_{Xe}}\frac{[He']}{[Xe']}}{1 + \frac{k_{N2}}{k_{Xe}}\frac{[N2]}{[Xe]} + \frac{k_{He}}{k_{Xe}}\frac{[He]}{[Xe]}} \right), \tag{A.12}$$

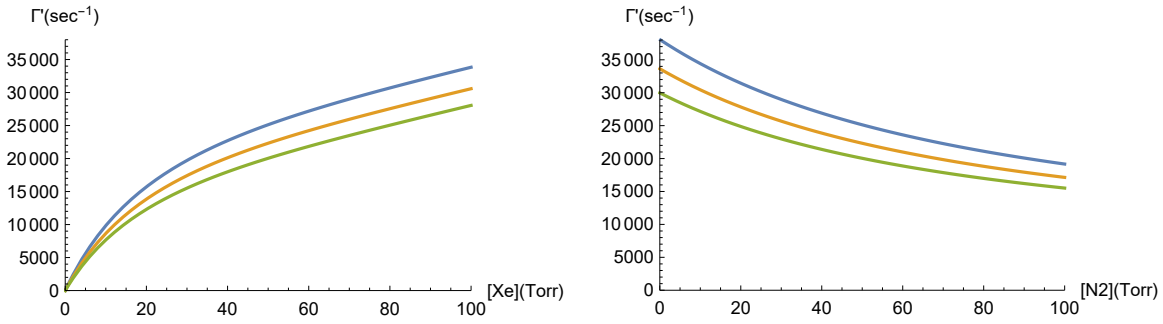

Figure A.3: Influence of Temperature, [Xe], and [N2] on Γ'. Left shows Γ' vs [Xe] for [N2]= 50 Torr. Right shows Γ' vs [N2] for [Xe] = 50 Torr. The influence of temperature is displayed using the colors; Blue= 100 C, Orange= 120 C, Green= 140 C. All traces assume Rb polarization of 1/2.

where [Xe'] = 1%, [N2'] = 1%, and [He']=98%. Figure A.3 Shows our estimate of Γ' vs [Xe] and [N2] assuming $R = \Gamma_K^S$ and $S_\perp = 1/2$. Similar to Γ_S^K, Γ' is dominated by [Xe]. Not only does Γ' determine the Rb magnetometer's scaling from field to Volts, but it also scales the sensitivity of ϵ_z to B_z. We will also see in the sections that follow how Γ' limits the sensitivity of the comagnetometer through photon shot noise.

We find that in practice the estimations presented in this section are only good for order-of-magnitude approximations. The discrepancy is not surprising as the cell compositions we use are not similar to the cell compositions used in the few measurements which exist in published literature. Besides improperly accounted for differences in partial pressure, optical thickness effects in our system, which are difficult to parameterize, also make these estimates unreliable. We find that, in general, the Xe concentration of the vapor cell and number of pump photons should be increased until the photon shot noise limits the performance of the comagnetometer.

Appendix B

LabVIEW FPGA

As mentioned in the main body of the thesis, the FPGA allows us to compare the phase of precession of the noble gas nuclei to the phase of a commercial atomic clock. In the sections that follow we discuss DDS in general as well as how it is implemented in LabVIEW FPGA software.

Direct digital synthesis

DDS is a digital programming technique used to synthesize arbitrary frequencies from fixed system clocks. A direct digital synthesizer consists of two components: a phase register, and a look-up table (LUT). A phase register is simply an unsigned integer counter that wraps. The LUT determines the DDS output for a given phase register input. The phase register and LUT are placed in a loop which executes at fixed rate f_{up}. Each iteration of the loop adds Δn to the phase register such that the phase register output repeats at frequency f according to

$$f = \Delta n f_{up}/2^b, \tag{B.1}$$

where b is the bit width of the phase register counter. The influence of the phase register resolution on the frequency uncertainty of the DDS is found by replacing $\Delta n = 1$ and $f = \delta f$ such that $\delta f = f_{up}/2^b$. For an update rate of 10 MHz and 64 bit counter the frequency uncertainty is better than 1 pHz.

Advanced techniques

The code outlined in the sections that follow utilizes several advanced programming techniques such as multiplexing, first-in-first-out (FIFO) memory, polling, and single cycle timed loops. An excellent resource describing these concepts and others in terms of LabVIEW FPGA code can be found in [Instruments (2014)].

The LabVIEW FPGA software consists of two parts: code that runs on the FPGA, and code that runs on the Host computer. The Host computer we use is embedded in the Labview Chassis in which our FPGA is installed. This Host computer has a Labview operating system called Real Time. We actually write the programs (for both FPGA and Host) on a seperate desktop computer. In order to run the programs we write, we must command the Host computer to compile the FPGA code onto the FPGA device. The amount of time this compilation takes depends on the complexity of the FPGA code one is trying to compile.

It is important to understand the difference between the Host and FPGA. The timing of the Host is not rigid, but it has much greater resources enabling it to perform double precision arithmetic. The FPGA has very rigid timing (if a loop can not run on time there will likely be an error), but it has finite resources (mostly limited to integer arithmetic). In general, the FPGA code contains the DDS, DAQ (the hardware for which is built into the FPGA), and demodulation code. The Host contains the data archiving, digital filtering, and double precision arithmetic. As much computation as possible should be performed on the Host instead of the FPGA because of the FPGA's finite resources. The general naming scheme for the hundreds of files we have written follows the scheme "XY_Host.vi"

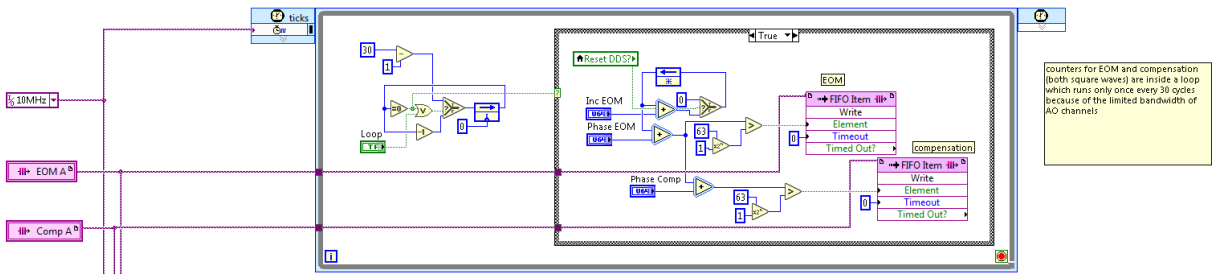

Figure B.1: Code for LabVIEW FPGA DDS generator.

and "X_FPGA.vi". Since it is common to use the same FPGA code for different Host progam files, the Y is used as a Host program version identifier.

The following snippets of code are from the FPGA program named "kappaE" which is used to control the PDM comagnetometer. We will describe the function of the code and provide motivation for its particular form. We begin by describing the code used to generate two analog square waves of the same arbitrary frequency but with independent phase and amplitude control. Figure B.1 shows the code for a single DDS generator and square wave LUT. The timed loop in which the code is placed is a so called "single cycle timmed loop" (SCTL) set to execute at 10 MHz. We use a SCTL because it is the most rigid timing stucture in LabVIEW FPGA. If the loop can not execute at the specified rate for any reason then the program will not run and an error will be generated. The programmed rate of SCTLs is limited to certain integers of the master clock of the FPGA, which for our FPGA is 40 MHz. In order to satisfy the finite update rate of the analog output channels,

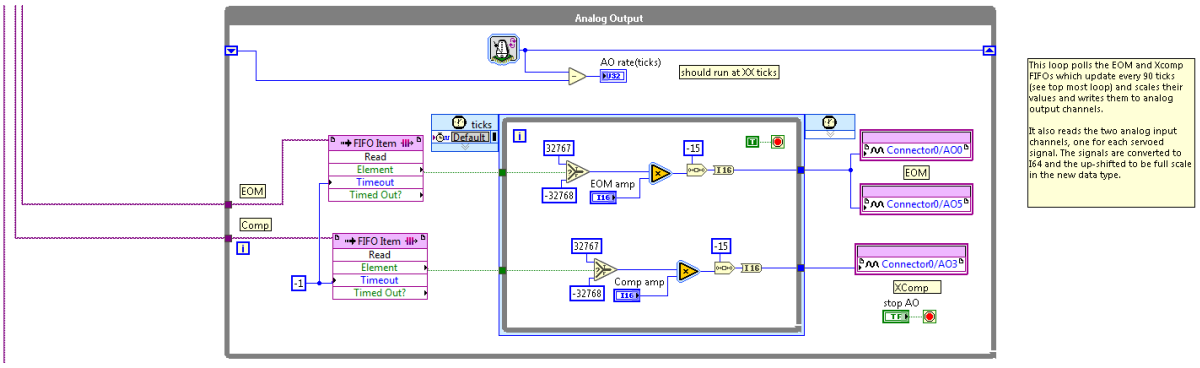

Figure B.2: Code for sending output of LUT to analog output channel.

the DDS code is embedded in a case structure such that despite the SCTL update rate of 10 MHz, the DDS code only runs once every 30 loop iterations or 333 kHz. The DDS generator consists of three input controls, where $IncEOM = \Delta n$ from Eq. B.1 and $PhaseEOM$ and $PhaseComp$ determine the phase of the two channels and are computed on the Host according to $2^{64}\theta/360$ where θ is the phase in degrees. These inputs are used to compute the output of a 64 bit unsigned summer programmed to wrap. The output of the phase register (summer) is compared to 2^{63} or half the bit width. If the output of the summer is less than this value a boolean line is low and if it is greater than this value the boolean line is high. Such constitutes the square wave LUT. The boolean outputs for each channel are then loaded into independent first-in-first-out (FIFO) memory channels.

Figure B.2 shows the code for scaling the output of the LUT and sending it to separate analog output channels. This code can not be place in its entirety inside a SCTL because of the analog output write commands. The loop in which the code is contained is an ordinary

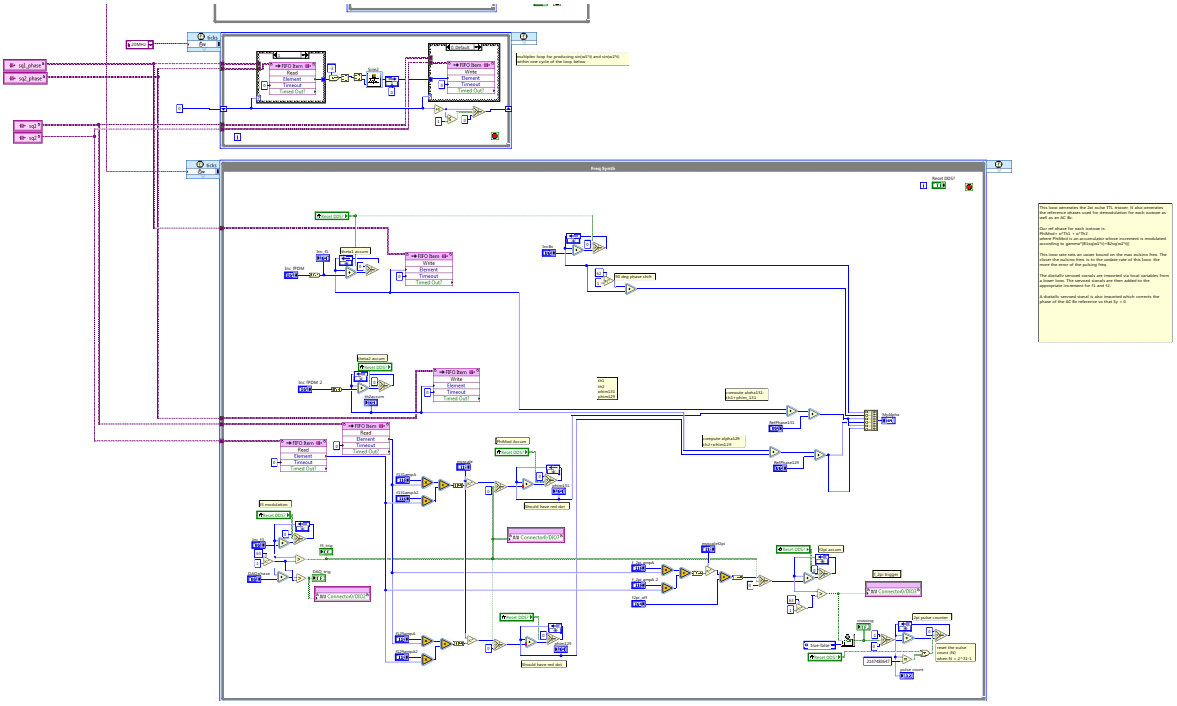

Figure B.3: Code for Computing α for each noble gas.

while loop. The rate of execution of the while loop is controlled by the FIFO read commands such that the loop is "polling" the SCTL mentioned previously (note the -1 in the FIFO timeout read commands). This means that the while loop will execute when both FIFOs have new data to be processed. Polling is a powerful tool for transfering the reliable timing of SCTLs to ordinary while loops. The boolean data is read from each FIFO memory bank. The boolean value is converted to an arbitrary signed 16 bit number (the bit width of the analog output channels) using the code shown in the embedded SCTL. This SCTL is not necessary for the code to run. That said, any code in a SCTL will utilize the minimum number of FPGA resources required to compile the programmed code. Hence, it is wise to put as much code as possible in SCTLs, even when embedded in a while loop. Finally, the signed 16 bit integers are sent to analog output channels.

Figure B.3 depicts the code for generating the 2π pulse triggers and computing α for each noble gas in terms of two phase registers/accumulators labeled θ_1 and θ_2. Because we

need to compute $\sin(\theta_1)$ and $\sin(\theta_2)$ we mutliplex a built-in LabVIEW FPGA vi called LUT. Mutliplexing allows us to utilize a single LUT to compute the sine of each θ. Hence, in the larger SCTL, which executes at 10 MHz, we compute θ_1 and θ_2 and then transfer both values via FIFO memory to the smaller SCTL which computes the sine of θ_1 and θ_2 at a rate of 20 MHz. The output of the faster SCTL is then transferred by FIFO memory (again) back into the larger SCTL for further processing. Because the LUT vi does not support 64 bit inputs we must divide the 64 bit values of the θs into smaller bit widths. Some of the disgarded bits are used for linear interpolation within the LUT. Because the LUT vi takes two cycles to produce a valid output, a feedback node (box with an arrow) is placed directly after the LUT vi. This feedback node delays the output by one cycle. So on the first iteration of the SCTL, the current value of θ_1 is loaded and the LUT produces no output. On the second iteration it loads θ_2 and outputs $\sin(\theta_1)$. On the third iteration it loads θ_1's new value and outputs $\sin(\theta_2)$ etc.

Once the values of $\sin(\theta_1)$ and $\sin(\theta_2)$ are loaded into the larger SCTL they are manipulated to modulate ω_p and compute ϕ_{mod} for each species where

$$\phi_{mod}^K = g(t)\gamma^K \int \left(B_1 \sin(\theta_1(t)) + B_2 \sin(\theta_2(t))\right) dt, \tag{B.2}$$

and g(t) is the gating due to ω_3 modulation. The integral is performed using another phase register for each isotope. The value of α^K is then computed according to

$$\alpha^K = p^K\theta_1 + q^K\theta_2 + \phi_{mod}^K. \tag{B.3}$$

Note: for the code shown: $(p^a, q^a) = (0, 1)$ and $(p^b, q^b) = (1, 0)$. The values of α^a and α^b are then put into an array which is accessed by subsequent while loops (discussed below). The bottom left of the main SCTL depicts the phase register for generating the ω_3 modulation used to gate the 2π pulses. Note how the trigger for ω_3 toggles the input to the ϕ_{mod}

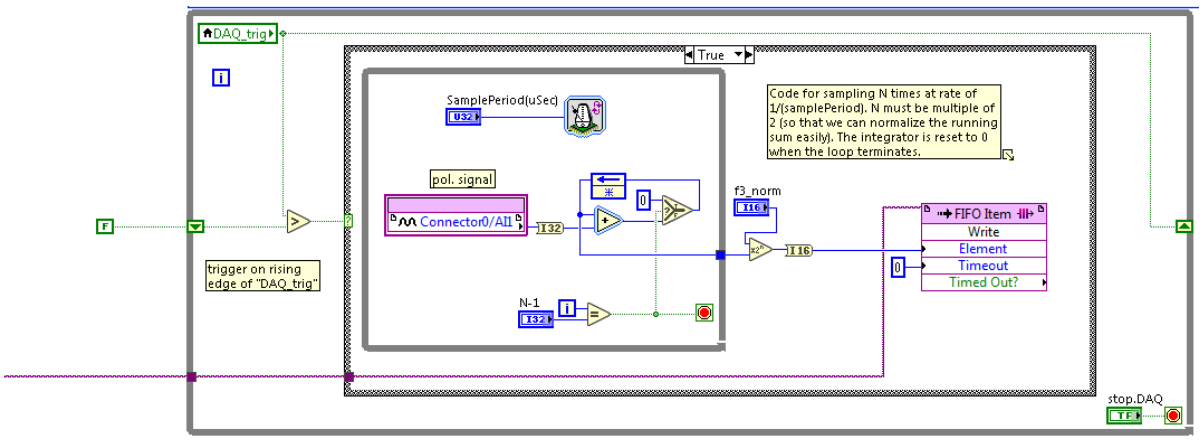

Figure B.4: Code for DAQ trigger and data averaging.

accumulators such that when the pulses are triggered off the value of ϕ_{mod} stays constant. Finally, the bottom right of the main loop depicts the code for the ω_p phase register. This code is similar to ϕ_{mod} for each isotope except there is a constant offset to its input that produces the average pulsing frequency.

The next loop, shown in Fig. B.4 is another standard while loop that performs the triggered acquistion and averaging of the magnetometer signal. The loop cycles as fast as possible (no timing is enforced) effectively polling the variable DAQ_{trig}, which is the trigger for ω_3 generated in the large SCTL discussed previously. When this variable becomes true, a nested while loop executes N times with a rate of $SamplePeriod(usec)$. The analog input Channel 1 is read and summed with previous readings at each iteration of the nested loop. After N iterations (readings) the sum is scaled by $2^{f3_{norm}}$ and then stored in a FIFO memory. The summer is also reset to 0 in preparation for the next signal acquisition.

Figure B.5 shows the code for computing $\sin(\alpha^K)$ and $\cos(\alpha^K)$ among other waves. It

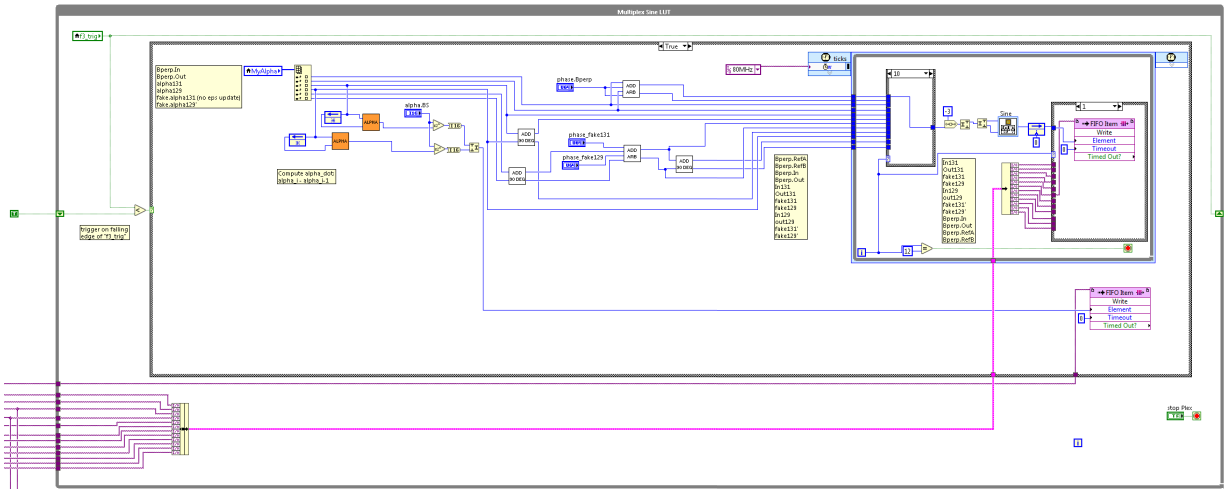

Figure B.5: Code for computing of $\sin(\alpha^K)$ and $\cos(\alpha^K)$

also utilizes multiplexing to compute many sine waves from a single LUT. The loop is triggered similarly to the DAQ loop just discussed. A standard while loop executes as fast as possible. When $f3_{trig}$, which is a phase shifted version of DAQ_{trig}, is true then the code shown in the case structure executes. The code within the case structure is very similar to the mutliplexing code discussed previously but extended to many more channels. Also computed is the change in α^K between successive data acquisitions, which was used in one of the demodulation schemes. Once again, an imbedded SCTL is used not because it is necessary but because it is good practice. The values of $\sin(\alpha^K)$ and $\cos(\alpha^K)$ are stored in FIFO memory for further processing.

Figure B.6 depicts the final while loop of the FPGA program. This standard while loop polls the many FIFO outputs from the many channel mutliplexing loop. Some of these channels are then put into an array and streamed to the Host through a direct memory access FIFO structure, shown in an embedded For loop. This For loop will execute as many

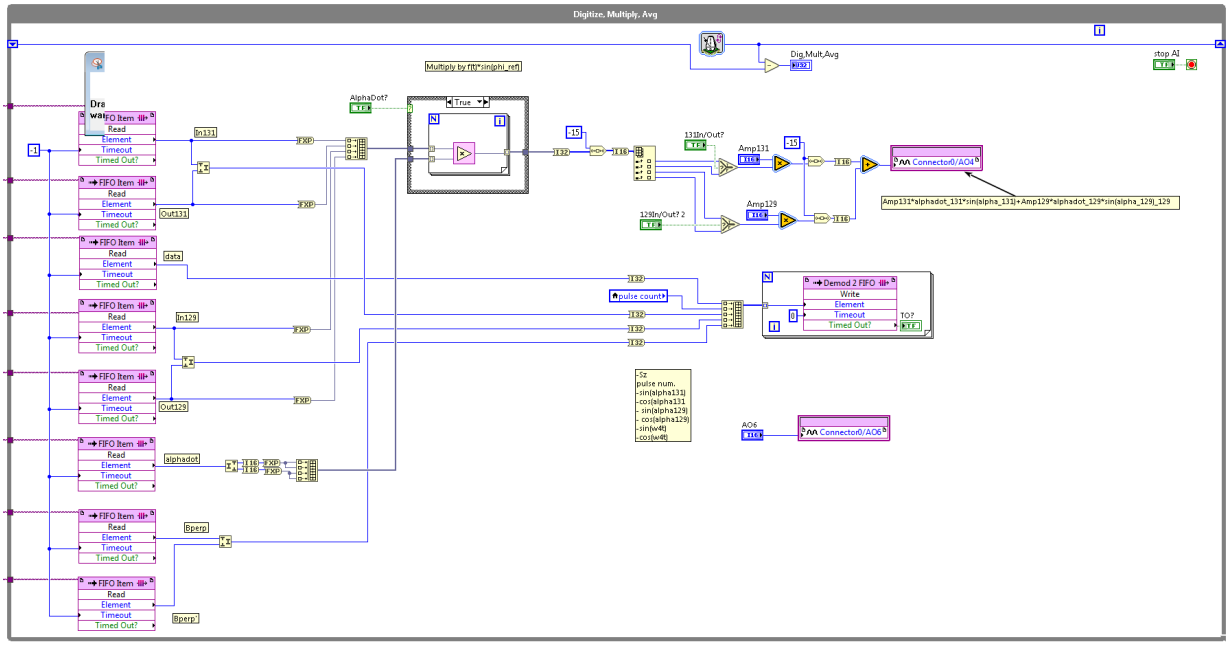

Figure B.6: Code depicting DMA data stream from FPGA to Host

times as there are channels to be written (as long as its input terminal labeled N is unwired).

references

Allan, D.W., and J.A. Barnes. 1981. A modified "allan variance" with increased oscillator characterization ability. *Proceedings of the 35th Anual Frequency Control Symposium, Philadelphia, 1981* 470–475.

Allmendinger, F., I. Engin, W. Heil, S. Karpuk, H.-J. Krause, B. Niederländer, A. Offenhäusser, M. Repetto, U. Schmidt, and S. Zimmer. 2019. Measurement of the permanent electric dipole moment of the ^{129}Xe atom. *Phys. Rev. A* 100:022505.

Bear, D., R. E. Stoner, R. L. Walsworth, V. A. Kostelecky, and C. D. Lane. 2000. Limit on lorentz and cpt violation of the neutron using a two-species noble-gas maser 85:5038.

Bechhoefer, J. 2005. Feedback for physicists: A tutorial essay on control. *Rev. Mod. Phys.* 77:783–836.

Bhaskar, N., W. Happer, M. Larsson, and X. Zeng. 1983. Slowing down of rubidium-induced nuclear spin relaxation of ^{1}29Xe gas in a magnetic field 50:105.

Bhaskar, N., W. Happer, and T. McClelland. 1982. Efficiency of spin exchange between rubidium spins and ^{129}Xe nuclei in a gas 49:25.

Brinkmann, D., E. Brun, and H. H. Staub. 1962. Kernresonanz im gasformigen xenon. *Helv. Phys. Acta* 35:431.

Brown, J. M., S. J. Smullin, T. W. Kornack, and M. V. Romalis. 2010. New limit on lorentz- and CPT-violating neutron spin interactions. *Phys. Rev. Lett.* 105:151604.

Bulatowicz, M., R. Griffith, M. Larsen, J. Mirijanian, C. B. Fu, E. Smith, W. M. Snow, H. Yan, and T. G. Walker. 2013. Laboratory search for a long-range T-odd, P-odd interaction from axionlike particles using dual-species nuclear magnetic resonance with polarized ^{129}Xe and ^{131}Xe gas. *Phys. Rev. Lett.* 111:102001.

Chann, B., I. A. Nelson, L. W. Anderson, B. Driehuys, and T. G. Walker. 2002. $^{129}xe - $Xe molecular spin relaxation. *Phys. Rev. Lett.* 88:113201.

Cheiney, Pierrick, Lauriane Fouché, Simon Templier, Fabien Napolitano, Baptiste Battelier, Philippe Bouyer, and Brynle Barrett. 2018. Navigation-compatible hybrid quantum accelerometer using a kalman filter. *Phys. Rev. Applied* 10:034030.

Chupp, T. E., E. R. Oteiza, J. M. Richardson, and T. R. White. 1988. Precision frequency measurements with polarized ^{3}He, ^{21}Ne, and ^{129}Xe atoms. *Phys. Rev. A* 38:3998–4003.

Donley, E. A., and J. Kitching. 2013. Nuclear magnetic resonance gyroscopes. In *Optical magnetometry*, chap. 19, 369–386. Cambridge University Press.

Flambaum, V. V., and M. V. Romalis. 2017. Limits on lorentz invariance violation from coulomb interactions in nuclei and atoms. *Phys. Rev. Lett.* 118:142501.

Gemmel, C., W. Heil, S. Karpuk, K. Lenz, Yu. Sobolev, K. Tullney, M. Burghoff, W. Kilian, S. Knappe-Grüneberg, W. Müller, A. Schnabel, F. Seifert, L. Trahms, and U. Schmidt. 2010. Limit on lorentz and *cpt* violation of the bound neutron using a free precession ^{3}He/^{129}Xe comagnetometer. *Phys. Rev. D* 82:111901.

Gentile, T. R., P. J. Nacher, B. Saam, and T. G. Walker. 2017. Optically polarized ^{3}He. *Rev. Mod. Phys.* 89:045004.

Grover, BC. 1978. NOBLE-GAS NMR DETECTION THROUGH NOBLE-GAS-RUBIDIUM HYPERFINE CONTACT INTERACTION. *PHYSICAL REVIEW LETTERS* 40(6):391–392.

Hobbs, Philip C. D. 1997. Ultrasensitive laser measurements without tears. *Appl. Opt.* 36(4):903–920.

Instruments, National. 2014. Ni labview high-performance fpga developer's guide.

Jiang, Liwei, Wei Quan, Rujie Li, Wenfeng Fan, Feng Liu, Jie Qin, Shuangai Wan, and Jiancheng Fang. 2018. A parametrically modulated dual-axis atomic spin gyroscope. *Applied Physics Letters* 112(5):054103. https://doi.org/10.1063/1.5018015.

Karwacki, F. A. 1980. Nuclear magnetic resonance gyro development. *Navigation* 27:72.

Katz, O., R. Shaham, and O. Firstenberg. 2019. Quantum interface for noble-gas spins. 1905.12532.

Kornack, T. W. 2005. A test of cpt and lorentz symmetry using a k-^{3}he co-magnetometer. Ph.D. thesis, Princeton University.

Kornack, T. W., R. K. Ghosh, and M. V. Romalis. 2005. Nuclear spin gyroscope based on an atomic comagnetometer. *Physical review letters* 95(23):230801.

Kornack, T. W., and M. V. Romalis. 2002. Dynamics of two overlapping spin ensembles interacting by spin exchange. *Phys. Rev. Lett.* 89:253002.

Korver, A. 2015. Towards an nmr oscillator. Ph.D. thesis, University of Wisconsin-Madison.

Korver, A., D. Thrasher, M. Bulatowicz, and T. G. Walker. 2015. Synchronous spin-exchange optical pumping. *Phys. Rev. Lett.* 115:253001.

Kwon, T. M., J. G. Mark, and C. H. Volk. 1981. Quadrupole nuclear spin relaxation of ^{131}Xe in the presence of rubidium vapor. *Phys. Rev. A* 24:1894–1903.

Lee, J., A. Almasi, and M. V. Romalis. 2018. Improved limits on spin-mass interactions. *Phys. Rev. Lett.* 120:161801.

Li, Zhimin, Ronald T Wakai, and T.G. Walker. 2006. Parametric modulation of an atomic magnetometer. *Appl. Phys. Lett.* 89:134105.

Limes, M. E., N. Dural, M. V. Romalis, E. L. Foley, T. W. Kornack, A. Nelson, L. R. Grisham, and J. Vaara. 2019. Dipolar and scalar ^{3}He$-^{129}$Xe frequency shifts in stemless cells. *Phys. Rev. A* 100:010501(R).

Limes, M. E., D. Sheng, and M. V. Romalis. 2018. ^{3}He$-^{129}$Xe comagnetometery using ^{87}Rb detection and decoupling. *Phys. Rev. Lett.* 120:033401.

Ludlow, Andrew D., Martin M. Boyd, Jun Ye, E. Peik, and P. O. Schmidt. 2015. Optical atomic clocks. *Rev. Mod. Phys.* 87:637–701.

Ma, Z. L., E. G. Sorte, and B. Saam. 2011. Collisional ^{3}He and ^{129}Xe frequency shifts in rb˘noble-gas mixtures. *Phys. Rev. Lett.* 106:193005.

Makulski, W. 2015. ^{129}Xe and ^{131}Xe nuclear magnetic dipole moments from gas phase nmr spectra. *Magnetic Resonance in Chemistry* 53(4):273–279. `https://onlinelibrary.wiley.com/doi/pdf/10.1002/mrc.4191`.

Nahlawi, A. I., Z. L. Ma, M. S. Conradi, and B. Saam. 2019. High-precision determination of the frequency-shift enhancement factor in Rb $-^{129}$ Xe. *Phys. Rev. A* 100:053415.

Nelson, I. A., and T. G. Walker. 2001. Rb-xe spin relaxation in dilute xe mixtures. *Phys. Rev. A* 65(1):012712.

Petrov, V. I., A. S. Pazgalev, and A. K. Vershovskii. 2019. Isotope shift of nuclear magnetic resonances in 129Xe and 131Xe caused by spin-exchange pumping by alkali metal atoms. *IEEE Sensors Journal* 1–1.

Romalis, M.V. 2013. Quantum noise in atomic magnetometers. In *Optical magnetometry*, chap. 2, 25–39. Cambridge University Press.

Rosenberry, M. A., and T. E. Chupp. 2001. Atomic electric dipole moment measurement using spin exchange pumped masers of ^{129}Xe and ^{3}He. *Phys. Rev. Lett.* 86:22–25.

Sachdeva, N., I. Fan, E. Babcock, M. Burghoff, T. E. Chupp, S. Degenkolb, P. Fierlinger, S. Haude, E. Kraegeloh, W. Kilian, S. Knappe-Grüneberg, F. Kuchler, T. Liu, M. Marino, J. Meinel, K. Rolfs, Z. Salhi, A. Schnabel, J. T. Singh, S. Stuiber, W. A. Terrano, L. Trahms, and J. Voigt. 2019. New limit on the permanent electric dipole moment of ^{129}Xe using ^{3}He comagnetometry and squid detection. *Phys. Rev. Lett.* 123:143003.

Schaefer, S. R., G. D. Cates, Ting-Ray Chien, D. Gonatas, W. Happer, and T. G. Walker. 1989. Frequency shifts of the magnetic-resonance spectrum of mixtures of nuclear spin-polarized noble gases and vapors of spin-polarized alkali-metal atoms. *Phys. Rev. A* 39(11): 5613–5623.

Seltzer, S.J. 2008. Developements in alkali-metal atomic magnetometry. Ph.D. thesis, Princeton University.

Sheng, D., A. Kabcenell, and M. V. Romalis. 2014. New classes of systematic effects in gas spin comagnetometers. *Phys. Rev. Lett.* 113:163002.

Takahashi, Y., K. Honda, N. Tanaka, K. Toyoda, K. Ishikawa, and T. Yabuzaki. 1999. Quantum nondemolition measurement of spin via the paramagnetic faraday rotation. *Phys. Rev. A* 60:4974–4979.

Terrano, W. A., J. Meinel, N. Sachdeva, T. E. Chupp, S. Degenkolb, P. Fierlinger, F. Kuchler, and J. T. Singh. 2019. Frequency shifts in noble-gas comagnetometers. *Phys. Rev. A* 100: 012502.

Thrasher, D. A., S. S. Sorensen, J. Weber, M. Bulatowicz, A. Korver, M. Larsen, and T. G. Walker. 2019. Continuous comagnetometry using transversely polarized xe isotopes. *Phys. Rev. A* 100:061403(R).

Vaara, J., and M. V. Romalis. 2019. Calculation of scalar nuclear spin-spin coupling in a noble-gas mixture. *Phys. Rev. A* 99:060501(R).

Vanier, J., and C. Audoin. 1989. In *The Quantum Physics of Atomic Frequency Standards*, vol. 1, chap. Appendix 2F, 216–256. IOP Publishing Ltd, Bristol.

Vasilakis, G., J. M. Brown, T. W. Kornack, and M. V. Romalis. 2009. Limits on new long range nuclear spin-dependent forces set with a $k - he3$ comagnetometer. *Phys. Rev. Lett.* 103(26):261801.

Walker, T.G., and W. Happer. 1997. Spin-exchange optical pumping of noble-gas nuclei. *Rev. Mod. Phys.* 69(2):629–642.

Walker, T.G., and M.S. Larsen. 2016. Spin-exchange-pumped nmr gyros 65:373 – 401.

Wu, Z., S. Schaefer, G. D. Cates, and W. Happer. 1988. Coherent interactions of the polarized nuclear spins of gaseous atoms with the container walls. *Phys. Rev. A* 37: 1161–1175.

Wyllie, R. 2012. The developement of a multichannel atomic magnetometer array for fetal magnetocardiography. Ph.D. thesis, University of Wisconsin-Madison.